TAMPEREEN TEKNILLINEN YLIOPISTO
TAMPERE UNIVERSITY OF TECHNOLOGY

Kalle Koskinen

Novel Aspects of Second-harmonic Generation from Thin Films and Surfaces

Julkaisu 1579 • Publication 1579

Tampere 2018

Tampereen teknillinen yliopisto. Julkaisu 1579
Tampere University of Technology. Publication 1579

Kalle Koskinen

Novel Aspects of Second-harmonic Generation from Thin Films and Surfaces

Thesis for the degree of Doctor of Science in Technology to be presented with due permission for public examination and criticism in Tietotalo Building, Auditorium TB109, at Tampere University of Technology, on the 12th of October 2018, at 12 noon.

Tampereen teknillinen yliopisto - Tampere University of Technology
Tampere 2018

Doctoral candidate:
Kalle Koskinen
Laboratory of Photonics
Faculty of Natural Sciences
Tampere University of Technology
Finland

Supervisor:
Professor Martti Kauranen
Laboratory of Photonics
Faculty of Natural Sciences
Tampere University of Technology
Finland

Pre-examiners:
Professor Isabelle Staude
Institute of Applied Physics
Abbe Center of Photonics
Friedrich Schiller University Jena
Germany

Doctor Jerry Dadap
Department of Electrical Engineering
Columbia University
The United States of America

Opponent:
Professor Thierry Verbiest
Molecular Imaging and Photonics
Faculty of Bioengineering Sciences
Katholieke Universiteit Leuven
Belgium

ISBN 978-952-15-4209-1 (printed)
ISBN 978-952-15-4233-6 (PDF)
ISSN 1459-2045

ABSTRACT

Second-harmonic generation is a second-order nonlinear optical process that can be utilized in a variety of applications. The main limitation of second-harmonic generation is that it is forbidden for centrosymmetric materials. Enabled by the advances in nanofabrication, considerable amount of attention has been given to the miniaturization of optical components for integrated photonics. As a result, the expansion of the range of second-order materials is more desirable than ever.

In this work, we developed a sophisticated analytical model to characterize the second-harmonic response of thin films using various traditional experimental methods. A thin material system brings forth additional complexity due to the presence of reflections that have significant consequences to the nonlinear characterization process both qualitatively and quantitatively. Using the developed model, we studied second-harmonic generation from various material candidates in order to determine whether they have potential as novel nonlinear materials. These materials are composites consisting of multiple alternating dielectric layers, silicon nitride, indium selenide, and gold nanoparticle films coated with titanium dioxide.

The results of this work indicate, that 1) multilayered composites are in fact a promising solution to circumvent the requirement for non-centrosymmetry of second-harmonic generation, 2) indium selenide was found to possess a significant second-harmonic response and to show potential for nonlinear applications, 3) the already strong second-harmonic generation from silicon nitride was enhanced six-fold by material composition, and 4) the second-harmonic response from gold nanoisland films was enhanced 40-fold by a novel non-resonant local-field enhancement process, controlled by tuning the thickness of dielectric coating covering the nanoislands. Lastly, the utility of the developed model was demonstrated by showing that using a traditional simpler model that neglects reflections results in both qualitatively and quantitatively erroneous results in the recognition of multipolar contributions to second-harmonic generation from thin films. In addition, the general nature of the model was highlighted by the fact that the same model was used successfully to analyse the various different experimental configurations used in this work.

TIIVISTELMÄ

Taajuudenkahdennus on toisen kertaluvun epälineaarinen optinen prosessi jota voidaan hyödyntää monissa sovelluksissa. Taajuudenkahdennuksen tärkein rajoite on se, että prosessi on kielletty keskeissymmetrisissä materiaaleissa. Nanoteknologian kehityksen mahdollistamana optisten laitteiden miniaturisointi integroidun fotoniikan tarpeisiin on saanut osakseen suuren määrän huomiota. Tästä syystä uusien toisen kertaluvun epälineaaristen materiaalien löytäminen olisi erityisen hyödyllistä.

Tässä työssä kehitettiin hienostunut analyyttinen malli ohutkalvojen toisen kertaluvun epälineaarisen vasteen karakterisointiin käyttäen erinäisiä tyypillisiä mittaustekniikoita. Ohutkalvojen analysointi on erityisen haasteellista, koska niiden äärimmäisen pieni paksuus johtaa monimutkaisiin heijastusilmiöihin joilla on edelleen merkittävä vaikutus karakterisointiprosessiin sekä kvalitatiivisesti että kvantitatiivisesti. Työssä tutkittiin taajuudenkahdennusta erinäisistä materiaaleista ja niiden potentiaalia uusina epälineaarisina materiaaleina käyttäen kehitettyä mallia. Tutkittavat materiaalit olivat useista ultraohuista kalvoista sykleinä koostuva komposiittikalvo, piinitridi, indiumselenidi ja titaanidioksiidilla päällystetty kultananopartikkelikalvo.

Työn tulokset osoittavat, että: 1) komposiittikalvot ovat lupaava metamateriaaliryhmä taajuudenkahdennuksen keskeissymmetriarajoitteiden kiertämiseksi, 2) indiumselenidin taajuudenkahdennusvaste on merkittävä ja näin ollen indiumselenidi on potentiaalinen materiaali epälineaarisiin optisiin sovelluksiin, 3) piinitridin voimakasta taajuudenkahdennusvastetta voidaan vahvistaa entisestään jopa kuusinkertaiseksi säätämällä piinitridin kemiallista koostumusta ja 4) kultananohiukkaskalvon taajuudenkahdennusvaste voidaan kasvattaa jopa 40-kertaiseksi uudenlaisen epäresonantin lähikenttäilmiön avuttaa. Lisäksi kehitettyä hienostunutta mallia verrattiin yksinkertaisempaan heijastusilmiöt laiminlyövään perinteiseen malliin, ja yksinkertaisen mallin havaittiin tuottavan sekä kvalitatiivisesti että kvantitatiivisesti virheellisiä tuloksia ohutkalvojen multipoli-taajuudenkahdennuksen karakterisoinnissa. Kehitettyä mallia käytettiin kaikkien työn tulosten analysointiin, mikä kuvastaa mallin yleistä luonnetta.

PREFACE

The research related to this Thesis was carried out at the Laboratory of Photonics under the Faculty of Natural Sciences in Tampere University of Technology. The Thesis work was mainly funded by a personal fellowship from Vilho, Yrjö and Kalle Väisälä Foundation administered by the Finnish Academy of Sciences, for which I am extremely grateful.

I would like express my heartfelt gratitude towards my supervisor professor Martti Kauranen, whose superb expertise, kindness and patience have been invaluable. In addition, I thank all of my co-authors with whom the research to which this Thesis is based on was conducted, as well as all of my colleagues in the amazing environment of the Laboratory of Photonics. Finally, my beloved family and friends, without whose support this work would have not been possible, deserve all the praise I can possibly give.

This has truly been an enjoying and interesting ride; I did not really feel its length. As this Thesis work is approaching its conclusion, so is, in a way, a chapter in my life. Indeed, it is with excitement but also with a certain longing that I approach this milestone. I believe, that this experience as a whole has taught me much, molded me, even. I know, that I will cherish the memories of this journey, and never forget them.

Tampere 25.9.2018

Kalle Koskinen

CONTENTS

SYMBOLS AND ABBREVIATIONS

In this work scalar variables are written in *italics* and vectorial variables in **bold**.

Symbols

A_{xz}	Effective off-diagonal SHG component
$\mathbf{B}$	Magnetic flux density
$\mathbf{B}_{\pm}$	Magnetic flux density of field propagating along ± direction
c	Speed of light
$C^{p/s}$	Fabry-Perot reflection factor
D	Thickness of the nonlinear medium
$\mathbf{D}$	Electric displacement
$\mathbf{E}$	Electric field
$\mathbf{E}_{\mathrm{L}}$	Local non-propagating response
$\mathbf{E}_{\pm}$	Electric field propagating along ± direction
$\mathbf{E}_{\mathrm{T}\pm}$	Total electric field propagating along ± direction
$\mathbf{E}_{\mathrm{out}}$	Total SHG field leaving the medium
$f^{\zeta,\eta,\kappa}$	Polarization signature describing ζ polarized SHG from η and κ polarized fundamental fields
$\mathbf{G}$	Dyadic Green's function
$H(z)$	Heaviside step function
$\mathbf{H}$	Magnetic field
I	Irradiance
i	Imaginary unit
J	Local field factor

k	Wave number
$K_\pm^{p/s}$	Factor connecting the p/s-polarized fundamental field incident to the medium with the total $\pm$ propagating p/s field
k_x	Transverse component of the wave vector
$\mathbf{k}$	Wave vector
$\underline{K}_\pm^{p/s}$	Factor describing the contribution of $\pm$ propagating SHG field to the total downward propagating SHG field leaving the medium
$\mathbf{k}_\pm$	Wave vector of field propagating along $\pm$ direction
$\hat{k}_\pm$	Unit vector along the wave vector of field propagating in $\pm$ direction
L_{abc}	Projection of unit polarization vector $a \in \{\hat{\mathbf{p}}_c, \hat{\mathbf{s}}\}$ of $c \in \{\pm\}$ propagating fundamental field to vector $b \in \{\hat{\mathbf{x}}, \hat{\mathbf{y}}, \hat{\mathbf{z}}\}$
$\underline{L}_{abc}$	Projection of unit vector $b \in \{\hat{\mathbf{x}}, \hat{\mathbf{y}}, \hat{\mathbf{z}}\}$ to polarization vector $a \in \{\underline{\hat{\mathbf{p}}}_c, \underline{\hat{\mathbf{s}}}\}$ of $c \in \{\pm\}$ propagating SHG field
$\mathbf{M}$	Magnetization
n	Refractive index
$\hat{p}_\pm$	Unit vector along the p-polarization of field propagating in $\pm$ direction
$\mathbf{P}$	Material polarization
$\mathbf{P}_0$	Elementary source polarization
$\mathbf{P}^{\mathrm{NL}}$	Nonlinear part of material polarization
$\mathbf{Q}$	Electric quadrupolarization
$\underline{q}$	Quantity q evaluated for second-harmonic generation
$q_{a/b}$	Quantity q evaluated for fundamental field a/b
$\mathbf{r}$	Spatial coordinate
r_{it}^p	The Fresnel field reflection coefficient for p polarization from medium i to t

r_{it}^{s}	The Fresnel field reflection coefficient for s polarization from medium i to t
$\hat{s}$	Unit vector along the s polarization
t	Time
t_{it}^{p}	The Fresnel field transmission coefficient for p polarization from medium i to t
t_{it}^{s}	The Fresnel field transmission coefficient for s polarization from medium i to t
$\mathbf{U} = [u_{\xi,\tau}]$	Matrix describing the connection between polarization signatures and SHG susceptibility components
w	Absolute value of the z-component of the wave vector
$w_{\pm}$	z-component of the wave vector for field propagating in ± direction
$\hat{\mathbf{x}}, \hat{\mathbf{y}}, \hat{\mathbf{z}}$	Unit vectors of cartesian coordinates
z_0	z-coordinate of the elementary polarization sheet
ω	Angular frequency
$\chi_e^{(1)}$	Linear electric susceptibility
$\chi_{ijk}^{(2)}$	SHG susceptibility tensor component i, j, k
$\boldsymbol{\chi}^{(2)}$	SHG susceptibility tensor
δ_{ij}	Kronecker delta
$\delta(z)$	Dirac delta function
δ'	Separable multipolar parameter
ϵ_0	Electric permittivity of vacuum
$\Phi_{\phi,\beta,\gamma}$	Phase-mismatch factor for ϕ propagating SHG from β and γ propagating fundamental fields
$\Phi'_{\phi,\beta,\gamma}$	Phase-mismatch factor for ϕ propagating SHG from β and γ propagating fundamental fields a and b, respectively

μ_0	Magnetic permeability of vacuum
θ	Angle of propagation
$[a \leftrightarrow b]$	Term with field subscripts a, b interchanged
c.c.	Complex conjugate term
∇	Differential operator

Abbreviations

ALD	Atomic layer deposition
BS	Beam splitter
CMOS	Complementary metal-oxide semiconductor
ED	Electric-dipole
HWP	Half-wave plate
InSe	Indium selenide
LF	Local field
LPCVD	Low pressure chemical vapor deposition
LP	Linear polarizer
MCM	Multilayer composite material
MNS	Metal nanostructures and metal-dielectric composites
MP	Multipole
PECVD	Plasma-enhanced chemical vapor deposition
PMT	Photomultiplier tube
QWP	Quarter-wave plate
RF	Radio frequency
SHG	Second-harmonic generation
SiN	Silicon nitride

LIST OF PUBLICATIONS

Publication I Stéphane Clemmen, Artur Hermans, Eduardo Solano, Jolien Dendooven, Kalle Koskinen, Martti Kauranen, Edouard Brainis, Christophe Detavernier and Roel Baets, "Atomic layer deposited second-order nonlinear optical metamaterial for back-end integration with CMOS-compatible nanophotonic circuitry," *Optics Letters* **40**, 5371-5374 (2015) [1]

Publication II Kalle Koskinen, Robert Czaplicki, Tommi Kaplas and Martti Kauranen, "Recognition of multipolar second-order nonlinearities in thin-film samples," *Optics Express* **24**, 4972-4978 (2016) [2]

Publication III Kalle Koskinen, Abdallah Slablab, Sasi Divya, Robert Czaplicki, Semen Chervinskii, Madanan Kailasnath, Padmanabhan Radhakrishnan and Martti Kauranen, "Bulk second-harmonic generation from thermally evaporated indium selenide thin films," *Optics Letters* **42**, 1076-1079 (2017) [3]

Publication IV Kalle Koskinen, Robert Czaplicki, Abdallah Slablab, Tingyin Ning, Artur Hermans, Bart Kuyken, Vinita Mittal, Ganapathy Senthil Murugan, Tapio Niemi, Roel Baets and Martti Kauranen, "Enhancement of bulk second-harmonic generation from silicon nitride films by material composition," *Optics Letters* **42**, 5030-5033 (2017) [4]

Publication V Semyon Chervinskii, Kalle Koskinen, Sergey Scherbak, Martti Kauranen and Andrey Lipovskii, "Nonresonant local fields enhance second-harmonic generation from metal nanoislands with dielectric cover," *Physical Review Letters* **120**, 113902 (2018) [5]

AUTHOR'S CONTRIBUTION

Publication I The author provided some consulting on the planning of the nonlinear experiment and significant consulting on the nonlinear analysis. The author conducted experiments and analysis on the calibration of the glass substrate. S.C, A.H., E.S., and J.D conducted the rest of the experiments and analysis and wrote most of the paper. The author contributed to the writing process via comments, corrections and consultation. All co-authors provided valuable insights on the writing process.

Publication II The author planned the experiments, conducted the nonlinear experiments, conducted all of the analysis and wrote the manuscript. R.C. provided help with the experiments, T.K. conducted the linear experiments, and all co-authors provided valuable insights on the writing process.

Publication III The author contributed considerably to the planning of the experiments, conducted approximately half of the nonlinear experiments, conducted all of the nonlinear analysis and wrote approximately 60% of the manuscript. A.S. wrote the rest of the manuscript and provided valuable assistance with experiments, S.D. fabricated the samples, R.C. provided help with the experiments, S.C. conducted the linear experiments and all co-authors provided valuable insights on the writing process.

Publication IV The author contributed considerably to the planning of the experiments, conducted almost all of the nonlinear experiments, conducted all of the nonlinear analysis and wrote approximately 90% of the manuscript. R.C. provided particularly valuable insights and wrote a small portion of the manuscript, and A.S. helped with the nonlinear experiments. T. Niemi, A.H. and B.K. fabricated the samples, V.M and G.S.M. conducted the loss measurements, and T. Ning provided help with the writing. All co-authors provided valuable insights on the writing process.

Publication V The author contributed considerably to the planning of the experiments, conducted all of the nonlinear experiments and conducted all of the nonlinear analysis. The author wrote a small portion of the manuscript and contributed to the writing process via comments, corrections and consultation. S.C. fabricated the samples, S.S. conducted the modelling and all co-authors provided valuable insights on the writing process.

1. INTRODUCTION

The field of nonlinear optics is defined by the study of phenomena where the optical response of a material depends on the interacting optical fields in a nonlinear manner, which occurs in the presence of intense light fields [6]. Thus, it is unsurprising that the invention of laser marks the *de facto* beginning of nonlinear optics [7], as evidenced by the consequent emergence of multiple observations of nonlinear optical effects such as second-harmonic generation [8–14]. The observation of other nonlinear effects such as third-harmonic generation, sum-frequency generation and difference-frequency generation soon followed [9, 15, 16]. However, second-order effects, such as second-harmonic generation, are the lowest-order coherent frequency conversion processes and thus remain interesting due to the gradual weakening of the nonlinear effects with increasing order of nonlinearity [6, 17].

Second-harmonic generation is an instantaneous process where two incident photons at a fundamental frequency are annihilated and one photon at the doubled frequency is generated [6, 18]. Under the electric-dipole approximation of the light-matter interaction, the process is governed by a polar third-rank tensor and is thus forbidden for centrosymmetric materials [17, 19]. For this reason, studies of second-harmonic generation have been limited to systems of lower symmetry, such as surfaces [11, 12, 14], crystals [8, 9, 20–22] and for example chiral molecules [23–26]. It should be noted that this limitation can become advantageous when the goal is to probe surface or symmetry features of a material [27–29]. However, if high nonlinearity is required, the non-centrosymmetry requirement remains an important problem. Several methods have been utilized to artificially create materials with high second-order nonlinearity, such as poling [30–33], Mie-resonant structures [34], resonant dielectric structures [35], symmetry-breaking strain [36–38], stacking of ultrathin layers [39, 40], plasmon enhancement in metal nanostructures [41] and utilizing multipolar (magnetic-dipole and electric-quadrupole) contributions to the second-order nonlinear response [42].

Due to advancements in nanofabrication during recent decades, the miniaturization of optical devices has become more realistic [43–45]. As a consequence, there has been considerable attention towards integrated photonics, i.e., the integration of multiple photonic devices together on a substrate [46–50]. Silicon on insulator is often used as the basis of these devices, as it enables the use of the existing complementary metal-oxide semiconductor infrastructure established for integrated electronic circuits [43, 46–48]. As some of the desired functionalities for these photonic devices rely on second-order effects [51–56], expanding the range of suitable nonlinear materials has become even more desirable.

In order to expand the range of nonlinear materials, an experimental methodology for the nonlinear characterizaton of the candidate materials must be established. The characterization is often most convenient to do by using thin-film samples. The second-harmonic response of a material is then typically characterized by an experiment where the polarizations of the fundamental beam and the second-harmonic beam as well as the angle of incidence are controlled in order to access the various susceptibility tensor components of the material [26, 57–59]. The most traditional method, known as the Maker-fringe method, utilizes variable angle of incidence for fixed choices of polarization for the fundamental and detected SHG beam [57, 58]. This method has been further extended to account for absorption and birefringence [60]. Another approach is to have the angle of incidence fixed while conducting multiple measurements with different combinations of the polarization of the fundamental and SHG beams [26].

Lastly, it was discovered early that if magnetic-dipole and electric-quadrupole contributions are taken into account, second-harmonic generation is allowed even in centrosymmetric media [17, 61, 62]. The separation of these contibutions from the electric-dipole contribution of the material surface has been a long-standing problem in nonlinear optics [59, 63]. However, it was later found out that this could be done by second-harmonic generation based on the use of two non-collinear excitation beams at the fundamental frequency [64–67].

1.1 Research objectives and scope of the Thesis

As discussed above, expansion of the range of novel nonlinear materials is highly desirable and second-order nonlinear materials are particularly hard to come by due to the symmetry restrictions associated with second-order processes. Thus, the ultimate research objective of this work is to expand the range of materials with high second-order response.

We limit our research methodology to the consideration of the second-harmonic response, as its presence already indicates that the symmetry restrictions are overcome. In addition, due to the physical similarities between second-harmonic generation and other second-order processes, it is likely that a material with a strong second-harmonic response exhibits high second-order nonlinearity in general. This limitation of scope is highly beneficial for the practical experimental methodology and the associated analysis.

Our ultimate research objective can be separated into 3 sub-objectives all contributing to the ultimate objective: 1) Finding a high second-harmonic response from a material that was previously unknown to possess one, 2) Finding a method to enhance the second-harmonic response of a material that was previously known to possess one, and 3) Improving the experimental methodology of nonlinear characterization, contributing to the ultimate objective.

In order to determine the nonlinear response, we utilize the experiments presented in Refs. [26, 57] and expand the analysis to the case of thin films using the theoretical framework presented in Ref. [68]. In addition, we apply the aforementioned theoretical framework in conjunction with the analysis presented in Ref. [69] for two non-collinear fundamental beams for the case of thin films, and use experiments presented in Ref. [64] to probe the multipolar contribution to the second-harmonic generation. In addition to enabling the research, the development of these models falls under sub-objective 3.

In this work, we studied the following material candidates: i) A metamaterial consisting of cycles of alternating dielectric layers, ii) silicon nitride, iii) indium selenide and iv) gold nanoisland films coated with titanium dioxide.

The choice for material (i) was inspired by the recent results on a similar multilayered structure presented in Ref. [40]. We aimed to improve upon the previous design in order to enhance the second-harmonic response using the guidelines presented in Ref. [70]. In addition, this research will serve to verify or question the previous results, and falls under sub-objective 2.

The choice for material (ii) was motivated by the recent results on high second-harmonic response from silicon nitride presented in Ref. [71]. We aimed to study samples of different material compositions in order to determine whether the second-harmonic response can be enhanced by tuning the material composition. In addition, we aimed to probe the presence and relative strength of the multipolar contribution to second-harmonic generation from silicon nitride. These topics fall under sub-objective 2.

The choice for material (iii) was motivated by a previous report of optical nonlinearity presented in Ref. [72] in conjunction with reports of its flexible phases presented in Ref. [73], potentially enabling favourable symmetry breaking. We aimed to study multiple thin films of indium selenide in order to determine its second-harmonic response, if any is present. This falls under sub-objective 1.

The choice for material (iv) was motivated by the well-documented high enhancement of second-harmonic generation from metal nanostructures by plasmon resonance driven local fields, presented for example in Ref. [74]. We aimed to determine whether this enhancement could be accomplished by tuning the thickness of the titanium dioxide coating of gold nanoisland films. This falls under sub-objective 2.

1.2 Structure of the Thesis

This dissertation consists of six chapters including this one. Chapters 2 and 3 provide the theoretical framework for the analysis and design of experiments specified in Chapter 4. The results of the experiments are described and analysed in Chapter 5. Chapter 6 concludes the work with a summary and a brief outlook to the future.

In Chapter 2, we examine the fundamental principles of the optics of thin layers embedded between dielectric media. Starting from the Maxwell's and Fresnel's equations, the description of the total electric field inside the layer is derived for the case of a plane wave input from outside the layer. Lastly, we describe the total field originating from a nonlinear polarization source within the layer. This serves as important groundwork for the analysis of second-harmonic generation from thin layers treated in the following chapter.

In Chapter 3, we look into the nonlinear polarization for the case of a plane-wave excitation and determine the total second-harmonic field generated within a thin nonlinear layer. In addition, second-harmonic generation for two fundamental fields is examined. In both cases, the second-harmonic generation field is described in terms of its polarization components and with respect to the polarization components of the input field(s) in order to analyse the nonlinear experiments described in the following chapter.

Chapter 4 describes the experimental methodology of this work. This includes a detailed description of the experimental arrangements, an overview of the studied materials, and an explanation of the motivations behind the chosen methodology. Lastly, the particular experiments are explicitly specified.

In Chapter 5, the results of all of the experiments outlined in Chapter 4 are described in detail and analysed using the theoretical results of Chapter 3. The particular weaknesses and strengths of both the experiments and the analysis are assessed. Finally, the key results are laid out in a logical manner and their scientific impact is discussed.

Lastly, Chapter 6 contains concluding remarks about the research as a whole, discussion about the results with respect to our objectives and an outlook to the potential future of the research.

2. OPTICS OF LAYERED STRUCTURES

In this chapter, we examine the basic optical phenomena in layered structures. In this context, the term layered structure denotes a system which consists of multiple well-defined media that are separated from each other by parallel interfaces. We will start by writing down Maxwell's equations and deriving the wave equation for homogeneous media. Next, we will write down the basic laws of refraction and reflection, followed by the expression of the homogeneous solution for a layered system. We will then utilize the Green's function formalism for nonlinear optics to write the field generated from a nonlinear source similarly to what was done in Ref. [68]. Finally, we combine all of the above in order to describe the field generated outside the system with respect to the nonlinear source.

2.1 Maxwell's equations and the homogeneous wave equation

In this section, we write down the Maxwell's equations under electric-dipole (ED) approximation for a non-magnetic system without free charges or currents as well as formulate and solve the wave equation for a homogeneous material. These results will provide the foundation for the more specific analysis ahead.

In the classical regime, the physics of light in matter is governed by Maxwell's equations [75]. In this work, all bulk media are assumed to consist of dielectric materials, and thus exhibit no free charges or currents. For such materials, Maxwell's equations can be written as [6]

$$\nabla \cdot \mathbf{D}(\mathbf{r},t) = 0 \tag{2.1a}$$

$$\nabla \cdot \mathbf{B}(\mathbf{r},t) = 0 \tag{2.1b}$$

$$\nabla \times \mathbf{E}(\mathbf{r},t) = -\frac{\partial \mathbf{B}(\mathbf{r},t)}{\partial t} \tag{2.1c}$$

$$\nabla \times \mathbf{H}(\mathbf{r},t) = \frac{\partial \mathbf{D}(\mathbf{r},t)}{\partial t}, \tag{2.1d}$$

where **D** denotes the electric displacement, **B** denotes the magnetic flux density, **E** denotes the electric field, **H** denotes the magnetic field, **r** denotes the spatial coordinate and t denotes time. The relationships between the two pairs of electric $(\mathbf{E}, \mathbf{D})$ and magnetic $(\mathbf{B}, \mathbf{H})$ quantities describe the electric and magnetic interactions between light and matter, respectively. Mathematically, they can be connected via constitutive equations. The constitutive equations can be written for a nonmagnetic medium under the ED approximation as [76]

$$\mathbf{D}(\mathbf{r}, t) = \epsilon_0 \mathbf{E}(\mathbf{r}, t) + \mathbf{P}(\mathbf{r}, t) \tag{2.2a}$$

$$\mathbf{H}(\mathbf{r}, t) = \frac{1}{\mu_0} \mathbf{B}(\mathbf{r}, t), \tag{2.2b}$$

where ϵ_0 is the electric permittivity of vacuum, μ_0 is the magnetic permeability of vacuum and **P** is the material polarization. In this section, we will consider the case where the material polarization is linearly dependent on the electric field and can be written as

$$\mathbf{P}(\mathbf{r}, t) = \epsilon_0 \chi_e^{(1)} \mathbf{E}(\mathbf{r}, t), \tag{2.3}$$

where $\chi_e^{(1)}$ is the linear electric susceptibility. It should be noted that generally the linear electric susceptibility is a tensorial quantity. However, we will assume that the medium is isotropic in the linear regime.

In order to proceed, we assume that all of the above time-dependent quantities can be treated in terms of their frequency components, i.e.,

$$f(\mathbf{r}, t) = f(\mathbf{r}) \mathrm{e}^{-i\omega t} + \text{c.c.}, \tag{2.4}$$

where c.c. denotes the complex conjugate and ω is the angular frequency of the respective quantity. This is justified because in the context of this work, only coherent light sources and processes are considered and thus all light can be separated into sufficiently discrete frequency components. From here on, we treat the fields implicitly in terms of their frequency components and consider any frequency mixing explicitly when required. As a result, the temporal behavior of the Maxwell's equations is greatly simplified. By combining the Eq. (2.1) with Eqs. (2.2, 2.3), the simplified set of Maxwell's equations can be written as

$$\begin{aligned}
\nabla \cdot \mathbf{E}(\mathbf{r}) &= 0 && \text{(2.5a)}\\
\nabla \cdot \mathbf{B}(\mathbf{r}) &= 0 && \text{(2.5b)}\\
\nabla \times \mathbf{E}(\mathbf{r}) &= i\omega \mathbf{B}(\mathbf{r}) && \text{(2.5c)}\\
\nabla \times \mathbf{B}(\mathbf{r}) &= -i\frac{\omega n^2}{c^2}\mathbf{E}(\mathbf{r}), && \text{(2.5d)}
\end{aligned}$$

where $c = 1/\sqrt{\epsilon_0 \mu_0}$ is the speed of light and $n^2 = (1 + \chi_e^{(1)})$ is the refractive index.

By using Eq. (2.5d), the vector identity $\nabla \times \nabla \times = \nabla(\nabla \cdot\,) - \nabla^2$ and Eq. (2.5a), the curl of Eq. (2.5c) yields

$$\nabla^2 \mathbf{E}(\mathbf{r}) + \omega^2 \frac{n^2}{c^2} \mathbf{E}(\mathbf{r}) = 0, \tag{2.6}$$

which is the standard Helmholz equation for a homogeneous medium. The equation is satisfied by the plane wave

$$\mathbf{E}(\mathbf{r}) = \mathbf{E}\mathrm{e}^{i\mathbf{k}\cdot\mathbf{r}} \tag{2.7}$$

provided that the condition

$$\mathbf{k} \cdot \mathbf{k} = n^2 \omega^2 / c^2 = k^2 \tag{2.8}$$

holds, where k is the magnitude of the wave vector.

2.2 Refraction and reflection

We will begin this section by writing down the basic laws of refraction and reflection. Firstly, the angle of reflection of light at an interface is equal to the angle of incidence. Secondly, the refraction of light at an interface between two media is governed by the Snell's law [77]

$$n_i \sin \theta_i = n_t \sin \theta_t, \tag{2.9}$$

where n_i and n_t (θ_i and θ_t) are the refractive indices of (propagation angles in) the media before and after the interface, respectively.

The quantitative reflection and transmission of light at an interface are governed by the Fresnel equations. The Fresnel coefficients for fields describe the ratio between transmitted and reflected fields with respect to the incident field, and are given

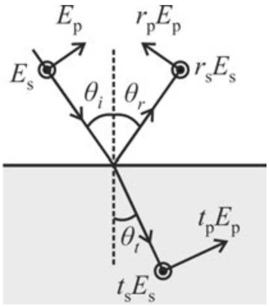

Figure 2.1: A schematic of the geometry of an interface and the notation used for the Snell's law and the Fresnel equations.

by [77]

$$
\begin{aligned}
r_{it}^{p} &= \frac{n_t\cos\theta_i - n_i\cos\theta_t}{n_t\cos\theta_i + n_i\cos\theta_t} && \text{(2.10a)}\\
r_{it}^{s} &= \frac{n_i\cos\theta_i - n_t\cos\theta_t}{n_i\cos\theta_i + n_t\cos\theta_t} && \text{(2.10b)}\\
t_{it}^{p} &= \frac{2n_i\cos\theta_i}{n_i\cos\theta_t + n_t\cos\theta_i} && \text{(2.10c)}\\
t_{it}^{s} &= \frac{2n_i\cos\theta_i}{n_i\cos\theta_i + n_t\cos\theta_t}, && \text{(2.10d)}
\end{aligned}
$$

where r denotes the Fresnel reflection coefficient, t denotes the Fresnel transmission coefficient, superscript p (s) denotes polarization component parallel (perpendicular) to the plane of incidence and subscript i (t) denotes the medium before (after) the interface. A schematic of the geometry is shown in (Fig. 2.1).

Before proceeding further, it is useful to define the coordinate system for the material. In this work, we focus on systems that 1) consist of layers whose interfaces are parallel to each other, 2) exhibit at least in-plane isotropy along planes parallel to the interfaces and 3) exhibit negligible birefringence. If the normal to the interfaces is defined as z and a plane wave propagates at an oblique angle with respect to z, x axis can be chosen in such a way that the wave vector of the plane wave lies in the (x, z)-plane. Thus, the wave vector of the plane wave can be written as

$$\mathbf{k} = k_x\hat{x} + k_z\hat{z}, \tag{2.11}$$

where k_x and k_z are the x and z components of the wave vector. Due to the limitations applied to the medium (requirements 1, 3), different spatial frequency

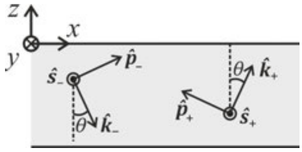

Figure 2.2: A schematic of the coordinate systems used for the material system (x, y, z) and the wave solutions $(p_\pm, s, k_\pm)$.

components defined by k_x do not mix, which is very convenient for the following analysis. In the rest of this chapter, all spatially dependent quantities will be treated with respect to the single spatial frequency component k_x unless otherwise explicitly stated.

By substituting Eq. (2.11) into the condition imposed by the wave equation Eq. (2.8), two solutions appear and are given by

$$\mathbf{k}_\pm = k_x\hat{x} + w_\pm\hat{z}, \tag{2.12}$$

with

$$w_\pm = \pm w = \pm\sqrt{\left(\frac{n\omega}{c}\right)^2 - k_x^2}, \tag{2.13}$$

where $w_\pm$ represents the two solutions for the z-component of the wave vector for a given k_x. From this point on, the (+)-solution is labeled as *upward* propagating wave and (−)-solution as *downward* propagating wave.

Lastly, we will define the polarization coordinates of the plane wave and combine them with the wave vector into a single right-handed orthogonal system given by

$$\begin{bmatrix} \hat{p}_\pm \\ \hat{s} \\ \hat{k}_\pm \end{bmatrix} = \begin{bmatrix} \mp\cos\theta & 0 & \sin\theta \\ 0 & -1 & 0 \\ \sin\theta & 0 & \pm\cos\theta \end{bmatrix} \begin{bmatrix} \hat{x} \\ \hat{y} \\ \hat{z} \end{bmatrix}, \tag{2.14}$$

where $\hat{p}_+$ ($\hat{p}_-$) and $\hat{k}_+$ ($\hat{k}_-$) are the unit vector for p-polarized component and the wave vector of upward (downward) propagating wave, respectively. In addition, $\hat{s}$ is the unit vector for s-polarized component of the wave. From the above definition, we have also defined the propagation angle theta so that at $\theta = 0$, the unit wave vector is given by $\hat{k}_\pm = \pm\hat{z}$. A schematic of the coordinate systems is shown in (Fig. 2.2).

By expanding the electric field of the wave in terms of its polarization components, noting that the wave is transverse (see Eq. 2.5a) and substituting Eq. (2.11), the upward and downward propagating solutions can be expressed as

$$\mathbf{E}_{\pm}(\mathbf{r}) = (E^{p\pm}\hat{p}_{\pm} + E^{s\pm}\hat{s})\mathrm{e}^{i\mathbf{k}_{\pm}\cdot\mathbf{r}}, \tag{2.15}$$

where $E^{p\pm}$ and $E^{s\pm}$ are the amplitudes of the p and s polarized components of the electric fields propagating along $\mathbf{k}_{\pm}$. By substituting Eq. (2.15) to Eq. (2.5c), a similar expression is obtained for the magnetic flux density but in terms of electric field amplitudes

$$\mathbf{B}_{\pm}(\mathbf{r}) = \frac{n}{c}(-E^{s\pm}\hat{p}_{\pm} + E^{p\pm}\hat{s})\mathrm{e}^{i\mathbf{k}_{\pm}\cdot\mathbf{r}}. \tag{2.16}$$

Equations Eq. (2.15) and Eq. (2.16) represent solutions for the electric and magnetic fields of a propagating wave characterized by the spatial frequency k_x in a homogeneous system, and are the main result of this section.

2.3 Green's function formalism

In this section, we will utilize Green's function formalism to solve Maxwell's equations for a system where a source polarization term is present. The approach follows closely to what was published in Ref. [68]. First, let us write the total polarization as a sum of a linear polarization term as described by Eq. (2.3) and a nonlinear term as

$$\mathbf{P}(\mathbf{r},t) = \epsilon_0\chi_e^{(1)}\mathbf{E}(\mathbf{r},t) + \mathbf{P}^{\mathrm{NL}}(\mathbf{r},t). \tag{2.17}$$

By substituting Eq. (2.17) into the constitutive equations and following an approach similar to the one used for the homogeneous case, Maxwell's equations can be expressed as

$$\begin{aligned}
\nabla\cdot\mathbf{D}(\mathbf{r}) &= 0 && \text{(2.18a)}\\
\nabla\cdot\mathbf{B}(\mathbf{r}) &= 0 && \text{(2.18b)}\\
\nabla\times\mathbf{E}(\mathbf{r}) &= i\omega\mathbf{B}(\mathbf{r}) && \text{(2.18c)}\\
\nabla\times\mathbf{B}(\mathbf{r}) &= -i\frac{\omega}{c^2}(n^2\mathbf{E}(\mathbf{r}) + \frac{1}{\epsilon_0}\mathbf{P}^{\mathrm{NL}}(\mathbf{r})). && \text{(2.18d)}
\end{aligned}$$

In order to solve Eqs. (2.18), let us consider an elementary source polarization sheet at some $z = z_0$ and of the form

$$\mathbf{P}^{\mathrm{NL}}(\mathbf{r}) = \mathbf{P}_0 \delta(z - z_0) \mathrm{e}^{ik_x x}, \tag{2.19}$$

where $\mathbf{P}_0$ is the magnitude of the source polarization and δ is the Dirac delta function. Due to the infinitesimal thickness of the source sheet, the previous homogeneous solutions described by Eqs. (2.15) and (2.16) also hold here when $z \neq z_0$. Furthermore, such a source cannot directly affect fields that are below the source sheet and are propagating upward. Similarly, the source cannot directly affect fields that are above the source sheet and are propagating downward. Thus, we try an ansatz

$$\begin{aligned} \mathbf{E}(\mathbf{r}) = {} & \mathbf{E}_+(\mathbf{r}) \mathrm{e}^{iw_- z_0} H(z - z_0) + \mathbf{E}_-(\mathbf{r}) \mathrm{e}^{iw_+ z_0} H(z_0 - z) \\ & + \mathbf{E}_{\mathrm{L}} \delta(z - z_0) \mathrm{e}^{ik_x x} \end{aligned} \tag{2.20}$$

$$\mathbf{B}(\mathbf{r}) = \mathbf{B}_+(\mathbf{r}) \mathrm{e}^{iw_- z_0} H(z - z_0) + \mathbf{B}_-(\mathbf{r}) \mathrm{e}^{iw_+ z_0} H(z_0 - z), \tag{2.21}$$

where $H(z)$ is the Heaviside step function, $\mathbf{E}_{\mathrm{L}}$ is the local non-propagating response, $\mathbf{E}_\pm(\mathbf{r})$ denote the homogeneous solutions for the electric field (see Eq. 2.15) and $\mathbf{B}_\pm(\mathbf{r})$ denote the homogeneous solution for the magnetic field (see Eq. 2.16). In order to determine the upward and downward propagating field components $E^{p\pm}$ and $E^{s\pm}$ with respect to the source term $\mathbf{P}_0$, Eqs. (2.20) and (2.21) are substituted to Eqs. (2.18c) and (2.18d), which yields

$$\begin{aligned} \nabla \times \mathbf{E}(\mathbf{r}) = {} & \delta(z - z_0) \left(\hat{s} E^p_+ \frac{w_+}{k} + \hat{x} E^s_+ \right) \\ & - \delta(z - z_0) \left(\hat{s} E^p_- \frac{w_-}{k} + \hat{x} E^s_- \right) \\ & + ik_x \delta(z - z_0) \left(-\hat{z} E^s_{\mathrm{L}} + \hat{s} E^z_{\mathrm{L}} \right) \\ & + \frac{\partial}{\partial z} \delta(z - z_0) (\hat{x} E^s_{\mathrm{L}} - \hat{s} E^x_{\mathrm{L}}) = 0, \end{aligned} \tag{2.22}$$

$$\begin{aligned} \nabla \times \mathbf{B}(\mathbf{r}) = {} & \delta(z - z_0) \frac{n}{c} \left(\hat{x} E^p_+ - \hat{s} E^s_+ \frac{w_+}{k} \right) \\ & - \delta(z - z_0) \frac{n}{c} \left(\hat{x} E^p_- + \hat{s} E^s_- \frac{w_+}{k} \right) \\ = {} & -\delta(z - z_0) \frac{i\omega n^2}{c^2} \mathbf{E}_{\mathrm{L}} - \delta(z - z_0) \frac{i\omega}{c^2 \epsilon_0} \mathbf{P}_0, \end{aligned} \tag{2.23}$$

By matching the different singular terms and vector components, the field amplitudes are found to be

$$\begin{aligned} E^{s+} &= E^{s-} = \frac{i\omega^2}{2\epsilon_0 c^2 w} P_0^s && (2.24a) \\ E^{p-} &= \frac{i\omega^2}{2\epsilon_0 c^2 w} \hat{p}^+ \cdot \mathbf{P}_0 && (2.24b) \\ E^{p+} &= \frac{i\omega^2}{2\epsilon_0 c^2 w} \hat{p}^- \cdot \mathbf{P}_0, && (2.24c) \end{aligned}$$

where w is the absolute value of the z-component of the wave vector, and the total propagating field generated from the sheet source is found to be

$$\begin{aligned} \mathbf{E}(\mathbf{r}) = \frac{i\omega^2}{2\epsilon_0 c^2 w} & \left(\hat{p}^+\hat{p}^+ \cdot \mathbf{P}_0(z_0) + \hat{s}\hat{s} \cdot \mathbf{P}_0(z_0)\right) \times H(z - z_0) \mathrm{e}^{iw_+(z-z_0)} \mathrm{e}^{ik_x x} \qquad (2.25) \\ + \frac{i\omega^2}{2\epsilon_0 c^2 w} & \left(\hat{p}^-\hat{p}^- \cdot \mathbf{P}_0(z_0) + \hat{s}\hat{s} \cdot \mathbf{P}_0(z_0)\right) \times H(z_0 - z) \mathrm{e}^{iw_-(z-z_0)} \mathrm{e}^{ik_x x}, \end{aligned}$$

where the sheet position z_0 is now explicitly noted to emphasize the fact that Eq. (2.25) describes a field generated by a thin sheet located at z_0. By reorganizing Eq. (2.25), the generated field can be expressed as

$$\mathbf{E}(\mathbf{r}) = \mathbf{G}(z - z_0) \cdot \mathbf{P}(z_0) \mathrm{e}^{ik_x x}, \qquad (2.26)$$

where $\mathbf{G}(z - z_0)$ is a dyadic Green's function describing how a source polarization sheet at z_0 generates a propagating field at an arbitrary z position and is defined as

$$\begin{aligned} \mathbf{G}(z - z_0) = \frac{i\omega^2}{2\epsilon_0 c^2 w} & \left(\hat{p}^+\hat{p}^+ + \hat{s}\hat{s}\right) \times H(z - z_0) \mathrm{e}^{iw_+(z-z_0)} \qquad (2.27) \\ + \frac{i\omega^2}{2\epsilon_0 c^2 w} & \left(\hat{p}^-\hat{p}^- + \hat{s}\hat{s}\right) \times H(z_0 - z) \mathrm{e}^{iw_-(z-z_0)}. \end{aligned}$$

As stated above, the Green's function describes the tensorial relationship between the sheet source polarization and the generated propagating fields for all z. However, another interpretation is that the Green's function describes the generated field at some z by a sheet at an arbitrary location z_0. Due to the superposition principle, the total contribution from a volumetric source can then be determined by integration:

$$\mathbf{E}(\mathbf{r}) = \int_{-\infty}^{\infty} \mathbf{G}(z - z_0) \cdot \mathbf{P}(z_0) \mathrm{e}^{ik_x x} dz_0. \qquad (2.28)$$

Now, Eq. (2.28) describes the generated field at any z from a source polarization distribution specified by $\mathbf{P}(z_0)$, and is the main result of this section.

2.4 Total fields in layerered structures

In this section, we utilize the results of the previous sections for the case of a layer embedded between two dielectric media. We note the three media by numbers 1, 2 and 3 so, that number 2 denotes the layer, number 1 denotes the medium above the layer (towards the positive z) and number 3 denotes the medium below the layer (towards the negative z). Let us begin by studying a plane wave solution given by Eqs. (2.15 and 2.16) within such a layer. As discussed earlier, a portion of light is reflected at interfaces between media of varying refractive indices as dictated by the Fresnel equations Eq. (2.10). The reflected portion acts as a new partial wave whose wave vector does not change except for the z-component changing sign ($w_\pm \rightarrow w_\mp$). Therefore, the wave vector of the reflected part of the upward (downward) field is parallel to the wave vector of the original downward (upward) field, and for the case of a plane wave, these these two partial waves are geometrically inseparable from each other (Fig. 2.3a). Furthermore, the successive reflections occurring for the reflected partial waves result in a family of downward and upward propagating partial waves that are geometrically inseparable from each other.

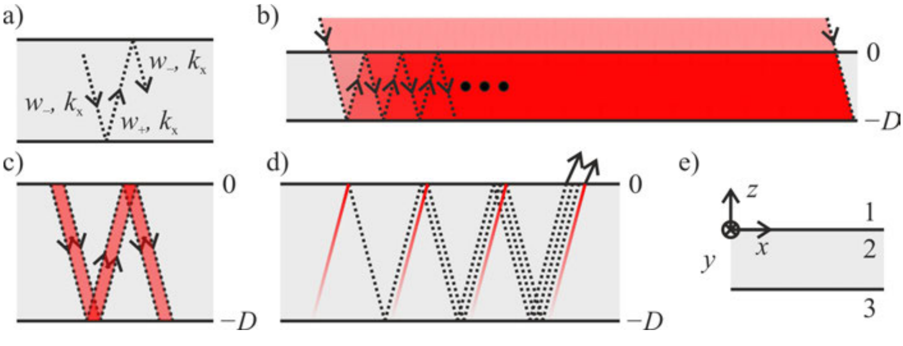

Figure 2.3: A schematic of reflection effects in layers. a) Components of the wave vector for reflected partial waves; b) Reflected waves contributing to one another in a thin layer; c) Reflected waves being geometrically separated and not mixing in a thick layer; d) Contribution principle of multiple reflected partial waves to the total field in a thin layer; e) Coordinate system and labels of media used in this work.

In practice, a light wave is never an infinite plane wave but has some finite beam width W. Consequently, the resulting total field within the layer depends on the relative size of the beam with respect to the layer thickness D. For the case of a thin layer ($D \ll W$), the wave exhibits *plane wave like behavior* within the layer (Fig. 2.3b), and a family of upward and downward propagating partial waves emerges. As a result, a Fabry-Perot etalon like phenomenon occurs [78]. By writing the Fresnel reflection coefficients as r_{21} and r_{23} for the top and bottom interfaces approached by upward and downward propagating beams, respectively, and noting that the total phase difference of the reflection cycle is $2wD$, the field of each subsequent cycle is the field of the previous cycle multiplied by a factor $(r_{21}r_{23}\mathrm{e}^{i2wD})$. Therefore, the total upward (downward) propagating field that arises from an upward (downward) propagating original field can be written as

$$\begin{aligned}\mathbf{E}_{\mathrm{FP}\pm}(z) &= \mathbf{E}_{\pm}(z)\left(1 + (r_{21}r_{23}\mathrm{e}^{i2wD}) + (r_{21}r_{23}\mathrm{e}^{i2wD})^2 + \cdots\right) \quad , \\ &= \mathbf{E}_{\pm}(z)\sum_{l=0}^{\infty}(r_{21}r_{23}\mathrm{e}^{i2wD})^l = \mathbf{E}_{\pm}(z)\frac{1}{1 - r_{21}r_{23}\mathrm{e}^{i2wD}}\end{aligned} \tag{2.29}$$

where the subscript FP refers to Fabry-Perot etalon like behavior, $\mathbf{E}_{\pm}(z) = (\hat{\mathbf{p}}_{\pm}E^p_{\pm} + \hat{\mathbf{s}}E^s_{\pm})\mathrm{e}^{iw_{\pm}z}$ denotes the original upward and downward propagating fields described by Eq. (2.15) with + (−) indicating upward (downward) propagation. These fields can originate for example from outside of the layer or be generated within the layer via nonlinear processes as shown in (Fig. 2.3b) and (Fig. 2.3d), respectively. Noting the above discussion about the upward (downward) propagating field contributing to the downward (upward) propagating field via reflection, the total fields inside the medium can be written as

$$\begin{aligned}\mathbf{E}_{\mathrm{T}+}(z) = \hat{\mathbf{p}}_{+}&\left(E^p_{+}\frac{1}{1 - r^p_{21}r^p_{23}\mathrm{e}^{i2wD}} + E^p_{-}\frac{r^p_{23}\mathrm{e}^{i2wD}}{1 - r^p_{21}r^p_{23}\mathrm{e}^{i2wD}}\right)\mathrm{e}^{iw_{+}z} \\ + \hat{\mathbf{s}}&\left(E^s_{+}\frac{1}{1 - r^s_{21}r^s_{23}\mathrm{e}^{i2wD}} + E^s_{-}\frac{r^s_{23}\mathrm{e}^{2iwD}}{1 - r^s_{21}r^s_{23}\mathrm{e}^{i2wD}}\right)\mathrm{e}^{iw_{+}z}\end{aligned} \tag{2.30}$$

$$\begin{aligned}\mathbf{E}_{\mathrm{T}-}(z) = \hat{\mathbf{p}}_{-}&\left(E^p_{+}\frac{r^p_{21}}{1 - r^p_{21}r^p_{23}\mathrm{e}^{i2wD}} + E^p_{-}\frac{1}{1 - r^p_{21}r^p_{23}\mathrm{e}^{i2wD}}\right)\mathrm{e}^{iw_{-}z} \\ + \hat{\mathbf{s}}&\left(E^s_{+}\frac{r^s_{21}}{1 - r^s_{21}r^s_{23}\mathrm{e}^{i2wD}} + E^s_{-}\frac{1}{1 - r^s_{21}r^s_{23}\mathrm{e}^{i2wD}}\right)\mathrm{e}^{iw_{-}z},\end{aligned} \tag{2.31}$$

where the subscript T refers to the total upward/downward propagating beam inside the layer and where the polarization dependence of Fresnel coefficients is explicitly noted.

For the case of a thick layer ($D \gg W$), the reflected partial waves are geometrically separated from each other and thus separable in experiment, resulting in a *ray like* *behavior* (Fig. 2.3c) where the reflected beams can be neglected.

Let us next examine the light wave generated by a volumetric source spanning over a thin layer surrounded by unknown dielectric media. Using Eq. (2.28), the generated upward and downward propagating fields can be calculated at locations right before the top and bottom interfaces of the source layer, respectively. By setting the top and bottom interfaces at $z = 0$ and $z = -D$, respectively, Eq. (2.28) yields

$$\mathbf{E}_+(0) = \int_{-D}^{0} \mathbf{G}(0 - z_0) \cdot \mathbf{P}(z_0) \mathrm{e}^{ik_x x} dz_0 \tag{2.32a}$$

$$\mathbf{E}_-(-D) = \int_{-D}^{0} \mathbf{G}(-D - z_0) \cdot \mathbf{P}(z_0) \mathrm{e}^{ik_x x} dz_0, \tag{2.32b}$$

where the two fields arise separately from the two different terms of the Green function Eq. (2.27) due to the presence of the Heaviside functions. Furthermore, in the calculation of Eq. (2.32), the fields are assumed to originate exclusively from the source polarization. As above, some portion of the fields is consecutively reflected at the interfaces, giving rise to the mixing of the upward and downward propagating waves as well as etalon factors (Fig. 2.3d). Following a procedure similar to the one used in derivation of Eqs. (2.29, 2.30 and 2.31), the total generated field outside the layer can be written as

$$\begin{aligned}\mathbf{E}_{\mathrm{out}}(0) = \hat{\mathbf{p}}_+ t_{21}^p &\left(E_+^p(0) \frac{1}{1 - r_{21}^p r_{23}^p \mathrm{e}^{i2wD}} + E_-^p(-D) \frac{r_{23}^p \mathrm{e}^{iwD}}{1 - r_{21}^p r_{23}^p \mathrm{e}^{i2wD}} \right) \\ + \hat{\mathbf{s}} t_{21}^s &\left(E_+^s(0) \frac{1}{1 - r_{21}^s r_{23}^s \mathrm{e}^{i2wD}} + E_-^s(-D) \frac{r_{23}^s \mathrm{e}^{iwD}}{1 - r_{21}^s r_{23}^s \mathrm{e}^{i2wD}} \right)\end{aligned} \tag{2.33}$$

$$\begin{aligned}\mathbf{E}_{\mathrm{out}}(-D) = \hat{\mathbf{p}}_- t_{23}^p &\left(E_-^p(-D) \frac{1}{1 - r_{21}^p r_{23}^p \mathrm{e}^{i2wD}} + E_+^p(0) \frac{r_{21}^p \mathrm{e}^{iwD}}{1 - r_{21}^p r_{23}^p \mathrm{e}^{i2wD}} \right) \\ + \hat{\mathbf{s}} t_{23}^s &\left(E_-^s(-D) \frac{1}{1 - r_{21}^s r_{23}^s \mathrm{e}^{i2wD}} + E_+^s(0) \frac{r_{21}^s \mathrm{e}^{iwD}}{1 - r_{21}^s r_{23}^s \mathrm{e}^{i2wD}} \right),\end{aligned} \tag{2.34}$$

where t_{21} and t_{23} are the Fresnel transmission coefficients for the top and bottom interfaces when approached from inside the layer, respectively. By defining a parameter

$$C^{p/s} = \frac{1}{1 - r_{21}^{p/s} r_{23}^{p/s} \mathrm{e}^{i2wD}}, \tag{2.35}$$

where p/s can be either p or s depending on the polarization component in question, Eqs. (2.33 and 2.34) can be written in a more concise form as

$$\begin{aligned}\mathbf{E}_{\text{out}}(0) &= \hat{\mathbf{p}}_{+}t^{p}_{21}\left(C^{p}E^{p}_{+}(0)+r^{p}_{23}\mathrm{e}^{iwD}C^{p}E^{p}_{-}(-D)\right) \\ &\quad+\hat{\mathbf{s}}t^{s}_{21}\left(C^{s}E^{s}_{+}(0)+r^{s}_{23}\mathrm{e}^{iwD}C^{s}E^{s}_{-}(-D)\right)\end{aligned} \tag{2.36}$$

$$\begin{aligned}\mathbf{E}_{\text{out}}(-D) &= \hat{\mathbf{p}}_{-}t^{p}_{23}\left(C^{p}E^{p}_{-}(-D)+r^{p}_{21}\mathrm{e}^{iwD}C^{p}E^{p}_{+}(0)\right) \\ &\quad+\hat{\mathbf{s}}t^{s}_{23}\left(C^{s}E^{s}_{-}(-D)+r^{s}_{21}\mathrm{e}^{iwD}C^{s}E^{s}_{+}(0)\right),\end{aligned} \tag{2.37}$$

where the parameters C^p and C^s describe the Fabry-Perot factors arising from successive reflections for p and s polarized fields, respectively.

3. NONLINEAR OPTICS AND SOURCE POLARIZATION

In this chapter, we lay out the basic principles of nonlinear optics and second-harmonic generation (SHG). Our goal is to formulate expressions for the nonlinear source polarization present in the previous chapter with respect to the fundamental optical field and for the generated harmonic field in various relevant configurations.

The field of nonlinear optics addresses the nonlinear part of the material response to an optical field. Mathematically speaking, the material polarization can be expressed in terms of its dependence on different powers of the electric field under ED approximation as [6, 18]

$$\mathbf{P}(\mathbf{r},t) = \epsilon_0 \sum_{j=1}^{\infty} \boldsymbol{\chi}^{(j)}(\mathbf{r},t) \cdot \mathbf{E}^j(\mathbf{r},t), \tag{3.1}$$

where the interaction is assumed to be local and instantaneous. In Eq. (3.1), $\boldsymbol{\chi}^{(j)}$ denotes the j:th order susceptibility tensor governing the response to the j:th power of the electric field. If the medium is assumed to be isotropic in the linear regime, the first order susceptibility can be described with a scalar and the polarization can be expanded to its linear and nonlinear parts as described by Eq. (2.17). As a result, the nonlinear part can be written as

$$\mathbf{P}^{\mathrm{NL}}(\mathbf{r},t) = \epsilon_0 \sum_{j=2}^{\infty} \boldsymbol{\chi}^{(j)}(\mathbf{r},t) \cdot \mathbf{E}^j(\mathbf{r},t). \tag{3.2}$$

Using this notation, the nonlinear part of the polarization acts as the source polarization equivalent to the source polarization discussed in the previous chapter, while the linear part is contained within the refractive index.

The process of interest in this work, the SHG, is an instantaneous second-order process described by the first term in the summation in Eq. (3.2) [6]. Thus, the

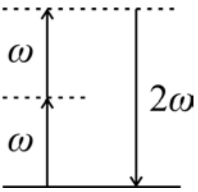

Figure 3.1: A photon diagram of the second-harmonic generation process.

higher order terms can be neglected, yielding a nonlinear polarization of

$$\mathbf{P}^{\mathrm{NL}}(\mathbf{r},t) = \epsilon_0 \boldsymbol{\chi}^{(2)}(\mathbf{r},t) \cdot \mathbf{E}^2(\mathbf{r},t). \tag{3.3}$$

It is again useful to treat the time-dependent quantities in terms of their frequency components. Specifically, by describing the incident field with its frequency components $\mathbf{E}(t) = \mathbf{E}(\omega)\mathrm{e}^{-i\omega t} + \mathrm{c.c.}$, the squared field in Eq. (3.3) becomes

$$\mathbf{E}^2(t) = \mathbf{E}(\omega)\mathbf{E}(\omega)\mathrm{e}^{-2i\omega t} + \mathbf{E}(\omega)\mathbf{E}^*(\omega) + \mathrm{c.c.}, \tag{3.4}$$

and has two frequency components 2ω and 0. Assuming that the response is instantaneous, these two frequency components of the fundamental field give rise to two frequency components for the material polarization at 2ω and 0, respectively. The 0 component corresponds to optical rectification, a temporally static electric field that is of no interest to us. The 2ω component, however, corresponds to the SHG process shown in (Fig. 3.1). Thus, the SHG source polarization can be written as

$$\mathbf{P}^{\mathrm{NL}}(\mathbf{r},2\omega) = \epsilon_0 \boldsymbol{\chi}^{(2)}(\mathbf{r},2\omega;\omega,\omega) \cdot \mathbf{E}^2(\mathbf{r},\omega), \tag{3.5}$$

with, neglecting optical rectification,

$$\mathbf{P}^{\mathrm{NL}}(\mathbf{r},t) = \mathbf{P}^{\mathrm{NL}}(\mathbf{r},2\omega)\mathrm{e}^{-2i\omega t} + \mathrm{c.c.}. \tag{3.6}$$

Lastly, if the nonlinear medium is homogeneous in terms of the nonlinear susceptibility, and the incident field is a plane wave characterized by k_x, we can write the SHG polarization as

$$\mathbf{P}^{\mathrm{NL}}(2k_x,z;2\omega) = \epsilon_0 \boldsymbol{\chi}^{(2)}(2\omega;\omega,\omega) \cdot \mathbf{E}^2(k_x,z;\omega), \tag{3.7}$$

where

$$\mathbf{P}^{\mathrm{NL}}(\mathbf{r}, 2\omega) = \epsilon_0 \mathbf{P}^{\mathrm{NL}}(2k_x, z; 2\omega)\mathrm{e}^{2ik_x x} + \mathrm{c.c.}, \tag{3.8}$$

whose form is compatible with the analysis presented in Chapter 2. To avoid clutter, the spatial frequency k_x will be left implicit from now on in the description of the SHG polarization arising from a plane wave characterized by k_x.

3.1 SHG susceptibility

SHG susceptibility is the fundamental material quantity governing the SHG process. In this section, we examine the mathematical properties of the SHG susceptibility under ED approximation. Mathematically, the SHG susceptibility can be described as a third rank polar tensor. The tensorial relation of Eq. (3.7) can be written in terms of spatial components as

$$P_i^{\mathrm{NL}}(\mathbf{r}, 2\omega) = \epsilon_0 \sum_{(j,k)} \chi_{ijk}^{(2)}(\mathbf{r}, 2\omega; \omega, \omega) E_j(\mathbf{r}, \omega) E_k(\mathbf{r}, \omega), \tag{3.9}$$

where the subscript i denotes the vector component of the SHG polarization, the subscripts j and k denote the vector components of the interacting field, $\chi_{ijk}^{(2)}$ is the tensor component describing the i:th SHG polarization vector component generated by fundamental field components j and k and the summation is carried out over material coordinate axes.

As a third rank polar tensor, the SHG susceptibility is sensitive to symmetry. Firstly, due to the fact that the two fundamental field factors in Eq. (3.9) are identical and thus interchangeable, it is immediately evident that the permutation of the last two indices cannot change the process in any way, i.e.,

$$\chi_{ijk}^{(2)}(2\omega; \omega, \omega) = \chi_{ikj}^{(2)}(2\omega; \omega, \omega). \tag{3.10}$$

This property is known as the intrinsic permutation symmetry and, as stated above, always holds for SHG [6].

Secondly, it can be shown that as long as all frequencies of the interaction (ω and 2ω) are sufficiently far from material resonances, all of the indices of the SHG tensor can be permuted as long as the corresponding frequency arguments are permuted as well, i.e.,

$$\chi_{ijk}^{(2)}(2\omega; \omega, \omega) = \chi_{jik}^{(2)}(\omega; 2\omega, -\omega), \tag{3.11}$$

where the signs of the frequency arguments must be chosen so that the first one is the sum of the latter two. This is called the full permutation symmetry. Furthermore, if the frequencies are much smaller than the lowest resonance frequency of the material, the susceptibility depends weakly on frequency [6]. As a result, all of the indices of the susceptibility tensor can be permuted freely

$$\chi^{(2)}_{ijk} = \chi^{(2)}_{jik} = \chi^{(2)}_{kji} = \chi^{(2)}_{ikj} = \chi^{(2)}_{jki} = \chi^{(2)}_{kij}, \tag{3.12}$$

where the frequency arguments are omitted as irrelevant. This is called the Kleinman symmetry [79], and while we do not assume it to hold in this work, it is worth noting in order to analyze the results.

Lastly, there are certain restrictions for the susceptibility components that arise from the symmetry of the material system. For a structural symmetry operation $\mathbf{r} \to \mathbf{r}'$, the new susceptibility tensor must remain constant, i.e., $\chi'^{(2)} = \chi^{(2)}$. The new susceptibility tensor component $\chi'^{(2)}$ resulting from a transformation $\mathbf{r} \to \mathbf{r}'$ for a third-rank polar tensor is given by [19]

$$\chi^{(2)}_{ijk} \to \chi'^{(2)}_{ijk} = \sum_{(m,n,\sigma)} \frac{\partial r'_i}{\partial m} \frac{\partial r'_j}{\partial n} \frac{\partial r'_k}{\partial \sigma} \chi^{(2)}_{mn\sigma} = \chi^{(2)}_{ijk}, \tag{3.13}$$

where (r'_i, r'_j, r'_k) are the coordinates corresponding to the indices of the post-transform tensor $\chi'^{(2)}_{ijk}$ and the summation of (m, n, σ) is carried over pre-transform coordinates. The last equality follows from the fact that the transformation is a symmetry operation.

The structural symmetry poses some very important restrictions for SHG, such as the well known property that SHG is forbidden in a centrosymmetric medium under ED approximation. The layered structures studied in this work are assumed to exhibit in-plane isotropy, i.e., to belong to the symmetry group $C_{\infty v}$. Using Eqs. (3.10 and 3.13), the nonvanishing independent SHG tensor components for such a material under ED approximation can be shown to be [18]

$$\chi^{(2)}_{zzz},\ \chi^{(2)}_{zxx} = \chi^{(2)}_{zyy},\ \chi^{(2)}_{xzx} = \chi^{(2)}_{yzy} = \chi^{(2)}_{xxz} = \chi^{(2)}_{yyz}. \tag{3.14}$$

Note that in the above equation as well as the following analysis the frequency arguments are omitted for simplicity.

The above analysis was carried out within the ED approximation, i.e., within an assumption where the source is governed by the electric polarization arising from fundamental electric field as described by Eqs. (2.17 and 3.2). Although the ED interaction is often the strongest electromagnetic phenomenon, magnetic and higher multipole interactions behave differently under symmetry and can thus have an unique contribution to the SHG process.

In the following, we will consider magnetic-dipole and electric-quadrupole contributions to SHG so that only one photon of the process can be interacting via magnetic or quadrupole interaction at a time. This is justified by the fact that in this work we are mainly interested in qualitative detection of multipole phenomena and by the general weakness of higher multipole interactions compared to the ED interaction for most materials [80]. For the same reason, we will neglect higher-multipole contributions beyond magnetic-dipole and electric-quadrupole (e.g., magnetic-quadrupole, electric-octopole, etc.). From here on, we will use the term multipole (MP) to refer to electric-quadrupole and magnetic-dipole interactions.

The MP interactions can be addressed by including MP terms into the constitutive equations Eqs. (2.2) and rewriting them as [76]

$$\mathbf{D}(\mathbf{r},t) = \epsilon_0 n^2 \mathbf{E}(\mathbf{r},t) + \mathbf{P}(\mathbf{r},t) - \nabla \cdot \mathbf{Q}(\mathbf{r},t) \tag{3.15}$$

$$\mathbf{H}(\mathbf{r},t) = \frac{1}{\mu_0}\mathbf{B}(\mathbf{r},t) - \mathbf{M}(\mathbf{r},t), \tag{3.16}$$

where $\mathbf{P}$, $\mathbf{M}$ and $\mathbf{Q}$ are the nonlinear parts of material polarization, magnetization and quadrupolarization, respectively and which results in a set of equations similar to Eqs. (2.18), but with the source polarization term given by [76]

$$\mathbf{P}^{\mathrm{NL}} = \mathbf{P}^{\mathrm{ED}} + \mathbf{P}^{\mathrm{MP}} + \frac{i}{\omega}\nabla \times \mathbf{M} - \nabla \cdot \mathbf{Q} = \mathbf{P}^{\mathrm{ED}} + \mathbf{P}^{\mathrm{MP,eff}}, \tag{3.17}$$

where $\mathbf{P}^{\mathrm{NL}}$ is the total effective nonlinear polarization, $\mathbf{P}^{\mathrm{ED}}$ is the conventional nonlinear ED polarization, $\mathbf{P}^{\mathrm{MP}}$ is the nonlinear electric dipole density arising from MP interaction and $\mathbf{P}^{\mathrm{MP,eff}}$ is the sum of all MP terms.

Using a similar approach to what was presented in Ref. [70, 81, 82], the multipolar

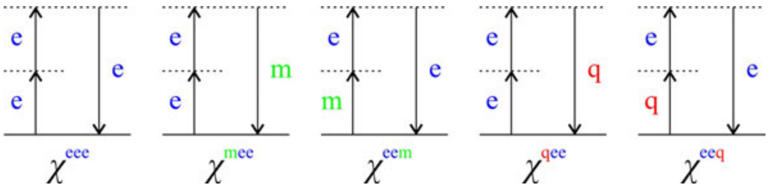

Figure 3.2: A schematic of the electric-dipole (e), magnetic-dipole (m) and electric-quadrupole (q) interactions addressed in this work.

source terms to the SHG can be written as

$$P_i^{\mathrm{MP}}(2\omega) = \chi_{ijk}^{eem} E_j(\omega) B_k(\omega) + \chi_{ijkl}^{eeq} E_j(\omega) \nabla_k E_l(\omega) \tag{3.18}$$

$$M_i = \chi_{ijk}^{mee} E_j(\omega) E_k(\omega) \tag{3.19}$$

$$Q_{ij} = \chi_{ijkl}^{qee} E_k(\omega) E_l(\omega), \tag{3.20}$$

where, for clarity, the superscript (2) was replaced with superscripts referring to the physical origin of interaction associated with the dimensions of the tensor. The first superscript corresponds to the interaction between the SHG photon and the material, and the latter two correspond to the interactions between the fundamental photons and the material. The values of the superscripts are either e, m, or q for ED, magnetic dipole and quadrupole interactions, respectively. The notation is shown in (Fig. 3.2).

The introduced MP interactions have different behavior under symmetry than the ED interaction. The magnetic SHG susceptibilities (χ_{ijk}^{mee}, χ_{ijk}^{eem}) are third rank tensors with one axial dimension and the quadrupolar SHG susceptibilities (χ_{ijkl}^{qee}, χ_{ijkl}^{eeq}) are fourth rank polar tensors, whereas the ED SHG susceptibility is a third rank polar tensor. The symmetry properties can still be determined by using a method similar to what was used for ED case. For the magnetic susceptibility, Eq. (3.13) is valid provided that the sign is switched for each *improper* symmetry operation [19]. For the quadrupolar susceptibility, the summation in Eq. (3.13) must be adjusted to be carried over all four indices with four corresponding derivatives in the summand [19] as

$$\chi_{ijkl}^{(2)} \rightarrow \chi_{ijkl}^{\prime(2)} = \sum_{(m,n,\sigma,\rho)} \frac{\partial r_i'}{\partial m} \frac{\partial r_j'}{\partial n} \frac{\partial r_k'}{\partial \sigma} \frac{\partial r_l'}{\partial \rho} \chi_{mn\sigma\rho}^{(2)} = \chi_{ijkl}^{(2)}, \tag{3.21}$$

where the notation is similar to that of Eq. (3.13).

Regarding the MP interaction, we will limit ourselves to the case of full isotropy. This is justified in the scope of this work since we are interested in qualitative probing of the presence of multipole effects in thin films. Under full isotropy, the independent nonvanishing components of a third rank tensor with a single axial component (magnetic susceptibility) and a fourth rank polar tensor (quadrupolar susceptibility) can be written as [6, 18]

$$\chi_{xyz} = \chi_{yzx} = \chi_{zxy} = -\chi_{xzy} = -\chi_{zyx} = -\chi_{yxz}, \text{ and} \tag{3.22}$$

$$\chi_{ijkl} = \chi_{xxyy}\delta_{ij}\delta_{kl} + \chi_{xyxy}\delta_{ik}\delta_{jl} + \chi_{xyyx}\delta_{il}\delta_{jk}, \tag{3.23}$$

where δ is the Kronecker delta, respectively. These nonvanishing components can further be combined into three components in a well documented fashion as [59, 63, 70, 81]

$$\mathbf{P}^{\mathrm{MP,eff}} = \beta\mathbf{E}(\omega)(\nabla \cdot \mathbf{E}(\omega)) + \gamma\nabla(\mathbf{E}(\omega) \cdot \mathbf{E}(\omega)) + \delta'(\mathbf{E}(\omega) \cdot \nabla)\mathbf{E}(\omega), \tag{3.24}$$

where the contribution from β is known to vanish for isotropic media and can thus be neglected. Furthermore, γ is known to be indistinguishable from surface ED SHG [59] and will be neglected here because in the scope of this work we are mainly interested in the detection of the presence of MP SHG governed by the last term.

3.2 Electric-dipole SHG from layered structures

In this section we will develop the mathematical formulae for the SHG generated from a thin nonlinear layer embedded between dielectric media under ED approximation. We will start by writing the full fundamental field within the thin layer, followed by expressing the source polarization introduced in Chapter 2, and finally calculating the total field leaving the material system.

Let us first consider the fundamental field within the nonlinear layer. For practical reasons, we consider a monochromatic plane wave of frequency ω characterized by spatial frequency k_x approaching the nonlinear layer from medium 1 as per the coordinate notation of Chapter 2. If the polarization components of the field prior to the upper interface are E_0^p and E_0^s, the polarization components of the field inside the nonlinear medium, neglecting reflections, are given by

$$E_-^{p/s}(z) = t_{12}^{p/s} E_0^{p/s} \mathrm{e}^{iw_- z}, \tag{3.25}$$

where the p/s once more denotes either p or s depending on the polarization component in question.

For the reasons outlined in Chapter 2, reflections at the interfaces of the nonlinear layer give rise to both upward and downward propagating waves. Using Eqs. (2.30 and 2.31) and setting $\mathbf{E}_+ = 0$, the total fundamental field inside the medium can be written as

$$\begin{aligned} \mathbf{E}_\mathrm{T}(z) &= \mathbf{E}_{\mathrm{T}+}\mathrm{e}^{iw_+z} + \mathbf{E}_{\mathrm{T}-}\mathrm{e}^{iw_-z} \\ &= \left(\hat{\mathbf{p}}_+ E^p_{\mathrm{T}+} + \hat{\mathbf{s}} E^s_{\mathrm{T}+}\right)\mathrm{e}^{iw_+z} + \left(\hat{\mathbf{p}}_- E^p_{\mathrm{T}-} + \hat{\mathbf{s}} E^s_{\mathrm{T}-}\right)\mathrm{e}^{iw_-z}, \end{aligned} \tag{3.26}$$

with

$$E^{p/s}_{\mathrm{T}+} = K^{p/s}_{\mathrm{T}+} E^{p/s}_0 = \mathrm{e}^{2iwD} t^{p/s}_{12} r^{p/s}_{23} C^{p/s} E^{p/s}_0 \text{ and} \tag{3.27}$$

$$E^{p/s}_{\mathrm{T}-} = K^{p/s}_{\mathrm{T}-} E^{p/s}_0 = t^{p/s}_{12} C^{p/s} E^{p/s}_0, \tag{3.28}$$

where $C^{p/s}$ is the parameter defined in Eq. (2.35) and $K^{p/s}_\pm$ factors are used to combine the reflection effects discussed in the last section of Chapter 2 in a convenient manner. Now, the SHG polarization arising from the fundamental field can be written as

$$\mathbf{P}(z) = \epsilon_0 \boldsymbol{\chi}^{(2)} \cdot \mathbf{E}^2_\mathrm{T}(z), \tag{3.29}$$

with

$$\mathbf{E}^2_\mathrm{T}(z) = (\mathbf{E}_{\mathrm{T}+})^2\mathrm{e}^{2iw_+z} + \mathbf{E}_{\mathrm{T}+}\mathbf{E}_{\mathrm{T}-} + \mathbf{E}_{\mathrm{T}-}\mathbf{E}_{\mathrm{T}+} + (\mathbf{E}_{\mathrm{T}-})^2\mathrm{e}^{2iw_-z}. \tag{3.30}$$

The above equations fully describe the SHG source polarization that is compatible with the analysis of Chapter 2. The generated unreflected second-harmonic wave must fulfill Eqs. (2.18), and can be described with Eqs. (2.32) with Eq. (3.29) as the source. However, before substitution, we note that the parameters of the second-harmonic solution must be evaluated for the second-harmonic frequency. Thus, we denote all frequency dependent quantities that correspond to the second-harmonic frequency with an underline, e.g., $\mathbf{E}(2\omega) \rightarrow \underline{\mathbf{E}}$. Now, the substitution for the upward and downward propagating SHG fields yields

$$\begin{aligned}\underline{\mathbf{E}}(0) = \epsilon_0 \mathrm{e}^{i\underline{k}_x x}\Big(&\int_{-D}^{0} \underline{\mathbf{G}}(0-z_0)\mathrm{e}^{2iw_- z_0} dz_0 \cdot \boldsymbol{\chi}^{(2)} \cdot (\mathbf{E}_{\mathrm{T}-})^2 \\ &+ \int_{-D}^{0} \underline{\mathbf{G}}(0-z_0) dz_0 \cdot \boldsymbol{\chi}^{(2)} \cdot \mathbf{E}_{\mathrm{T}+}\mathbf{E}_{\mathrm{T}-} \\ &+ \int_{-D}^{0} \underline{\mathbf{G}}(0-z_0) dz_0 \cdot \boldsymbol{\chi}^{(2)} \cdot \mathbf{E}_{\mathrm{T}-}\mathbf{E}_{\mathrm{T}+} \\ &+ \int_{-D}^{0} \underline{\mathbf{G}}(0-z_0)\mathrm{e}^{2iw_+ z_0} dz_0 \cdot \boldsymbol{\chi}^{(2)} \cdot (\mathbf{E}_{\mathrm{T}+})^2\Big) \text{ and}\end{aligned} \tag{3.31}$$

$$\begin{aligned}\underline{\mathbf{E}}(-D) = \epsilon_0 \mathrm{e}^{i\underline{k}_x x}\Big(&\int_{-D}^{0} \underline{\mathbf{G}}(-D-z_0)\mathrm{e}^{2iw_- z_0} dz_0 \cdot \boldsymbol{\chi}^{(2)} \cdot (\mathbf{E}_{\mathrm{T}-})^2 \\ &+ \int_{-D}^{0} \underline{\mathbf{G}}(-D-z_0) dz_0 \cdot \boldsymbol{\chi}^{(2)} \cdot \mathbf{E}_{\mathrm{T}+}\mathbf{E}_{\mathrm{T}-} \\ &+ \int_{-D}^{0} \underline{\mathbf{G}}(-D-z_0) dz_0 \cdot \boldsymbol{\chi}^{(2)} \cdot \mathbf{E}_{\mathrm{T}-}\mathbf{E}_{\mathrm{T}+} \\ &+ \int_{-D}^{0} \underline{\mathbf{G}}(-D-z_0)\mathrm{e}^{2iw_+ z_0} dz_0 \cdot \boldsymbol{\chi}^{(2)} \cdot (\mathbf{E}_{\mathrm{T}+})^2\Big),\end{aligned} \tag{3.32}$$

respectively, where $\underline{k}_x = 2k_x$ is the x-component of the wave vector of the generated SHG field and $\underline{\mathbf{G}}$ is the dyadic Green's function evaluated for the second-harmonic frequency. Thus, the SHG source polarization acts as a source to two plane waves characterized by wave vectors $\underline{\mathbf{k}}_\pm = \underline{k}_x\hat{x} + \underline{w}_\pm\hat{z}$ as per Eq. (2.12). In the following discussion, the transverse component of the wave vector will be left implicit as it is conserved in the system in the absence of nonlinear effects.

The integration in Eqs. (3.31 and 3.32) can be carried out by the substitution of Eq. (2.27), yielding

$$\begin{aligned}\underline{\mathbf{E}}(0) = \frac{\underline{\omega}^2}{2c^2\underline{w}}(\hat{\underline{\mathbf{p}}}_+\hat{\underline{\mathbf{p}}}_+ + \hat{\underline{\mathbf{s}}}\hat{\underline{\mathbf{s}}}) \cdot \Big(&\boldsymbol{\chi}^{(2)} \cdot (\mathbf{E}_{\mathrm{T}+})^2\Phi_{+++} \\ &+ \boldsymbol{\chi}^{(2)} \cdot \mathbf{E}_{\mathrm{T}+}\mathbf{E}_{\mathrm{T}-}\Phi_{++-} + \boldsymbol{\chi}^{(2)} \cdot \mathbf{E}_{\mathrm{T}-}\mathbf{E}_{\mathrm{T}+}\Phi_{+-+} \\ &+ \boldsymbol{\chi}^{(2)} \cdot (\mathbf{E}_{\mathrm{T}-})^2\Phi_{+--}\Big)\end{aligned} \tag{3.33}$$

$$\begin{aligned}\underline{\mathbf{E}}(-D) = \frac{\underline{\omega}^2}{2c^2\underline{w}}\mathrm{e}^{i\underline{w}D}(\hat{\underline{\mathbf{p}}}_-\hat{\underline{\mathbf{p}}}_- + \hat{\underline{\mathbf{s}}}\hat{\underline{\mathbf{s}}}) \cdot \Big(&\boldsymbol{\chi}^{(2)} \cdot (\mathbf{E}_{\mathrm{T}+})^2\Phi_{-++} \\ &+ \boldsymbol{\chi}^{(2)} \cdot \mathbf{E}_{\mathrm{T}+}\mathbf{E}_{\mathrm{T}-}\Phi_{-+-} + \boldsymbol{\chi}^{(2)} \cdot \mathbf{E}_{\mathrm{T}-}\mathbf{E}_{\mathrm{T}+}\Phi_{--+} \\ &+ \boldsymbol{\chi}^{(2)} \cdot (\mathbf{E}_{\mathrm{T}-})^2\Phi_{---}\Big),\end{aligned} \tag{3.34}$$

where

$$\Phi_{\phi\beta\gamma} = \frac{1 - \mathrm{e}^{-i(-\underline{w}_\phi + w_\beta + w_\gamma)D}}{-\underline{w}_\phi + w_\beta + w_\gamma}, \tag{3.35}$$

and $\phi, \beta, \gamma \in \{+, -\}$. The upward and downward generated fields described by Eqs. (3.33 and 3.34) both contribute to the total SHG fields leaving the medium as per Eqs. (2.36 and 2.37). Let us consider the SHG field leaving to medium 3 and substitute Eqs. (3.33 and 3.34) into Eq. (2.37), yielding

$$\begin{aligned}\underline{E}^p_{\mathrm{out}}(-D) = \mathrm{e}^{i\underline{w}D}\frac{\underline{\omega}^2}{2c^2\underline{w}}\underline{t}^p_{23}\sum_{\phi\beta\gamma}\underline{\hat{\mathbf{p}}}_\phi \cdot \boldsymbol{\chi}^{(2)}\underline{K}^p_\phi\Phi_{\phi\beta\gamma}\cdot\Big(&\hat{\mathbf{p}}_\beta\hat{\mathbf{p}}_\gamma K^p_\beta K^p_\gamma (E^p_0)^2 \\ &+ \hat{\mathbf{p}}_\beta\hat{\mathbf{s}}K^p_\beta K^s_\gamma E^p_0 E^s_0 + \hat{\mathbf{s}}\hat{\mathbf{p}}_\gamma K^s_\beta K^p_\gamma E^s_0 E^p_0 + \hat{\mathbf{s}}\hat{\mathbf{s}}K^s_\beta K^s_\gamma (E^s_0)^2\Big)\end{aligned} \tag{3.36}$$

$$\begin{aligned}\underline{E}^s_{\mathrm{out}}(-D) = \mathrm{e}^{i\underline{w}D}\frac{\underline{\omega}^2}{2c^2\underline{w}}\underline{t}^s_{23}\sum_{\phi\beta\gamma}\underline{\hat{\mathbf{s}}} \cdot \boldsymbol{\chi}^{(2)}\underline{K}^s_\phi\Phi_{\phi\beta\gamma}\cdot\Big(&\hat{\mathbf{p}}_\beta\hat{\mathbf{p}}_\gamma K^p_\beta K^p_\gamma (E^p_0)^2 \\ &+ \hat{\mathbf{p}}_\beta\hat{\mathbf{s}}K^p_\beta K^s_\gamma E^p_0 E^s_0 + \hat{\mathbf{s}}\hat{\mathbf{p}}_\gamma K^s_\beta K^p_\gamma E^s_0 E^p_0 + \hat{\mathbf{s}}\hat{\mathbf{s}}K^s_\beta K^s_\gamma (E^s_0)^2\Big),\end{aligned} \tag{3.37}$$

where $\underline{K}^{p/s}_+ = r^{p/s}_{21}\underline{C}^{p/s}$, $\underline{K}^{p/s}_- = \underline{C}^{p/s}$ and the summation is carried out over all combinations of $\phi, \beta, \gamma \in \{+, -\}$.

Although tedious, the forms of Eqs. (3.36 and 3.37) become convenient as they explicitly map the SHG field polarization components with respect to those of the fundamental field. To probe the SHG susceptibility tensor, a polarization controlled experiment can be utilized. It is thus useful to describe the SHG process in the system in terms of polarization signatures, i.e.,

$$\underline{E}^p_{\mathrm{out}}(-D) = f^{ppp}(E^p_0)^2 + f^{pps}E^p_0E^s_0 + f^{psp}E^s_0E^p_0 + f^{pss}(E^s_0)^2 \tag{3.38}$$

$$\underline{E}^s_{\mathrm{out}}(-D) = f^{spp}(E^p_0)^2 + f^{sps}E^p_0E^s_0 + f^{ssp}E^s_0E^p_0 + f^{sss}(E^s_0)^2, \tag{3.39}$$

where $f^{\zeta,\eta,\kappa}$ are the polarization signatures for ζ-polarized SHG arising from η and κ -polarization components of the fundamental field, i.e., $\zeta, \eta, \kappa \in \{p, s\}$. The polarization signatures can be written as

$$f^{\zeta,\eta,\kappa} = \mathrm{e}^{i\underline{w}D}\frac{\underline{\omega}^2}{2c^2\underline{w}}\underline{t}^\zeta_{23}\sum_{\phi\beta\gamma}\underline{\hat{\boldsymbol{\zeta}}}_\phi \cdot \boldsymbol{\chi}^{(2)}\Phi_{\phi\beta\gamma}\cdot\hat{\boldsymbol{\eta}}_\beta\hat{\boldsymbol{\kappa}}_\gamma\underline{K}^\zeta_\phi K^\eta_\beta K^\kappa_\gamma. \tag{3.40}$$

Finally, the polarization signatures can be described in terms of SHG susceptibility tensor components by expressing the tensor product in terms of the polarization unit basis vectors $(\hat{p}_{\pm}, \hat{s}, \hat{k}_{\pm})$ shown in (Fig. 2.2) as

$$f^{\zeta,\eta,\kappa} = \mathrm{e}^{i\underline{w}D} \frac{\underline{\omega}^2}{2c^2\underline{w}} \underline{t}_{23}^{\zeta} \sum_{ijk} \sum_{\phi\beta\gamma} \underline{L}_{\zeta,i,\phi} \chi_{ijk}^{(2)} \Phi_{\phi\beta\gamma} L_{\eta,j,\beta} L_{\kappa,k,\gamma} \underline{K}_{\phi}^{\zeta} K_{\beta}^{\eta} K_{\gamma}^{\kappa}, \tag{3.41}$$

where the summation of i, j, k is carried out over Cartesian coordinates. For a fundamental field propagating along c-direction, the factor L_{abc} is the projection of the polarization component a to the Cartesian axis b. Similarly, for a SHG field propagating along c-direction, the factor $\underline{L}_{abc}$ is the projection of the Cartesian coordinate b to the polarization component a. As such, for a given system with a thin source embedded between two dielectric media and a given angle of incidence of the fundamental field, the polarization signatures are linear combinations of the SHG susceptibility tensor components.

In should be noted that although Eq. (3.41) may seem mathematically convoluted, the various factors present describe distinct physical phenomena: $\underline{K}$ and the two K-factors describe the mixing of the upward and downward propagating partial fields inside the thin medium for SHG and fundamental fields, respectively; $\underline{L}$ and the two L factors describe the projections between the field polarization coordinates and the system coordinates for SHG and fundamental fields, respectively; and the factor Φ describes the phase-mismatch of the SHG process for different combinations of upward and downward propagating partial fundamental and SHG fields. Finally, within $\underline{K}$ and K, the $\underline{C}$ and the two C factors are the etalon factors due to multiple reflections inside the thin layer for the SHG and fundamental fields, respectively. A short summary about the above parameters is shown in Table 3.1.

Table 3.1: A short summary of the used parameters

Factor	Description
C	Etalon factor due to consequtive reflections
K	Combined etalon factor and cross contribution between + and −
L	Projection between beam coordinates and material coordinates
Φ	Phase mismatch factor between SHG polarization and SHG field

The concept of polarization signatures conveniently splits the analysis into two parts: 1) The relationship between the signatures and the SHG susceptibility, which depends on the material symmetry and system geometry; 2) The polarization signatures that can be uniquely determined by the degrees of freedom available with the experiment. This is very useful for the planning of experimental methodology for a sample of given symmetry as well as interpretation of unexpected results.

3.3 Multipolar SHG from layered structures

In this section, we will address MP SHG from a thin nonlinear layer embedded between dielectric media. A common method for the study of MP SHG from isotropic materials involves utilizing two non-collinear excitation beams, and studying the SHG process where one of the fundamental photons originate from each of the beams [64, 83]. Using this method, it is possible to separate the MP bulk contribution from the ED surface contribution to SHG [67, 84–86]. In the following, we will derive the expressions for the ED and MP SHG arising jointly from two non-collinear beams. As before, we will consider an in-plane isotropic nonlinear material for the ED SHG process. However, for simplicity, we assume the material to be fully isotropic for the MP SHG case and that the MP SHG arises primarily from the δ' term in Eq. (3.24). This is justified by the fact that, within the context of this work, it is sufficient to study the signatures of the presence of MP SHG rather than fully characterize the complete MP response. In addition, the other contributions are not strictly of bulk origin.

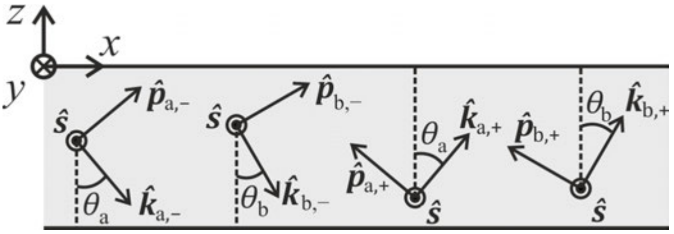

Figure 3.3: A schematic of the relationship between the beam coordinates and material system coordinates for two-beam configuration.

We begin by considering two non-collinear plane waves, denoted by a and b, at the same frequency but different angles of propagation. The beams approach the nonlinear layer from medium 1 so that their wave vectors are in the same the plane of incidence. The only differences between the beams are the quantities that depend on the angle of propagation. These quantities include the angle of propagation, the components of the wave vector, the polarization coordinate system and the Fresnel coefficients. In order to account for this, a subscript a or b is added to all these quantities (see Fig. 3.3). Aside from that, both beams can be treated with the previous analysis for plane waves in layered structures. Using this approach, the individual fields inside the nonlinear layer $\mathbf{E}_{\mathrm{T},a/b}(\mathbf{r})$ can be written in terms of their polarization component amplitudes right before the upper interface $E^{p/s}_{a/b,0}$ as

$$\begin{aligned}\mathbf{E}_{\mathrm{T},a/b}(\mathbf{r}) &= (\mathbf{E}_{\mathrm{T},a/b,+}\mathrm{e}^{iw_{a/b,+}z} + \mathbf{E}_{\mathrm{T},a/b,-}\mathrm{e}^{iw_{a/b,-}z})\mathrm{e}^{ik_{a/b,x}x} \\ &= \Big[\Big(\hat{\mathbf{p}}_{a/b,+}E^{p}_{\mathrm{T},a/b,+} + \hat{\mathbf{s}}E^{s}_{\mathrm{T},a/b,+}\Big)\,\mathrm{e}^{iw_{a/b,+}z} \\ &\quad + \Big(\hat{\mathbf{p}}_{a/b,-}E^{p}_{\mathrm{T},a/b,-} + \hat{\mathbf{s}}E^{s}_{\mathrm{T},a/b,-}\Big)\,\mathrm{e}^{iw_{a/b,-}z}\Big]\mathrm{e}^{ik_{a/b,x}x},\end{aligned} \tag{3.42}$$

with

$$E^{p/s}_{\mathrm{T},a/b,+} = K^{p/s}_{a/b,+}E^{p/s}_{a/b,0} = \mathrm{e}^{2iw_{a/b}D}t^{p/s}_{a/b,12}r^{p/s}_{a/b,23}C^{p/s}_{a/b}E^{p/s}_{a/b,0} \text{ and} \tag{3.43}$$

$$E^{p/s}_{\mathrm{T},a/b,-} = K^{p/s}_{a/b,-}E^{p/s}_{a/b,0} = t^{p/s}_{a/b,12}C^{p/s}_{a/b}E^{p/s}_{a/b,0}. \tag{3.44}$$

for beam a/b. The above equations fully describe the electric fields of the two beams inside the nonlinear layer.

Let us first consider the ED SHG by following an approach almost identical to the single beam case. The total electric field inside the medium is given by $\mathbf{E} = \mathbf{E}_a + \mathbf{E}_b$ and the ED source polarization depends on the square of the total electric field $\mathbf{P} = \epsilon_0\boldsymbol{\chi}^{(2)}\mathbf{E}^2$. By using Eq. (3.42), the ED source polarization can be seen to consist of three terms with different transverse spatial behavior: $2k_{a,x}$, $2k_{b,x}$ and $k_{a,x} + k_{b,x}$. Only the last term corresponds to the case where a photon is annihilated from each of the beams which, as discussed in the beginning of this section, results in new information. Thus, the two former terms are neglected and the squared field can be written as

$$\mathbf{E}^2(\mathbf{r}) = \Big[\mathbf{E}_a(z)\mathbf{E}_b(z) + \mathbf{E}_b(z)\mathbf{E}_a(z)\Big]\mathrm{e}^{i(k_{a,x}+k_{b,x})x}. \tag{3.45}$$

The generated unreflected ED SHG field for the two-beam case can be determined by substituting the above equations to Eqs. (2.32), yielding

$$\begin{aligned}\underline{\mathbf{E}}_{\mathrm{ED}}(0) = \epsilon_0 \mathrm{e}^{i\underline{k}_x x}\Big(&\int_{-D}^{0} \underline{\mathbf{G}}(0-z_0)\mathrm{e}^{i(w_{a,+}+w_{b,+})z_0}dz_0 \cdot \boldsymbol{\chi}^{(2)} \cdot \mathbf{E}_{\mathrm{T},a,+}\mathbf{E}_{\mathrm{T},b,+}\\ &+\int_{-D}^{0} \underline{\mathbf{G}}(0-z_0)\mathrm{e}^{i(w_{a,+}+w_{b,-})z_0}dz_0 \cdot \boldsymbol{\chi}^{(2)} \cdot \mathbf{E}_{\mathrm{T},a,+}\mathbf{E}_{\mathrm{T},b,-}\\ &+\int_{-D}^{0} \underline{\mathbf{G}}(0-z_0)\mathrm{e}^{i(w_{a,-}+w_{b,+})z_0}dz_0 \cdot \boldsymbol{\chi}^{(2)} \cdot \mathbf{E}_{\mathrm{T},a,-}\mathbf{E}_{\mathrm{T},b,+}\\ &+\int_{-D}^{0} \underline{\mathbf{G}}(0-z_0)\mathrm{e}^{i(w_{a,-}+w_{b,-})z_0}dz_0 \cdot \boldsymbol{\chi}^{(2)} \cdot \mathbf{E}_{\mathrm{T},a,-}\mathbf{E}_{\mathrm{T},b,-}\Big) + [a \leftrightarrow b] \text{ and}\end{aligned} \tag{3.46}$$

$$\begin{aligned}\underline{\mathbf{E}}_{\mathrm{ED}}(-D) = \epsilon_0 \mathrm{e}^{i\underline{k}_x x}\Big(&\int_{-D}^{0} \underline{\mathbf{G}}(-D-z_0)\mathrm{e}^{i(w_{a,+}+w_{b,+})z_0}dz_0 \cdot \boldsymbol{\chi}^{(2)} \cdot \mathbf{E}_{a,+}\mathbf{E}_{b,+}\\ &+\int_{-D}^{0} \underline{\mathbf{G}}(-D-z_0)\mathrm{e}^{i(w_{a,+}+w_{b,-})z_0}dz_0 \cdot \boldsymbol{\chi}^{(2)} \cdot \mathbf{E}_{a,+}\mathbf{E}_{b,-}\\ &+\int_{-D}^{0} \underline{\mathbf{G}}(-D-z_0)\mathrm{e}^{i(w_{a,-}+w_{b,+})z_0}dz_0 \cdot \boldsymbol{\chi}^{(2)} \cdot \mathbf{E}_{a,-}\mathbf{E}_{b,+}\\ &+\int_{-D}^{0} \underline{\mathbf{G}}(-D-z_0)\mathrm{e}^{i(w_{a,-}+w_{b,-})z_0}dz_0 \cdot \boldsymbol{\chi}^{(2)} \cdot \mathbf{E}_{a,-}\mathbf{E}_{b,-}\Big) + [a \leftrightarrow b],\end{aligned} \tag{3.47}$$

where $\underline{k}_x = k_{a,x}+k_{b,x}$ and $[a \leftrightarrow b]$ denotes an additional term identical to the previous one but with a and b interchanged. By substituting Eq. (2.27) and carrying out the integration, the total s-polarized ED SHG field leaving the nonlinear layer can be written as

$$\begin{aligned}\underline{E}^{s}_{\mathrm{out,ED}}(-D) = \mathrm{e}^{i\underline{w}D}\frac{\underline{\omega}^2}{2c^2\underline{w}}\underline{t}^{s}_{23}\sum_{\phi\beta\gamma}\hat{\underline{\mathbf{s}}}\cdot\boldsymbol{\chi}^{(2)}\underline{K}^{s}_{\phi}\Phi'_{\phi,\beta\gamma}\cdot\Big(&\hat{\mathbf{p}}_{a,\beta}\hat{\mathbf{p}}_{b,\gamma}K^{p}_{a,\beta}K^{p}_{b,\gamma}E^{p}_{a,0}E^{p}_{b,0}\\ &+\hat{\mathbf{s}}\hat{\mathbf{p}}_{b,\gamma}K^{s}_{a,\beta}K^{p}_{b,\gamma}E^{s}_{a,0}E^{p}_{b,0}+\hat{\mathbf{p}}_{a,\beta}\hat{\mathbf{s}}K^{p}_{a,\beta}K^{s}_{b,\gamma}E^{p}_{a,0}E^{s}_{b,0}\\ &+\hat{\mathbf{s}}\hat{\mathbf{s}}K^{s}_{a,\beta}K^{s}_{b,\gamma}E^{s}_{a,0}E^{s}_{b,0}\Big)+[a \leftrightarrow b]\end{aligned} \tag{3.48}$$

where

$$\Phi'_{\phi,\beta,\gamma} = \frac{1-\mathrm{e}^{-i(-\underline{w}_{\phi}+w_{a,\beta}+w_{b,\gamma})D}}{-\underline{w}_{\phi}+w_{a,\beta}+w_{b,\gamma}}. \tag{3.49}$$

It is worth noting that the form of Eq. (3.48) is very similar to that of Eq. (3.37). In addition, the parameters that appear here are analogous to those defined for the single beam case and carry similar convenient physical insights within them.

Lastly, let us consider the MP SHG arising from the two fundamental beams. Once more, we will begin by examining the transverse profile of the source polarization by substituting the total field into the δ' term in Eq. (3.24), which yields [64]

$$\begin{aligned}(\mathbf{E}\cdot\nabla)\mathbf{E} = {}& i\mathrm{e}^{i2k_{a,x}x}(\mathbf{E}_a\cdot\mathbf{k}_a)\mathbf{E}_a + i\mathrm{e}^{i2k_{b,x}x}(\mathbf{E}_b\cdot\mathbf{k}_b)\mathbf{E}_b \\ & + i\mathrm{e}^{i(k_{a,x}+k_{b,x})x}((\mathbf{E}_a\cdot\mathbf{k}_b)\mathbf{E}_b + (\mathbf{E}_b\cdot\mathbf{k}_a)\mathbf{E}_a).\end{aligned} \tag{3.50}$$

Again, we see that the first two terms arise exclusively from individual beams and only consider the latter two terms. Continuing with an approach identical to the one for ED SHG, the unreflected SHG fields can now be obtained by substituting Eqs. (3.24 and 3.50) into Eqs. (2.32), yielding

$$\begin{aligned}\underline{\mathbf{E}}(0) = {}& \epsilon_0 i\delta'\frac{n\omega}{c}\mathrm{e}^{i\underline{k}_x x}\Big(\int_{-D}^{0}\underline{\mathbf{G}}(0-z_0)\mathrm{e}^{i(w_{a,+}+w_{b,+})z_0}dz_0\cdot(\mathbf{E}_{\mathrm{T},a,+}\cdot\hat{\mathbf{k}}_{b,+})\mathbf{E}_{\mathrm{T},b,+} \\ & + \int_{-D}^{0}\underline{\mathbf{G}}(0-z_0)\mathrm{e}^{i(w_{a,+}+w_{b,-})z_0}dz_0\cdot(\mathbf{E}_{\mathrm{T},a,+}\cdot\hat{\mathbf{k}}_{b,-})\mathbf{E}_{\mathrm{T},b,-} \\ & + \int_{-D}^{0}\underline{\mathbf{G}}(0-z_0)\mathrm{e}^{i(w_{a,-}+w_{b,+})z_0}dz_0\cdot(\mathbf{E}_{\mathrm{T},a,-}\cdot\hat{\mathbf{k}}_{b,+})\mathbf{E}_{\mathrm{T},b,+} \\ & + \int_{-D}^{0}\underline{\mathbf{G}}(0-z_0)\mathrm{e}^{i(w_{a,-}+w_{b,-})z_0}dz_0\cdot(\mathbf{E}_{\mathrm{T},a,-}\cdot\hat{\mathbf{k}}_{b,-})\mathbf{E}_{\mathrm{T},b,-}\Big) + [a\leftrightarrow b] \text{ and}\end{aligned} \tag{3.51}$$

$$\begin{aligned}\underline{\mathbf{E}}(-D) = {}& \epsilon_0 i\delta'\frac{n\omega}{c}\mathrm{e}^{i\underline{k}_x x}\Big(\int_{-D}^{0}\underline{\mathbf{G}}(-D-z_0)\mathrm{e}^{i(w_{a,+}+w_{b,+})z_0}dz_0\cdot(\mathbf{E}_{\mathrm{T},a,+}\cdot\hat{\mathbf{k}}_{b,+})\mathbf{E}_{\mathrm{T},b,+} \\ & + \int_{-D}^{0}\underline{\mathbf{G}}(-D-z_0)\mathrm{e}^{i(w_{a,+}+w_{b,-})z_0}dz_0\cdot(\mathbf{E}_{\mathrm{T},a,+}\cdot\hat{\mathbf{k}}_{b,-})\mathbf{E}_{\mathrm{T},b,-} \\ & + \int_{-D}^{0}\underline{\mathbf{G}}(-D-z_0)\mathrm{e}^{i(w_{a,-}+w_{b,+})z_0}dz_0\cdot(\mathbf{E}_{\mathrm{T},a,-}\cdot\hat{\mathbf{k}}_{\mathrm{T},b,+})\mathbf{E}_{b,+} \\ & + \int_{-D}^{0}\underline{\mathbf{G}}(-D-z_0)\mathrm{e}^{i(w_{a,-}+w_{b,-})z_0}dz_0\cdot(\mathbf{E}_{\mathrm{T},a,-}\cdot\hat{\mathbf{k}}_{b,-})\mathbf{E}_{\mathrm{T},b,-}\Big) + [a\leftrightarrow b],\end{aligned} \tag{3.52}$$

which can be integrated by utilizing Eq. (2.27). The resulting s polarized field leaving the nonlinear medium can be written as

$$\begin{aligned}\underline{E}^s_{\mathrm{out}}(-D) = {}& \mathrm{e}^{i\underline{w}D}i\delta'\frac{n\omega}{c}\frac{\underline{\omega}^2}{2c^2\underline{w}}\underline{t}^s_{23}\sum_{\phi\beta\gamma}\underline{K}^s_\phi\Phi'_{\phi\beta\gamma}K^s_{b,\gamma}\Big(K^p_{a,\beta}(\hat{\mathbf{p}}_{a,\beta}\cdot\hat{\mathbf{k}}_{b,\gamma})E^s_{b,0}E^p_{a,0} \\ & + K^s_{a,\beta}(\hat{\mathbf{s}}\cdot\hat{\mathbf{k}}_{b,\gamma})E^s_{b,0}E^s_{a,0}\Big) + [a\leftrightarrow b],\end{aligned} \tag{3.53}$$

where $(\hat{\mathbf{s}} \cdot \hat{\mathbf{k}}_{b,\gamma}) = 0$. Thus, the expression further simplifies into

$$
\begin{aligned}
\underline{E}^s_{\text{out}}(-D) = \mathrm{e}^{i\underline{w}D} i\delta' \frac{n\omega}{c} \frac{\underline{\omega}^2}{2c^2\underline{w}} \underline{t}^s_{23} & \\
\times \sum_{\phi\beta\gamma} \underline{K}^s_\phi \Phi'_{\phi\beta\gamma} K^s_{b,\gamma} K^p_{a,\beta} (\hat{\mathbf{p}}_{a,\beta} \cdot \hat{\mathbf{k}}_{b,\gamma}) E^s_{b,0} E^p_{a,0} + [a \leftrightarrow b]. &
\end{aligned}
\tag{3.54}
$$

Finally, the total s-polarized SHG field leaving the nonlinear layer can be written for the two-beam case as

$$
\begin{aligned}
\underline{E}^s_{\text{out}}(-D) = \mathrm{e}^{i\underline{w}D} \frac{\underline{\omega}^2}{2c^2\underline{w}} \underline{t}^s_{23} & \\
\times \sum_{\phi\beta\gamma} \underline{K}^s_\phi \Phi'_{\phi\beta\gamma} \Bigg[& \underline{\hat{\mathbf{s}}} \cdot \boldsymbol{\chi}^{(2)} \cdot \Big(\hat{\mathbf{p}}_{a,\beta} \hat{\mathbf{p}}_{b,\gamma} K^p_{a,\beta} K^p_{b,\gamma} E^p_{a,0} E^p_{b,0} \\
& + \hat{\mathbf{s}} \hat{\mathbf{p}}_{b,\gamma} K^s_{a,\beta} K^p_{b,\gamma} E^s_{a,0} E^p_{b,0} + \hat{\mathbf{p}}_{a,\beta} \hat{\mathbf{s}} K^p_{a,\beta} K^s_{b,\gamma} E^p_{a,0} E^s_{b,0} \\
& + \hat{\mathbf{s}} \hat{\mathbf{s}} K^s_{a,\beta} K^s_{b,\gamma} E^s_{a,0} E^s_{b,0} \Big) \\
+ i\delta' \frac{n\omega}{c} K^s_{b,\gamma} K^p_{a,\beta} (\hat{\mathbf{p}}_{a,\beta} \cdot \hat{\mathbf{k}}_{b,\gamma}) E^s_{b,0} E^p_{a,0} \Bigg] + [a \leftrightarrow b], &
\end{aligned}
\tag{3.55}
$$

which is the primary result of this section. Once more, our general notation proves convenient as it allows for a relatively easy comparison between the contributions from ED and MP processes to the total two-beam SHG.

4. EXPERIMENTS AND SAMPLES

In this Chapter, we describe our experimental methodology for the characterization of the SHG response for the single- and two-beam schemes analyzed in Chapter 3, apply them to a variety of material geometries, connect the experiments with the previous analysis and discuss their weaknesses and strengths. In addition, we will describe the materials and samples studied in this work, describe our motivation for studying them and provide a brief overview on the role of the said materials in optics.

4.1 Single-beam setup

In this section, we will describe the experimental methodogy for the study of ED SHG. We begin by describing the setup itself, followed by the description and examination of the different experiments it enables. We will also consider the connection between the experiments and the analysis as well as certain approximations that are useful for particular geometries used in the actual experiments.

The setup used for the single-beam nonlinear characterization is illustrated in (Fig. 4.1). A pulsed Nd:YAG laser (Ekspla PL 2200) with a wavelength of 1064 nm, repetition rate of 1 kHz and pulse length of 70 ps was used as the light source. After leaving the laser, the beam power was controlled by a half-wave plate (HWP), followed by a linear polarizer (LP). Finally, before the sample, the polarization state of the laser can be controlled with a motorized quarter-wave plate (QWP) in conjunction with the aforementioned LP. In order to control the angle of incidence, the sample holder was placed on a motorized rotation stage. Lastly, prior to the detection of SHG with a (Hamamatsu H6779-01) photomultiplier tube (PMT) connected to an oscilloscope, the polarization state of the detected SHG was chosen with a LP. In order to ensure that only SHG is detected and that all of the detected SHG is generated from the sample, visible-blocking and infrared-blocking filters were placed immediately before and after the sample, respectively. In addition, a lens was placed

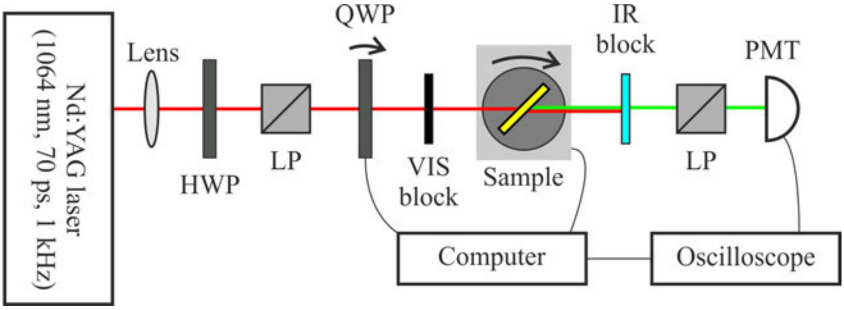

Figure 4.1: Schematic of the single-beam setup, with the following notation: HWP - half-wave plate, LP - linear polarizer, QWP - quarter-wave plate, VIS block - visual filter, IR block - infrared filter, PMT - photomultiplier tube. The red and green lines denote beams at 1064 nm and 532 nm, respectively.

before the polarization control in order to focus the beam weakly on the sample for increased SHG. The spot size at the sample was estimated to be a few hundred micrometers. Finally, both of the motorized stages and the oscilloscope are controlled by a computer running a measurement automatization software so that polarization and angle of incidence controlled experiments can be realized.

The motorized control of the incident polarization and the angle of incidence enables two types of measurements depending on which quantity is varied. Let us first consider a measurement where the control variable is the angle of incidence while the polarization control is kept constant. This, the more traditional of the two, is known as the Maker fringe experiment [57,58]. In principle, the Maker fringe method enables quantitative determination of SHG response and has been used widely for second-order nonlinear characterization [87–90]. Unfortunately, there are technical challenges for such characterization as it is difficult to perform measurements where absolute ratio between the SHG power and the power of the fundamental beam is obtained. In addition, it is common for a sample to have more than one source of SHG, e.g., the two interfaces for a plate of glass. However, the latter phenomenon can be convenient because if the SHG susceptibility is known for one of the sources, the unknown SHG susceptibility can be obtained by carefully analysing the fringes resulting from a varying phase-mismatch between the two SHG fields as the angle of incidence changes. Indeed, this is often the case for thin film samples, as they are usually fabricated on a glass substrate of some kind, and it is often sufficient to only consider SHG from the thin film and from the back surface of the substrate. In this case, the dependence of the varying phase mismatch on the angle of incidence depends only on the dispersion of the substrate between the sources. As the SHG fields from the two sources interfere, the resulting irradiance can be written as

$$I \propto \left| \mathbf{E}_1^{\mathrm{SHG}} + \mathbf{E}_2^{\mathrm{SHG}} \mathrm{e}^{i\phi(\theta)} \right|^2 , \tag{4.1}$$

where I is the total SHG irradiance, E_1^{SHG} is the generated SHG field from the material of interest, E_2^{SHG} is the generated SHG from the substrate and $\phi(\theta)$ is an angle of incidence dependent phase factor which will span over multiple rounds of 2π for a thick substrate, resulting in fringes in a measurement versus varying angle of incidence. Using the results of Section 3.2, the SHG fields can be expanded in terms of the susceptibility components, and the unknown SHG susceptibility can be determined. From here on, this is called *substrate referenced Maker-fringe experiment.*

The above notwithstanding, it is very complicated to determine the SHG susceptibility of a thin source from the corresponding SHG signal using a Maker fringe experiment. Due to the fact that the angle of incidence varies, the convenient formulation of polarization signatures described in Section 3.3 loses some of its usefulness as the polarization signatures denoted by $f^{\zeta,\eta,\kappa}$ depend on the angle of incidence in an extremely complex manner. However, this unfortunate problem can be mitigated by applying certain approximations. If an approximate signal magnitude estimation is sufficient and the nonlinear system of interest lays on a substrate with known nonlinear behavior, it is possible to consider the unknown thin source as an effective surface as well as neglect the tensorial nature of SHG altogether. As a result, the ratio of the SHG fields itself is the quantity of interest, and the analysis reduces to solving the ratio of fields in Eq. (4.1) by examining the visibility of the fringes. It should be noted though, that this is a very rough approximation and suitable only for the analysis of general trends and signal levels. From here on this is called *scalar approximation.*

Another useful approximation is to neglect some or all of the reflections and the resulting phenomena, which are the main source of complexity in the problem. This can be done conveniently by setting the appropriate Fresnel reflection coefficients to zero, effectively removing the summation over propagation directions $\phi, \beta\,\gamma$ in Eq. (3.41) so that few or even only one term remains. Consequently, by choosing the polarizations for the fundamental beam and the detected SHG well, only a few terms remain nonzero in the summation over i, j, k for a material with high symmetry.

Lastly, for nonlinear materials with high indices of refraction at both the fundamental and SHG frequencies or relatively small dispersion, some of the otherwise independent SHG tensor components may become *de facto* non-independent and thus inseparable in practice. In order to overcome this difficulty, a measurement scheme with more degrees of freedom can be used, such as one where polarization states for both fundamental beam as well as that of the detected SHG are controlled. The other option is to settle for the separable tensor components.

As mentioned above, the other type of experiment for the SHG characterization consists of a measurement or measurements where the polarization state of the fundamental beam is controlled while the angle of incidence and the polarization state of the SHG beam are kept constant. Here, we will label this method as the *polarization controlled* experiment. With the polarization controlled experiment, the polarization signatures and thus the SHG susceptibility can be fully characterized for in-plane isotropic samples provided, that the polarization space for the fundamental and SHG beams is sufficiently comprehensive [26,91]. This involves multiple measurements if only the polarization state of the fundamental beam is varied within an experiment [91]. For example, four experiments with particular combinations of polarization states for the fundamental beam before the wave-plate and detected SHG are sufficient in conjunction with a rotating QWP to uniquely determine the relative values of polarization signatures $f^{p,p,p}$, $f^{p,s,s}$ and $f^{p,p,s} + f^{p,s,p}$ as well as $f^{s,p,p}$, $f^{s,s,s}$, $f^{s,p,s} + f^{s,s,p}$ [91, 92].

The above result does not depend on the system geometry or the symmetry of the material. For a surface response, these signatures can be uniquely connected to the non-vanishing surface SHG tensor components by

$$\mathbf{f} = \mathbf{U} \cdot \boldsymbol{\chi}_V^{(2)}, \tag{4.2}$$

where $\mathbf{f}$ is a vector containing the polarization signatures mentioned above, $\boldsymbol{\chi}_V^{(2)}$ is a vector containing all the nonvanishing tensor components and $\mathbf{U}$ is a matrix whose elements only depend on the linear material properties and the geometry of the experiment and can thus be calculated beforehand [93]. The above is also true for bulk SHG from a thin in-plane isotropic layer with the only change being different values for the elements of $\mathbf{U}$. The elements of $\mathbf{U}$ are given by the terms of the summation over i, j, k of Eq. (3.41), again highlighting the usefulness of the separation of variables in Eq. (4.2).

It is worth noting, that polarization controlled experiments are best suited for the characterization of the relative SHG tensor structure, rather than the absolute values for susceptibility. This is due to the aforementioned fact that it is very difficult to measure absolute power levels accurately with a PMT without a proper reference. In addition, it is not possible to reference the SHG from the nonlinear material to the SHG from the substrate surface using the visibility of Maker fringes since the angle of incidence is constant. To circumvent this problem, it is possible to use a known nonlinear crystal such as crystalline quartz as reference. The results of Section 3.2 can be easily modified for this as well. Nonetheless, the polarization controlled measurements are suitable only if there is one clear dominating SHG source, because then the other interfering sources can be neglected.

4.2 Two-beam setup

In this section, we will describe the experimental method to study the presence of MP SHG using a setup with two non-collinear beams, as discussed in Section 3.3. Using the labels defined in the previous section, our two-beam experiment is a polarization controlled experiment. In other words, in a single measurement the polarization state of one of the beams incident on the sample is varied continuously while the polarization state of the other incident beam as well as that of the detected SHG beam is kept constant. In addition, the angles of incidence and thus, detection, are kept constant.

A schematic of the two-beam setup is shown in (Fig. 4.2). The two-beam setup is similar to the single-beam setup described in the previous section, except for the division of the fundamental beam into two parts with a beam splitter (BS). A delay line is added to one of the beams, labelled b, to ensure that the pulses coincide temporally at the sample. The other beam is labelled a. Before coinciding spatially at the sample, both of the beams pass a weakly focusing lens (gray ellipses in Fig. 4.2), power and polarization control optics (blue boxes in Fig. 4.2) and a visible-blocking filter, in that order (black bars in Fig. 4.2). In a measurement, the polarization state of beam b is continuously varied with a motorized QWP. It should be noted that filtering of the infrared light prior to the polarization control for SHG is not necessary, since neither of the incident beams propagates towards that direction.

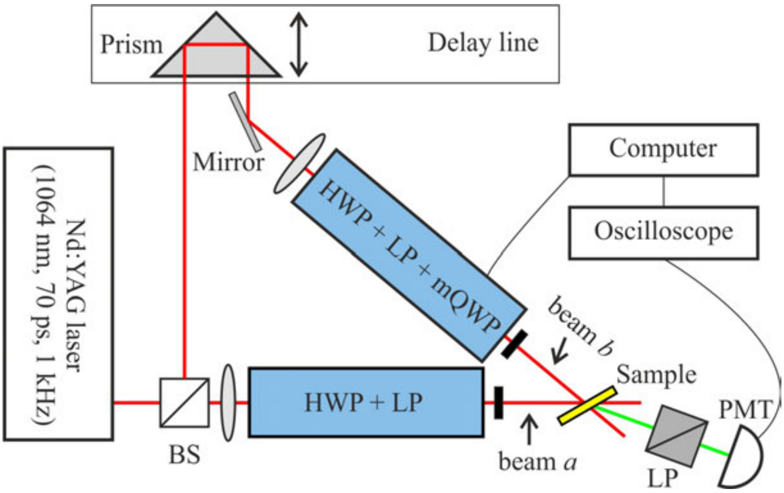

Figure 4.2: A schematic of the two-beam setup with the following notation: BS - beam splitter, HWP - half-wave plate, LP - linear polarizer, mQWP - motorized quarter-wave plate, PMT - photomultiplier tube. The blue boxes responsible for power and polarization control, and are preceded by lenses (gray ellipses) and succeeded by visible-blocking filters (black bars). The red and green lines denote beams at 1064 nm and 532 nm, respectively. The beam with narrower (wider) angle of incidence is labelled beam b (a).

For thick samples, the two-beam experiment is known to be able to separate the ED surface SHG response from the MP bulk SHG response in a single measurement if proper polarizations for beam b prior to the QWP, beam a and detected SHG beam are chosen [64, 66, 67]. By examining Eq. (3.55), it can be seen that the same holds true for the separation of ED SHG and MP SHG arising from δ', although the relative contribution from the material parameters is quantitatively different.

4.3 Multilayer composite materials

The requirement for non-centrosymmetry is one of the most fundamental problems in the search for materials with high second-order nonlinearity. Certain crystals are an obvious class of materials with a low symmetry, but it would be highly beneficial to expand the range of nonlinear materials suitable for applications. Multiple approaches have been found to break the symmetry of otherwise centrosymmetric materials, including for example external poling [31–33], applied directional strain [36–38], and the nonuniform inclusion of plasmonic metal particles within the material [94]. The two latter approaches are enabled by the fact that they essentially morph the material to have effective layers, and even for fully centrosymmetric materials, the symmetry always breaks at interfaces that belong to the symmetry group $C_{\infty v}$ or lower. Thus, another obvious solution is to fabricate composite materials with multiple different thin layers stacked on top of each other. If the layers are ordered in a cycle, then, provided that a sufficiently large stack of sufficiently thin layers can be fabricated, the system acts as an effective material with $C_{\infty v}$ symmetry. Here, we label such a material as a multilayer composite material (MCM).

In this work, we studied MCMs consisting of cycles of three materials. This is the simplest possible system since, for a cycle of two, the system has a center of inversion along the interface normal in the middle of either of the sublayers in the bulk of the MCM. For the cycle of three MCM studied in this work, we denote the constituent materials with A, B and C, which results in a composite where the stack [A-B-C] is repeated (see Fig. 4.3a). We note that this approach to break centrosymmetry has already been demonstrated [40]. Our goal is to expand on the earlier work by improving the efficiency of the nonlinear process as well as by examining the material space and its effect on the SHG efficiency.

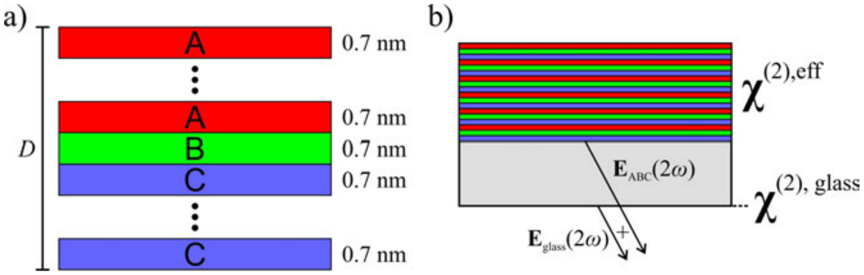

Figure 4.3: a) Schematic of the MCM stack consisting of [A-B-C] cycles. b) Diagram of the two sources present in substrate referenced SHG measurement from a MCM film on a glass substrate.

The studied sample consists of layers of TiO_2 (A), Al_2O_3 (B) and In_2O_3 (C) with refractive indices of $n_A = 2.1$, $n_A = 1.5$-1.7 and $n_A = 2.2$, respectively [95–97]. The motivation behind the choice of materials is that, as a rule of thumb, the surface nonlinearity is connected with the refractive index contrast between the surrounding media [70]. The layers were deposited as successive [A-B-C] cycles using atomic layer deposition (ALD). This process suits our purposes well as it can produce sufficiently thin layers and is compatible with nanophotonic circuitry [98].

Three MCM films with total thickness of 2.1 nm, 25 nm and 50 nm were fabricated on a borosilicate glass substrate (Schott BOROFLOAT33) with a thickness of 0.5 mm. The samples were fabricated at Ghent University-IMEC using ALD. The deposition process was enhanced by cleansing the system periodically with pulses of oxygen plasma (radio frequency (RF) power: 200 W, frequency: 13.56 MHz, pressure: 1.2×10^{-5} bar, temperature: 120°C) between pulses of the respective metal-organic precursor (pressure: 6.0×10^{-5} bar). In addition, we pumped the chamber to a high vacuum between each gas pulse. The precursors used for materials A, B and C were (dimethylamido)titaniuma, Trimethylaluminium, Tris(2,2,6,6-tetramethyl-3,5-heptanedionato) indium(III), respectively.

Before the nonlinear experiments, ellipsometric measurements were conducted in order to determine the refractive indices of the MCMs. The nonlinear characterization was conducted using a substrate referenced Maker-fringe experiment (see Fig. 4.3b) using a setup similar to the single-beam setup described in Section 4.1. However, for this experiment, a Ti:sapphire laser (Mai Tai HP, Spectra-Physics; wavelength: 980 nm; pulse duration: 100 fs) was used instead of the Nd:YAG laser, a parabolic mirror was used to focus the beam (focal length: 5 cm) instead of a lens, and a femtowatt detector (Thorlabs PDF10A) in conjunction with a collecting lens was used for the detection. p polarized light was used for the fundamental beam and the polarization of the detected SHG was not controlled.

The SHG suceptibility tensor components can be obtained by accounting for symmetry, applying proper approximations and using Eqs. (3.36 and 3.37) both for the MCM film and for the back surface of the glass substrate.

4.4 Silicon nitride

Silicon nitride (SiN) is a material that is compatible with the complementary metal-oxide semiconductor (CMOS) platform and has been recently shown to possess significant SHG response from the bulk of the material [71, 99, 100]. This is very significant, since many potential applications for photonic integrated circuits rely on nonlinear processes including SHG and, as discussed above, SHG enabling non-centrosymmetry is a difficult requirement. However, despite some theories being proposed, the physical origin of the symmetry breaking in SiN films is still unknown [71, 101–105]. For these reasons the recent research on the nonlinear optical properties of SiN fabricated with different techniques has been extensive [71, 99, 100, 106].

In this work, we expand on the previous research by studying whether SHG from SiN films fabricated using plasma-enhanced chemical vapor deposition (PECVD) technique can be further increased by the tuning of the chemical composition of the films. PECVD was chosen as the fabrication method since although SiN fabricated by sputtering has been shown to exhibit very strong SHG, the extreme sensitivity of the SHG response and even the material symmetry towards material composition indicates that the fabrication process is difficult to control [99, 100]. On the other hand, SiN fabricated using PECVD has been shown to exhibit a consistent SHG response and material symmetry [71, 106, 107]. In addition, we note that SiN prepared using low pressure chemical vapor deposition (LPCVD) showed little SHG compared to that observed from SiN fabricated using PECVD.

To study the composition dependence of the nonlinearity, five samples, labelled S10, S20, S30, S35 and S40, were fabricated on silica substrates using the PECVD process. The fabrication of samples S10, S20, S30 and S40 was carried out at Tampere University of Technology (Plasmalab 80 plus, Oxford Instruments) using a gas mixture consisting of 2% SiH_4/N_2 and NH_3. To adjust the composition of the fabricated film, the flow rate of 2% SiH_4/N_2 was kept constant at 1000 sccm, while the flow rate of NH_3 was varied for different samples: 10 sccm - S10, 20 sccm - S20, 30 sccm - S30 and 40 sccm - S40. The process pressure was 1000 mTorr, deposition temperature was 300°C, and the plasma was created using a RF field with 13.56 MHz frequency and 20 W power. The S35 sample was fabricated at Ghent University-IMEC (Advanced Vacuum Vision 310 PECVD) with a gas mixture of SiH_4 - 40 sccm, N_2 - 1960 sccm and NH_3 - 35 sccm. For the fabrication of S35 sample, the process pressure and temperature were 650 mTorr and 300°C, respectively, and the plasma was generated with a cycle of one second of RF field (power: 30 W, frequency: 13.73 MHz) and five seconds of low frequency field (power: 50 W, frequency: 100-300 kHz).

Again, ellipsometric measurements were carried out prior to the nonlinear characterization in order to determine the refractive indices and exact thicknesses of the films. The nonlinear characterization consisted of two different experiments: 1) a polarization controlled single-beam measurement for the characterization of the SHG tensor structure and 2) a quartz referenced Maker fringe experiment to calibrate the absolute values for the tensor components.

In the polarization controlled experiment, four measurements were carried out with an angle of incidence of 60° and four different combinations of initial polarization of the fundamental beam prior to the QWP and detected SHG polarization in order to uniquely determine the relevant polarization signatures [71, 91, 92]: $(\hat{\mathbf{p}}+\hat{\mathbf{s}})/\sqrt{2}$, $\underline{\hat{\mathbf{p}}}$; $(\hat{\mathbf{p}}-\hat{\mathbf{s}})/\sqrt{2}$, $\underline{\hat{\mathbf{p}}}$; $(\hat{\mathbf{p}}+\hat{\mathbf{s}})/\sqrt{2}$, $(\underline{\hat{\mathbf{p}}}+\underline{\hat{\mathbf{s}}})/\sqrt{2}$; $(\hat{\mathbf{p}}-\hat{\mathbf{s}})/\sqrt{2}$, $(\underline{\hat{\mathbf{p}}}+\underline{\hat{\mathbf{s}}})/\sqrt{2}$. These polarization signatures are then linear combinations of the non-vanishing SHG susceptibility tensor components as per Eq. (3.41).

In the Maker fringe measurement, p polarized SHG was detected with s polarized fundamental field. The polarizations were chosen as such in order to have only one SHG susceptibility tensor component, $\chi^{(2)}_{zxx}$, contribute to the SHG, which simplifies the analysis. The quartz measurement was carried out using a sample with a small wedge and at normal incidence so that both the polarization of the fundamental field and the polarization of the detected SHG were aligned along the quartz X axis, again ensuring simplicity of the analysis. Lastly, while measuring SHG, the quartz was moved slowly along the wedge so that the phase-matching was optimized, eliminating the *forward* phase-mismatch term (Φ_{---}) altogether. By fitting both of these measurements together and scaling for power, the absolute value of $\chi^{(2)}_{zxx}$ for SiN can be obtained.

In addition, motivated by the previously reported strong ED SHG and the possible additional degrees of freedom that MP SHG could provide, we studied the SiN film from Ref. [71] with the two-beam experiment. This sample is essentially identical to Sample S30 except for thickness of 800 nm. To separate the ED and MP contributions to s polarized SHG, the two-beam experiment was performed with polarization of the beam a being $(\hat{\mathbf{p}}-\hat{\mathbf{s}})/\sqrt{2}$, polarization of the beam b prior to the QWP being $\hat{\mathbf{p}}$ and the angles of incidence for beam a and beam b being $\theta_a = 58.3°$ and $\theta_b = 32.0°$, respectively. By fitting this measurement with Eq. (3.55), the relative values of δ' and $\chi^{(2)}_{xxz}$ can be obtained [64, 66, 85].

4.5 Indium selenide

Chalcogenide glasses are an interesting group of materials due to the fact that many of their properties, such as optical nonlinearity and band gap, can be tuned by material composition [108]. In addition, chalcogenide glasses exhibit high refractive index, high nonlinearity and high photosensitivity [109–113]. Indium selenide (InSe), a chalcogenide glass and a group III-VI semiconductor, has recently gained attention due to its possible applications in energy conversion and in opto-electronics [114–116]. Importantly for the scope of this work, InSe can exist in different phases depending on the stoichiometric ratio of the constituent elements [73]. As such, different types of SHG sources can arise in InSe due to different symmetry properties of the different phases.

Three InSe thin films with varying thickness (40 nm, 100 nm and 190 nm) were fabricated using a cost-effective thermal evaporation technique. The InSe films were evaporated from a bulk InSe source to BK7 glass substrates using a melt quenching method described in Ref. [117] with vacuum chamber pressure of 10^{-5} Torr and temperature of 300 °C. The thickness was controlled by the evaporation time. The bulk source was fabricated by melting a mixture of 62% Se and 38% In (Sigma Aldrich, 5N purity) at the temperature of 1000 °C. Finally, the chemical composition and surface roughness were verified using energy-dispersive X-ray spectroscopy and atomic force microscopy, respectively.

Once more, ellipsometric measuments were carried out to determine the linear properties and precise thicknesses of the samples. Preliminary experiments indicated, that the sample was in-plane isotropic and that the interference between the SHG signals from the film and the back surface of the substrate could not be neglected. Thus, the samples were characterized with the substrate referenced Maker fringe experiment with p polarized fundamental beam and p polarized SHG detection. Similarly to the case of MCM films, The SHG suceptibility can be characterized with Eqs. (3.36 and 3.37) for both sources.

4.6 Nanoisland films

Metal nanostructures and metal-dielectric composites (collectively labelled MNS) have been under intense study due to their highly tunable optical properties. This is due to the fact that their optical properties are governed by localized surface plasmon resonances and subsequent intense local fields (LF), whose distribution, spectrum and strength depend sensitively on the size and shape of the MNS, the surrounding environment and the metal in question [118–120]. These advantageous properties have been utilized in various applications, including solar cells, Raman spectroscopy and thin optical components [121–123]. From the perspective of our work, MNS are especially interesting since the nonlinear effects scale with a high power of the field, enabling extremely high tuning and enhancement of the nonlinearity [74, 119, 124–126]. Our goal was to investigate the enhancement of MNS coated with a dielectric by tuning the coating thickness.

As mentioned above, we studied gold nanoisland films deposited on a glass substrate and coated with thin layers of TiO_2 in order to determine whether the LFs, and thus, the SHG response can be tuned by varying the coating thickness. For this purpose, gold nanoisland films were prepared by first depositing a 5 nm thick solid gold film onto a fused silica substrate, followed by air annealing at 500 °C for 120 minutes. As a result, gold nanoparticles shaped like truncated spheres with truncation angle of 50°, average diameter of 20 nm and relatively high size variation were formed on the substrate. These films were subsequently coated with various thicknesses (from 3.2 nm to 97.9 nm) of TiO_2 by using ALD (Beneq TFS-200 reactor). The spectra of the coated nanoisland films were measured with a spectrophotometer (Specord 50). A schematic of a truncated and coated gold sphere and an SEM image of the nanoisland film with a diameter distribution diagram are shown in (Fig. 4.4).

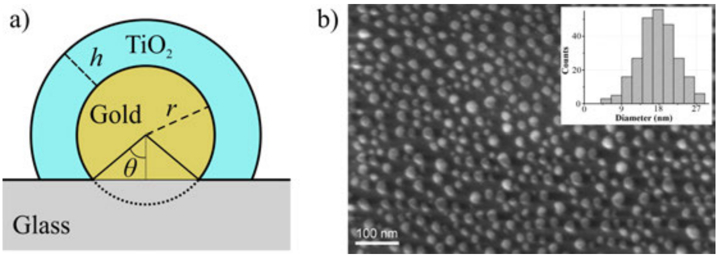

Figure 4.4: a) Schematic of a truncated sphere with a radius r and truncation angle θ coated with h thick layer of TiO_2. b) SEM image of the nanoisland film. Inset: Diameter distribution of the nanoislands.

A film of truncated spheres coated with a layer of dielectric whose thickness is of the order of the sphere diameter is an extremely complicated structure for a proper nonlinear analysis. Thus, a substrate referenced Maker fringe experiment with scalar approximation was used to estimate the effective signal level. As a result, all of the obtained signal levels from the film are estimated with respect to the signal level from the back surface of the substrate. This is justified by the fact that we are mainly interested in the relative magnitude of SHG from films with different TiO_2 coating thicknesses. This simple analysis can be carried out by using only Eq. (4.1) and setting the fields as scalar.

5. RESULTS

In this Chapter, we present the results of the experiments described in Chapter 4 and assess them by applying the analysis derived in Chapters 2 and 3. This Chapter is split and ordered according to the publications as they represent the key results of our research and stand on their own as evidenced by the fact that they are published separately. Finally, we will discuss briefly the scientific impact of the results from the perspective of the general motivations of this research as laid out in Chapter 1.

5.1 SHG from multilayer structures

In this section, we outline the results reported in **Publication I**. The nonlinear response of MCM films was characterized using a substrate referenced Maker-fringe experiment described in Section 4.3. In addition, preliminary measurements were carried out to support the analysis of the results. The preliminary measurements consisted of ellipsometry and nonlinear measurements on the glass substrate.

Table 5.1: Results from the ellipsometric measurements for MCM films and the surface SHG susceptibility values for glass [93].

Refractive index		Surface SHG susceptibility	$\times 10^{-22} m^2/V$
$n_{\mathrm{MCM}}^{\mathrm{av}}$	1.97	$\chi_{\mathrm{glass},xxz}^{(2),\mathrm{sf}}$	14.6
$\underline{n}_{\mathrm{MCM}}^{\mathrm{av}}$	2.10	$\chi_{\mathrm{glass},zxx}^{(2),\mathrm{sf}}$	7
$n_{\mathrm{glass}}^{\mathrm{av}}$	1.4633	$\chi_{\mathrm{glass},zzz}^{(2),\mathrm{sf}}$	93
$\underline{n}_{\mathrm{glass}}^{\mathrm{av}}$	1.4766		

The ellipsometric measurements were carried out in order to determine the refractive indices of the MCMs and revealed that the MCM films exhibit a small birefringence that our model cannot account for. Thus, the average refractive indices were used in the analysis. The refractive indices are shown in Table 5.1. The surface susceptibility of glass has been studied previously for BK7 glass [93]. The nonlinear measurements on BK7 and borosilicate glass showed almost identical nonlinear signals, indicating that the SHG susceptibility values of BK7 can be used for the borosilicate substrates of our samples. The surface SHG susceptibility values of glass used for the nonlinear characterization are shown in Table 5.1.

The Maker-fringe measurements were carried out for three MCM samples of 50 nm, 25 nm and 2.1 nm thickness fabricated on top of a borosilicate glass substrate. In addition, a bare substrate was studied for reference. The results of the Maker-fringe measurements are shown in (Fig. 5.1a), where the zero thickness refers to the bare substrate. As expected, the increasing number of interfaces results in an increased signal as the thickness grows. This is in line with our interpretation that the MCM can be treated as an effective film with $C_{\infty v}$ symmetry that is the same symmetry possessed by the glass surface. Thus, using Eq. (3.14), it can be seen that SHG from p polarized excitation is fully p polarized for both the MCM film and the substrate surface. As a result, both the surface SHG susceptibility of glass and the effective bulk SHG susceptibility of the MCM medium can be written as

$$\begin{aligned}\chi_j^{(2)} &= 2\chi_{j,xxz}^{(2)} \cos \underline{\theta}_j \sin \theta_j \cos \theta_j + \chi_{j,zxx}^{(2)} \sin \underline{\theta}_j \cos \theta_j \cos \theta_j \\ &+ \chi_{j,zzz}^{(2)} \sin \underline{\theta}_j \sin \theta_j \sin \theta_j .\end{aligned} \tag{5.1}$$

where j denotes MCM or glass. Furthermore, using Eq. (4.1), the total irradiance is

$$\underline{I} = q|\underline{E}^p_{\mathrm{MCM}} + \underline{E}^p_{\mathrm{glass}}|^2, \tag{5.2}$$

where q is a proportionality factor and with the SHG field from glass being [41, 93]

$$\underline{E}^p_{\mathrm{glass}} = \frac{\underline{\omega}^2 \underline{t}^p_{31} (t^p_{12})^2}{c^2} \frac{(t^p_{32})^2}{\underline{w}_{\mathrm{glass}}} \chi^{(2)}_{\mathrm{glass}} \mathrm{e}^{2iw_{\mathrm{glass}} D_{\mathrm{glass}}} (E^p_0)^2. \tag{5.3}$$

As discussed in Section 4.3, the reflections occuring in the numerous layers of MCM films are very difficult to account for and are thus neglected. As a result, the SHG field from the MCM film can be fully described by Eqs. (3.36 and 3.37). However, the functional form can be simplified further by noting that the samples are extremely thin. Thus, by using Eq. (3.35), the phase mismatch factor can be approximated as $\Phi \approx iD_{\mathrm{MCM}}$, yielding

$$\underline{E}^p_{\mathrm{MCM}} = \frac{\underline{\omega}^2 \underline{t}^p_{31} (t^p_{12})^2}{c^2} \frac{\underline{t}^p_{32}}{\underline{w}_{\mathrm{MCM}}} D_{\mathrm{MCM}} \chi^{(2)}_{\mathrm{MCM}} \mathrm{e}^{i\underline{w}_{\mathrm{glass}} D_{\mathrm{glass}}} (E^p_0)^2. \tag{5.4}$$

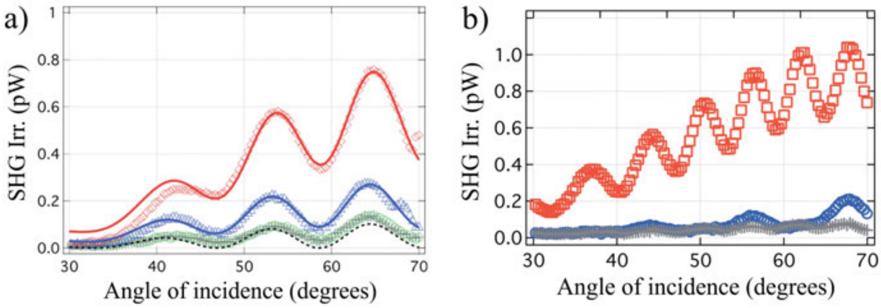

Figure 5.1: a) Substrate referenced Maker-fringe experiment results from MCM films with thickness of 50 nm - red diamonds, 25 nm - blue triangles 2.1 nm - green circles and 0 nm - gray crosses deposited on a borosilicate glass substrate. The markers represent experimental data and the lines represent fitted curves. b) Maker-fringe measurements from two samples attached to each other: Red - [ABC]-glass-glass-[CBA]; Blue - glass-[ABC]-[CBA]-glass; Gray - glass-glass. The figure is based on the results of **Publication I**.

Lastly, we note that it is extremely difficult to separate the two off-diagonal SHG tensor components χ_{xxz} and χ_{zxx} using a Maker-fringe measurement with our polarization configuration unless the material shows extremely high dispersion. Indeed, if the angles of incidence at the fundamental and SHG frequencies are identical $\underline{\theta} \approx \theta$, the two off-diagonal components are inseparable. Thus, we limit ourselves to fitting the results using three free parameters: $A_{zx} = 2\chi^{(2)}_{\mathrm{MCM},xxz} + \chi^{(2)}_{\mathrm{MCM},zxx}$, $\chi^{(2)}_{\mathrm{MCM},zzz}$ and the proportionality factor of Eq. (5.2). To connect the off-diagonal component to the SHG, Kleinman symmetry can be assumed to obtain an estimate $\chi^{(2)}_{\mathrm{MCM},xxz} = \chi^{(2)}_{\mathrm{MCM},zxx} = A_{zx}/3$.

The results of the Maker-fringe experiments fitted using the above analysis are shown in (Fig. 5.1a). The acquired values for the studied SHG components for the 25 nm and 50 nm thick MCMs are shown in Table 5.2. The 2.1 nm thick MCM was omitted due to the fact that we cannot verify whether the glass SHG or the MCM SHG dominates since the signal level is too close to the one from the bare substrate. The discrepancy between the acquired values for off-diagonal component A_{zx} is most likely due to the approximations and due to the signal being dominated by the diagonal component $\chi^{(2)}_{zzz}$. Taking the above into account, we feel that it is safe to report a value of the dominant component $\chi^{(2)}_{zzz}$ of 5 ± 2 pm/V.

Lastly, to verify that the observed nonlinearity is of bulk origin, we also measured SHG from glass-[ABC]-[CBA]-glass and [ABC]-glass-glass-[CBA] structures, and

Table 5.2: Separable SHG component values determined for MCM films of 25 nm and 50 nm thickness using substrate referenced Maker-fringe experiment.

	25 nm MCM	50 nm MCM
A_{zx}	1.44 ± 0.16 pm/V	0.78 ± 0.07 pm/V
$\chi^{(2)}_{zzz}$	6.0 ± 0.8 pm/V	6.1 ± 0.4 pm/V

compared the signal to that from two substrates put together. Results of these experiments are shown in (Fig. 5.1b). SHG from the glass-[ABC]-[CBA]-glass sample is almost as weak as that of the double substrate. This is expected for bulk nonlinearity since the [ABC]-[CBA] system has a center of inversion in the middle. On the other hand, the dispersion in the thick glass layer allows for much higher SHG with a smaller period of oscillation for the [ABC]-glass-glass-[CBA] case, and the imperfect visibility is explained by the temporal walkoff of the short femtosecond pulses. To summarize, these findings support the interpretation of the MCM film behaving like a effective bulk film.

In conclusion, we demonstrated high SHG nonlinearity of the order of 5 ± 2 pm/V for the dominant tensor component from our MCM films. This value is comparable to many common nonlinear materials [6]. As such, our results strongly support the proof of concept reported in Ref. [40] of multilayer structures as an effective new type of nonlinear material, for example, for use in conjunction with CMOS-compatible photonic components. Lastly, we note that the optimization could be taken further by increasing the refractive index contrast between the three materials or by fabricating thinner constituent layers, resulting in even higher nonlinearity [70].

5.2 Multipolar SHG from thin films

In this section, we outline the results reported in **Publication II**. In order to characterize the presence of MP SHG nonlinearity, we expanded the traditional two-beam method derived for thick samples to thin films and tested it for a SiN thin film. Preliminary experiments were unnecessary, since we used the SiN thin film from Ref. [71]. Thus, the SiN thin film was known to exhibit $C_{\infty v}$ symmetry, have thickness of $D = 800$ nm and refractive indices of $n = 1.94$ and $\underline{n} = 1.99$ for the fundamental and SHG wavelengths, respectively [71]. Lastly, the SHG signal from the SiN film is sufficiently strong so that SHG from the glass substrate could be neglected.

The traditional two-beam approach is based on the fact that by studying the s polarized SHG generated jointly from two non-collinear beams with particular polarizations, the MP contribution to the signal governed by δ' can be separated from the ED contribution to the signal governed by $\chi^{(2)}_{xxz}$ [64, 66, 85, 127]. The method is based on the unique determination of polarization signatures $f^{s,p,s}$ and $f^{s,s,p}$ and solving their relationship with ED and MP contribution.

Although the above method was developed for thick samples where reflections can be largely ignored, the result holds qualitatively for thin films as well. Indeed, by using Eq. (3.55) with $\underline{E}^s \propto f^{s,p,s}E^p_{a,0}E^s_{b,0} + f^{s,s,p}E^s_{a,0}E^p_{b,0}$ the relationship between the polarization signatures can be written as

$$\begin{bmatrix} f^{s,p,s} \\ f^{s,s,p} \end{bmatrix} = \begin{bmatrix} u_{11} & u_{12} \\ u_{21} & u_{22} \end{bmatrix} \begin{bmatrix} \chi^{(2)}_{xxz} \\ k\delta' \end{bmatrix}, \tag{5.5}$$

where the matrix elements are given by (see Section 3.3 for notation)

$$u_{11} = 2F\sin\theta_a \sum_{\beta,\gamma}(\Phi'_{-\beta\gamma} + \underline{r}_{21}\Phi'_{+\beta\gamma})K^p_{a,\beta}K^s_{b,\gamma} \tag{5.6}$$

$$u_{12} = iF\sum_{\beta,\gamma}(\Phi'_{-\beta\gamma} + \underline{r}_{21}\Phi'_{+\beta\gamma})K^p_{a,\beta}K^s_{b,\gamma}\mathrm{sign}(\gamma)\sin\left[\theta_a - \mathrm{sign}(\beta)\mathrm{sign}(\gamma)\theta_b\right] \tag{5.7}$$

$$u_{21} = 2F\sin\theta_b \sum_{\beta,\gamma}(\Phi'_{-\beta\gamma} + \underline{r}_{21}\Phi'_{+\beta\gamma})K^s_{a,\beta}K^p_{b,\gamma} \tag{5.8}$$

$$u_{22} = -iF\sum_{\beta,\gamma}(\Phi'_{-\beta\gamma} + \underline{r}_{21}\Phi'_{+\beta\gamma})K^s_{a,\beta}K^p_{b,\gamma}\mathrm{sign}(\gamma)\sin\left[\theta_a - \mathrm{sign}(\beta)\mathrm{sign}(\gamma)\theta_b\right], \tag{5.9}$$

with sign(i) = ±1 for $i = \pm$ and

$$F = \mathrm{e}^{i\underline{w}D}\frac{\omega^2\underline{t}^s_{23}\underline{C}^s}{2c\underline{w}}. \tag{5.10}$$

If reflection-related effects are ignored, i.e., all the Fresnel reflection coefficients are set to zero, the matrix elements in Eqs. (5.6-5.9) become

$$u_{11} = 2F'\sin\theta_a t^p_{a,12}t^s_{b,12} \tag{5.11}$$

$$u_{12} = -iF't^p_{a,12}t^s_{b,12}\sin(\theta_a - \theta_b) \tag{5.12}$$

$$u_{21} = 2F'\sin\theta_b t^s_{a,12}t^p_{b,12} \tag{5.13}$$

$$u_{22} = iF't^s_{a,12}t^p_{b,12}\sin(\theta_a - \theta_b), \tag{5.14}$$

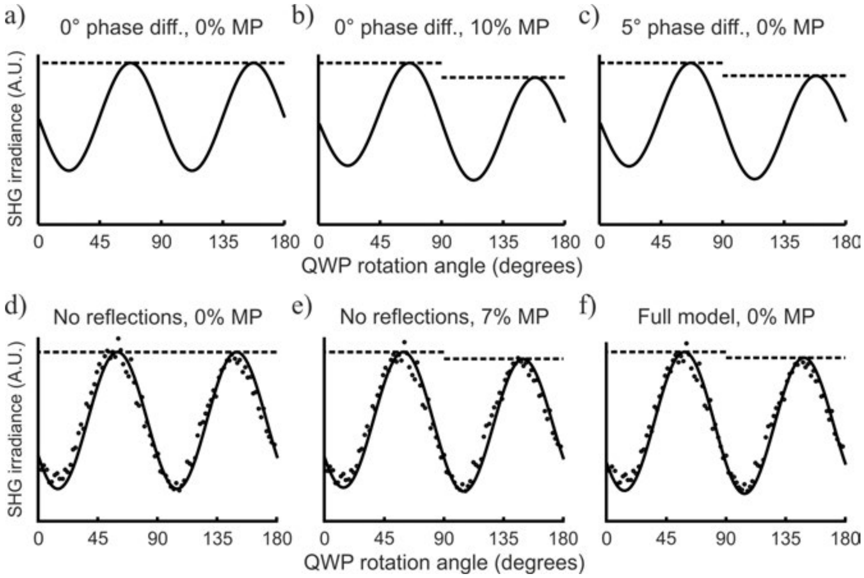

Figure 5.2: Simulations and results of two-beam polarization controlled experiment from a SiN thin film. a)-c): Simulation for the case a) without MP SHG and neglecting reflections, b) with 10% MP contribution to SHG and neglecting reflections and c) without MP SHG with reflections taken into account. d)-f): Experimental results (markers), fitted (lines) with d) no MP contribution allowed and neglecting reflections, e) MP contribution allowed and neglecting reflections (predicted MP contribution: 7%) and f) MP contribution allowed and reflections taken into account (predicted MP contribution: 0%). Dashed lines are guides for eyes only. The figure is based on the results of **Publication II**.

with

$$F' = \mathrm{e}^{i\underline{w}D} \frac{\underline{\omega}^2 \underline{t}^s_{23} \Phi'_{-,-,-}}{2c\underline{w}}, \tag{5.15}$$

which is almost identical to the thick sample case [67]. The important thing to note here is that the phase difference between $f^{s,p,s}$ and $f^{s,s,p}$ and the resulting signature in the measured signal arises exclusively from the MP parameter [64]. Simulations of this signature for a case without (a) and with (b) MP contribution are shown in (Fig. 5.2a and Fig. 5.2b). However, if the reflections are properly accounted for and Eqs. (5.6-5.9) are used, a phase difference between $f^{s,p,s}$ and $f^{s,s,p}$ is present even without a MP contribution. This situation is simulated in (Fig. 5.2c) with the dashed lines being guides for the eye to indicate the peak heights in the graph. A difference in peak heights is evidence of either MP contribution or a phase difference originating from something else, such as reflections.

The findings were verified experimentally by studying our SiN film with a polarization-controlled two-beam experiment discussed in Chapter 4, and fitting the results both by neglecting reflections and by taking them fully into account. The results are shown in (Fig. 5.2d-f). The results were fitted by neglecting reflections and allowing only ED contribution (Fig. 5.2d), by neglecting reflections and allowing both ED and MP contributions (Fig. 5.2e) and by taking the reflections into account and allowing both ED and MP contribution (Fig. 5.2f). As expected, there is no peak height difference without reflections nor MP contribution (Fig. 5.2d) and the analysis predicts 7% MP contribution if they are allowed and reflections are neglected (Fig. 5.2e). However, if the reflections are taken into account, the analysis yields essentially zero MP contribution and the phase difference is completely explained by ED SHG and reflections.

In summary, we have extended the analytical treatment of MP two-beam SHG from thick material systems to thin films with thicknesses of the order of optical wavelengths. The most important difference between the models is the presence of reflection-based phenomena, which must be taken into account. We showed theoretically and experimentally that neglecting these effects will result in qualitatively erroneous results outside the case of a dominating multipolar contribution and quantitatively erroneous results for all cases. We highlight that even though this analysis was conducted for the case with nonvanishing bulk-type dipolar SHG response, our result still holds for thin film samples where the dipolar SHG response is limited to the surfaces.

5.3 SHG from InSe thin films

In this section, we outline the results reported in **Publication III**. The characterization of the nonlinear response of InSe films was carried out using a method almost identical to the one used for MCM films. Thus, the analysis follows closely to the analysis presented in Section 5.1. Preliminary measurements included ellipsometry for the determination of refractive indices and preliminary nonlinear polarization experiments to verify in-plane isotropy of the films.

The ellipsometric measurements revealed that the InSe films exhibit significant absorption at the SHG wavelength, which can be represented with a complex refractive index. The obtained refractive indices were $n = 2.63$ and $\underline{n} = \underline{n}' + i\underline{n}''$, with $\underline{n}' = 3.02$ and $\underline{n}'' = 0.28$ for the fundamental and SHG frequencies, respectively.

Due to the real parts of the refractive indices being extremely high, the propagation angles within the film remain relatively small even for large angles of incidence. As a result, the sines of the propagation angles are also small. The contribution from $\chi^{(2)}_{zzz}$ depends on three sine factors (see Eq. 5.1), and can thus be neglected. As a result, following the reasoning of Section 5.1, the only experimentally separable SHG component is $A_{zx} = 2\chi^{(2)}_{xxz} + \chi^{(2)}_{zxx}$. Once more, the off-diagonal SHG susceptibility components can be estimated by assuming Kleinman symmetry as $\chi^{(2)}_{\text{MCM},xxz} = \chi^{(2)}_{\text{MCM},zxx} = A_{zx}/3$.

The Maker-fringe measurements were carried out for three InSe thin films of 40 nm, 100 nm and 190 nm thickness and the results are shown in (Fig. 5.3). As stated above, the analysis follows closely to what was used for MCM films. Here, we neglect phase-mismatched beams and consider only the forward phase-matched SHG (Φ_{---}), but we do account for reflections by including etalon coefficients $(C^p)^2$ and $\underline{C}^p$ at fundamental and SHG frequency, respectively. We also account for absorption by rewriting the z component of the wave vector at SHG frequency as $\underline{w} \to \underline{w}' = \underline{w} + i\alpha$, with $\alpha = (\underline{\omega n}'')/(c\cos\underline{\theta})$. Now, the SHG fields from InSe and glass can be written as

$$\underline{E}^p_{\text{InSe}} = \frac{\underline{\omega}^2 \underline{t}^p_{31}(t^p_{12})^2}{c^2}\frac{\underline{t}^p_{32}}{\underline{w}'_{\text{InSe}}}(C^p)^2\underline{C}^p\Phi_{---}\chi^{(2)}_{\text{InSe}}\mathrm{e}^{i\underline{w}_{\text{glass}}D_{\text{glass}}}(E^p_0)^2 \tag{5.16}$$

and

$$\underline{E}^p_{\text{glass}} = \frac{\underline{\omega}^2 \underline{t}^p_{31}(t^p_{12})^2}{c^2}\frac{(t^p_{32})^2}{\underline{w}_{\text{glass}}}(C^p)^2\chi^{(2)}_{\text{glass}}\mathrm{e}^{2iw_{\text{glass}}D_{\text{glass}}}(E^p_0)^2, \tag{5.17}$$

with $\chi^{(2)}_{\text{InSe}}$ containing only the A_{zx} term, $\chi^{(2)}_{\text{glass}}$ term being given by Eq. (5.1), and the total SHG irradiance given by Eq. (5.2). The SHG components obtained from the fitting process for the three samples are $A_{zx} = 2.9 \pm 0.4$ pm/V for 40 nm, $A_{zx} = 4.0 \pm 0.5$ pm/V for 100 nm, $A_{zx} = 4.1 \pm 0.5$ pm/V for 190 nm. We believe that the disagreement of the SHG component value obtained for the 40 nm thick film with the ones obtained for the 100 nm and 190 nm films is due to the neglect of the phase-mismatched SHG. While this contribution is generally relatively small compared to the forward generated SHG, for a sample as thin as 40 nm its contribution may play a larger role. Thus, we believe that the strong agreement between the values obtained for the 100 nm and 190 nm films indicates that those values better represent reality.

To summarize, we performed nonlinear Maker-fringe characterization for InSe thin films. The obtained value for the dominant SHG component was of the order of

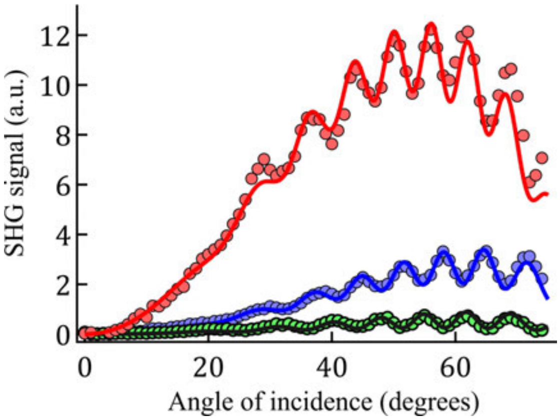

Figure 5.3: Results of the Maker-fringe experiment on InSe thin films of 40 nm (green), 100 nm (blue) and 190 nm (red) thicknesses. Markers denote the measurement points and the lines denote fitting curves. The figure is based on the results of **Publication III**.

4 pm/V, a value that is of the same order with many nonlinear crystals [6]. Although the third-order nonlinearity is common in chalcogenide glasses [111, 128], second-order effects being forbidden under centrosymmetry are much less common. As such, amorphous InSe, especially considering the cost-effectiveness of the fabrication, could well be an interesting material for photonic applications.

5.4 Tuning SHG from SiN by material composition

In this section, we outline the results reported in **Publication IV**. The nonlinear characterization of SiN thin films was carried out using quartz referenced polarization controlled experiment as described in Section 4.4. Five thin films, labeled S10, S20, S30, S35 and S40, of different material composition were studied. The symmetry of the samples was tested with preliminary nonlinear polarization mapping that indicated a $C_{\infty v}$ symmetry, as expected [71]. The refractive indices at the fundamental and SHG frequencies as well as exact thicknesses were determined using ellipsometry for all five samples. The ellipsometric results are shown in Table 5.3.

The results of the polarization controlled experiment for the different polarization combinations of the initial excitation beam and the detected SHG beam are shown in (Fig. 5.4). The results were analysed by using Eq. (4.2) in conjunction with Eqs. (3.14 and 3.41). As a result, the relationship between the polarization signa-

Table 5.3: Results from the ellipsometric measurements for SiN films. For each film, thickness and refractive indices both at fundamental and SHG frequency were determined.

Sample	D (nm)	n	$\underline{n}$
S10	662	$2.174 + 0.002i$	$2.354 + 0.022i$
S20	604	$2.005 + 0.000i$	$2.099 + 0.007i$
S30	537	$1.945 + 0.000i$	$1.989 + 0.002i$
S40	500	$1.969 + 0.000i$	$2.027 + 0.002i$
S50	505	$1.902 + 0.000i$	$1.951 + 0.001i$

tures and the nonvanishing SHG tensor components was found to be

$$\begin{bmatrix} f^{p,p,p} \\ f^{p,s,s} \\ f^{p,p,s} + f^{p,s,p} \\ f^{s,p,p} \\ f^{s,s,s} \\ f^{s,p,s} + f^{s,s,p} \end{bmatrix} = \begin{bmatrix} u_{11} & u_{12} & u_{13} & u_{14} & u_{15} & u_{16} & u_{17} \\ u_{21} & u_{22} & u_{23} & u_{24} & u_{25} & u_{26} & u_{27} \\ u_{31} & u_{32} & u_{33} & u_{34} & u_{35} & u_{36} & u_{37} \\ u_{41} & u_{42} & u_{43} & u_{44} & u_{45} & u_{46} & u_{47} \\ u_{51} & u_{52} & u_{53} & u_{54} & u_{55} & u_{56} & u_{57} \\ u_{61} & u_{62} & u_{63} & u_{64} & u_{65} & u_{66} & u_{67} \end{bmatrix} \begin{bmatrix} \chi^{(2)}_{xxz} \\ \chi^{(2)}_{xzx} \\ \chi^{(2)}_{yyz} \\ \chi^{(2)}_{yzy} \\ \chi^{(2)}_{zxx} \\ \chi^{(2)}_{zyy} \\ \chi^{(2)}_{zzz} \end{bmatrix}, \tag{5.18}$$

with

$$u_{\xi\tau} = \mathrm{e}^{i\underline{w}D} \frac{\underline{\omega}^2}{2c^2\underline{w}} \underline{t}^{\xi}_{23} \sum_{\phi\beta\gamma} \underline{L}_{\xi,\tau,\phi} \chi^{(2)}_{\tau} \Phi_{\phi\beta\gamma} L_{\xi,\tau,\beta} L_{\xi,\tau,\gamma} \underline{K}^{\xi}_{\phi} K^{\tau}_{\beta} K^{\tau}_{\gamma}, \tag{5.19}$$

where ξ and τ are the indices of permutations of $\zeta, \eta, \kappa \in \{p, s\}$ and permutations of $i, j, k \in \{x, y, z\}$, i.e., indices of the vectorizations $\mathbf{f}$ and $\boldsymbol{\chi}^{(2)}_V$ in Eq. (4.2), respectively. The particular choice of this indexing is arbitrary; for example, our choice in Eq. (5.18) has $\xi = 2 \leftrightarrow (p, s, s)$ and $\tau = 3 \leftrightarrow (y, y, z)$, since u_{23} describes the relationship between $f^{p,s,s}$ and $\chi^{(2)}_{yyz}$.

By examining Eq. (5.19) and combining the non-independent SHG tensor components, Eq. (5.18) can be written as

$$\begin{bmatrix} f^{p,p,p} \\ f^{p,s,s} \\ f^{s,s,p} + f^{s,p,s} \end{bmatrix} = \begin{bmatrix} m'_{11} & m'_{12} & m'_{13} \\ 0 & m'_{22} & 0 \\ m'_{31} & 0 & 0 \end{bmatrix} \begin{bmatrix} \chi^{(2)}_{xxz} \\ \chi^{(2)}_{zxx} \\ \chi^{(2)}_{zzz} \end{bmatrix}, \tag{5.20}$$

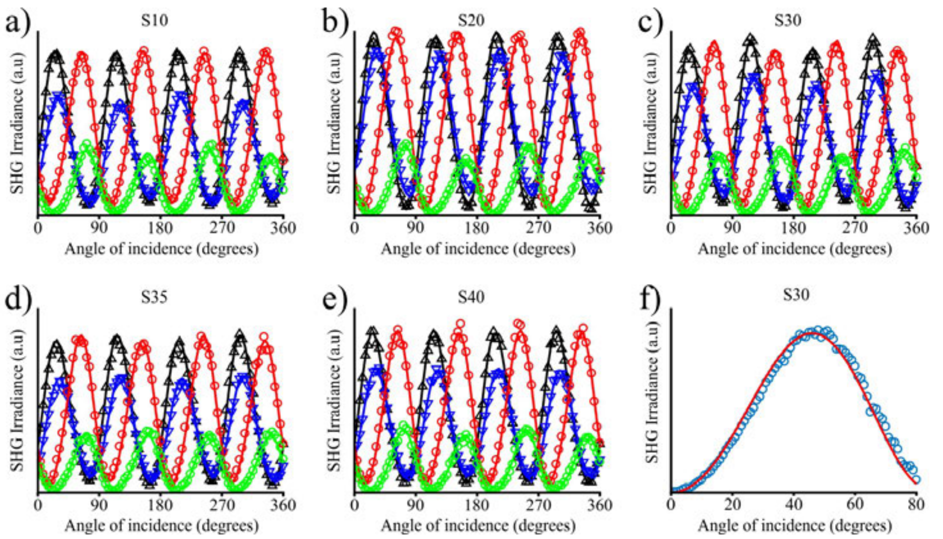

Figure 5.4: a)-e) The results from the polarization controlled measurements for samples a) S10, b) S20, c) S30, d) S35 and e) S40. The polarization combinations of the initial excitation beam and the detected SHG beam are: Black - $(\hat{\mathbf{p}} + \hat{\mathbf{s}})/\sqrt{2}$ in, $\underline{\hat{\mathbf{p}}}$ out; Blue - $(\hat{\mathbf{p}}+\hat{\mathbf{s}})/\sqrt{2}$ in, $(\underline{\hat{\mathbf{p}}}+\underline{\hat{\mathbf{s}}})/\sqrt{2}$ out; Red - $(\hat{\mathbf{p}}-\hat{\mathbf{s}})/\sqrt{2}$ in, $\underline{\hat{\mathbf{p}}}$ out; Green: $(\hat{\mathbf{p}}-\hat{\mathbf{s}})/\sqrt{2}$ in, $(\underline{\hat{\mathbf{p}}}+\underline{\hat{\mathbf{s}}})/\sqrt{2}$ out. f) An example of the calibration measurement of sample S30, which was subsequently compared to SHG from quartz. The figure is based on the results of **Publication IV**.

with

$$u'_{11} = u_{11} + u_{12} \tag{5.21}$$

$$u'_{12} = u_{15} \tag{5.22}$$

$$u'_{13} = u_{17} \tag{5.23}$$

$$u'_{22} = u_{26} \tag{5.24}$$

$$u'_{31} = u_{33} + u_{34}, \tag{5.25}$$

where the matrix elements can be calculated using Eq. (5.19) and the remaining polarization signatures can be uniquely solved with our measurement scheme as discussed in Section 4.4. In order to obtain the SHG tensor structure of SiN, the four polarization controlled measurements can be fitted simultaneously to the relative tensor components and a scaling factor using the above analysis.

For the calibration with respect to quartz, the p polarized SHG arising from s polarized excitation was measured with varying angle of incidence. Only $\chi^{(2)}_{zxx}$ contributes to the generated SHG, as governed by m'_{22}, and the SHG field can be written as

$$\underline{E}^p_{\mathrm{SiN}} = \underline{t}^p_{31} u_{26} (E^s_0)^2, \tag{5.26}$$

which can then be compared to SHG from quartz. Using Eq. (3.36) with perpendicular incidence, polarizations of the excitation beam and the detected SHG beam being parallel to the X axis of the quartz, neglecting reflections and maximizing the phase-matching ($\Phi_{---} = 2/(\underline{w} - 2w)$), the SHG from quartz is given by

$$\underline{E}^p_{\mathrm{Q}} = \frac{\underline{t}^p_{21}(t^p_{12})^2}{\underline{n}_{\mathrm{Q}}(\underline{n}_{\mathrm{Q}} - 2n_{\mathrm{Q}})} \chi^{(2)}_{\mathrm{Q},XXX} (E^p_0)^2. \tag{5.27}$$

The absolute value of $\chi^{(2)}_{zxx}$ can now be obtained with respect to the known SHG susceptibility of quartz $\chi^{(2)}_{\mathrm{Q},XXX} = 0.80$ pm/V [129]. The neglect of reflections for quartz measurement is justified by the thickness and wedged shape of the crystal, making the assumption of infinite reflections unphysical. The SHG susceptibility tensor components obtained with the above analysis in conjunction with the polarization controlled experiment are shown in Table 5.4.

Table 5.4: Results from the nonlinear measurements for SiN films. For each film, the SHG tensor structure was determined by a polarization controlled experiment and the absolute SHG tensor values were calibrated by the quartz reference experiment.

Sample	$\chi^{(2)}_{xxz}$ (pm/V)	$\chi^{(2)}_{zxx}$ (pm/V)	$\chi^{(2)}_{zzz}$ (pm/V)
S10	1.60	1.40	5.10
S20	0.87	0.72	1.70
S30	0.40	0.34	1.10
S40	0.20	0.21	0.66
S50	0.23	0.22	0.80

In conclusion, we conducted a full tensorial characterization of SiN thin films with varying composition. The SHG response was found to increase by as much as 6-fold with increasing silicon content. The highest SHG susceptibility component of $\chi^{(2)}_{zzz} = 5.10$ pm/V is once again comparable to well-known nonlinear materials, highlighting the potential applicability of SiN especially considering its CMOS compatibility. In addition, the PECVD method was found to produce extremely high-quality samples consistenty, which is useful from the characterization perspective. To answer the question about the microscopic origin of the bulk nonlinearity, proposed theories including intrinsic strain introduced in the fabrication process, presence of static fields and formation of small nanocrystals could be further studied for example by studying the effects of external strain on the SHG response, by an external application of a static field on the film or by diffraction techniques, respectively.

5.5 Non-resonant enhancement of SHG from metal-dielectric composites

In this section, we outline the results reported in **Publication V**. The nonlinear responses from the gold nanoisland films coated with TiO_2 were estimated using a substrate-referenced Maker-fringe experiment. The purpose of this experiment was to study the dependence of the local-field enhancement of the nonlinearity on the coating thickness. To support our analysis, absorption spectra were measured using a spectrophotometer.

The absorption spectra and results from Maker-fringe measurements are shown in (Fig. 5.5a) and (Fig. 5.5b), respectively. The relative SHG signals from the coated films were estimated from the visibility of the fringes using the scalar approximation of Eq. (4.1) and by assuming that one of the sources, e.g., the back surface of the substrate, is common for all samples. The resulting relative SHG signal values are shown in (Fig. 5.5c).

To analyze the results, the local field factors describing the relative enhancement of the electric field were calculated using a numerical model for a truncated nanosphere coated by TiO_2. The details of the modeling are reported in Refs. [130–132]. These local field factors can be connected to the enhancement of SHG as [133]

$$I_{\mathrm{SHG}} =\propto \underline{J} J^2, \tag{5.28}$$

where J and $\underline{J}$ are the local field factors at the fundamental and SHG frequencies, respectively. The SHG enhancement predicted by the model is shown in (Fig. 5.5d) and the individual local field factors at the fundamental and SHG frequencies are shown in the inset of (Fig. 5.5d). We note that while the thickness dependence is well explained by the model, the absolute magnitude of the enhancement predicted by the model differed from the observed enhancement. We believe that this is mostly due to the size distribution of the nanoparticles.

To conclude, we studied SHG response of gold nanoisland films coated with various thicknesses of TiO_2 using a Maker-fringe experiment under the scalar approxima-

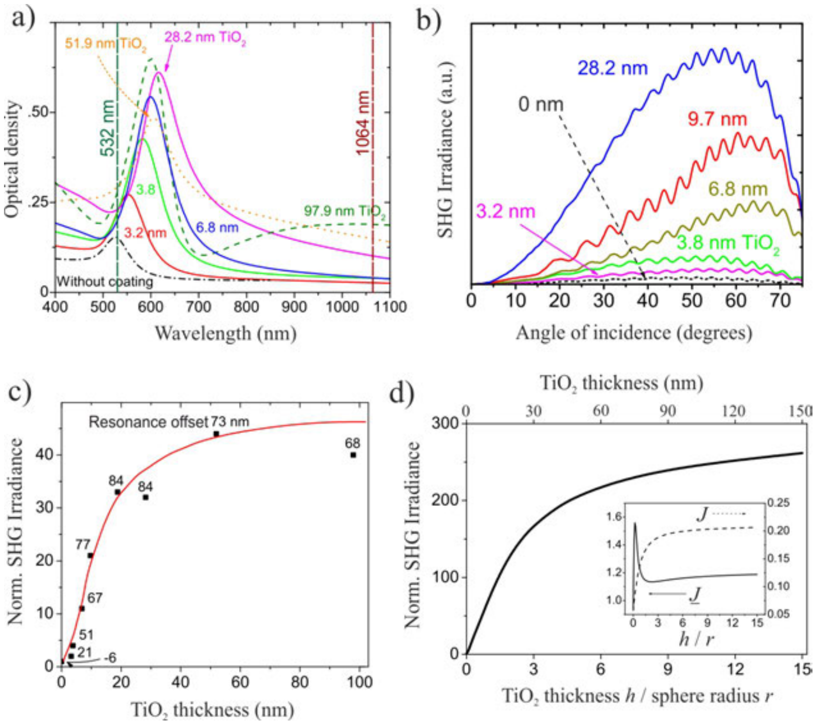

Figure 5.5: a) Absorption spectra of gold nanoisland films coated with different thicknesses of TiO_2. b) Maker-fringe measurement results for the said films. c) Estimated SHG signal levels from the said films. d) Numerically calculated total local field enhancement for said films. Inset: Numerically calculated local-field factors at the fundamental and SHG frequencies. The figure is based on the results of **Publication V**.

tion. Firstly, we showed that coating of nanoparticles affects the absorption spectra depending on the coating thickness. Secondly, we showed both experimentally and numerically that despite the detuning of the resonance with respect to the SHG frequency and thus weakening of the local-field factor at SHG frequency, the enhancement of the local-field factor at fundamental frequency can dominate the total contribution to SHG. To our understanding, such non-resonant enhancement has not been reported previously outside our research and is not limited to this context, possibly opening new ways to optimize nanostructures.

6. CONCLUSIONS

In this Thesis, we developed a thorough analytical model to treat second-harmonic generation from material systems of sub-wavelength thickness both for the case of a single excitation beam and for the case of two non-collinear excitation beams. The model was successfully applied to various traditional methods in the characterization of several potential nonlinear materials: Multilayer composite films, silicon nitride, indium selenide and metal-dielectric composites.

This work was motivated by the ongoing search for novel nonlinear materials for different optical applications. Indeed, many of the applications in, for example, the field of integrated photonics rely on nonlinear phenomena. Many of these phenomena are elusive by nature, few more so than second-harmonic generation, and thus potential materials are few and far in between. With the ever-growing interest towards the miniaturization of optical devices driven by the advances in nanophotonics, the need for expanding the range of applicable nonlinear materials has never been more compelling.

In pursuit of our goal, we demonstrated the potential of silicon nitride and indium selenide as novel second-order nonlinear materials with a second-harmonic response of the order comparable to traditional nonlinear crystals. In addition, the flexibility of the physical parameters of indium selenide allows for further optimization and the CMOS compatibility of silicon nitride is highly advantageous with the material needs of nanophotonics in mind. Our results also show that multilayered composite materials consisting of numerous extremely thin centrosymmetric dielectric layers can circumvent the non-centrosymmetry requirement of second-harmonic generation effectively and exhibit competitive second-harmonic responses.

Lastly, methods to further improve existing strong second-harmonic response were explored. We reported a six-fold increase in the second-harmonic susceptibility of silicon nitride by tuning the material composition via the fabrication process, as well as a 40-fold enhancement in the second-harmonic response of gold nanoparticle films coated with titanium dioxide by tuning the coating thickness.

In addition to its utility in the analysis of experimental results, the derivation of the analytical model itself works towards our objectives. The general nature of the model ensures that it can be used for the treatment of second-harmonic generation from any thin layer, as evidenced by its wide usage in the various experimental schemes of this work. The main advantage of the model compared to the common approaches is the full inclusion of reflections for the cases of single- and two-beam excitations in thin layers in conjunction with the aforementioned generality. Reflections can often be and even more often are neglected for thick systems due to the tedious calculus associated with their inclusion. However, for thin systems, it is absolutely paramount that they are accounted for as the failure to do so will result in both quantitative and qualitative errors, as demonstrated for the separation of multipolar SHG in this work. In addition, great attention was given to writing the model in a compact form with parameters clearly associated with physical phenomena. Particularly, the model explicitly addresses the relationship between the experimental polarization signatures and the SHG susceptibility tensor, allowing for a specific design of experiments, analysis of any kind of experiment as well as optimization of SHG by the geometrical design for thin systems. Thus, we believe that our theoretical work is invaluable for any researcher attempting to treat second-harmonic generation process in thin layers.

Despite the results of this Thesis, no work is ever complete. Besides the obvious trials for new materials, continuation of this work might involve a more thorough nonlinear characterization of multilayer structures and gold-titanium dioxide composites, broadening the experimental methodology and further expansion of the analytical model. Nonlinear materials transparent in the ultraviolet region such as certain plastics would be especially interesting due to most materials being opaque for ultraviolet light.

The characterization of multilayer structures and gold-titanium dioxide composites could be expanded by conducting a full polarization-controlled experiment to complement the current results. Such an experiment could address all of the susceptibility tensor components and improve the accuracy of the results. This is especially true for the gold-titanium dioxide composites given the simplicity of their analysis. However, great care should be taken to account for the non-negligible SHG from the back surface of the substrate as it is difficult to account for this using only a polarization-controlled scheme. A potential solution would be to analyse both a Maker-fringe experiment and a polarization-controlled experiment simultaneously. An alternative would be to fabricate thicker samples that produce more SHG so that the SHG from the substrate would become negligible.

The main ways to improve the experimental methodology would be to utilize a range of excitation frequencies for the nonlinear characterization or to introduce ways to control several parameters simultaneously in the experiment. The former is far more ambitious, as it requires a tunable source, achromatic optics and a detector capable of detecting a sufficiently wide spectrum of SHG with high sensitivity. However, the benefits of studying the spectral behaviour of the nonlinear susceptibility would provide great insights on the material nonlinearity and its origins. The latter option of introducing simultaneous control is considerably easier to implement as, besides some minor practical challenges, a modest financial investment and an updated automatization algorithm are all that are required. The main benefit aside from the convenience of the researcher is that the simultaneous control of the polarizations and the angle of incidence would allow for a more reliable joint Maker-fringe/polarization-controlled experiments.

Lastly, the analytical model could be further expanded in a variety of ways. Firstly, the full description of the total multipolar SHG could be derived as opposed to the signature-of-presence -approach used in this work. The derivation of the said expressions would be a straightforward but tedious process, perhaps one suitable for a M.Sc. thesis project. Secondly, the model could be expanded to systems of multiple thin nonlinear layers. This problem is less straightforward, since the complexity of the treatment of the interplay of reflections grows rapidly if the approach presented in this work is used. A good alternative might be to use some variation of the transfer matrix formalism, although the exact details would have to be assessed. Lastly, the model could be expanded to higher-order nonlinear effects such as third-harmonic generation. Once more, this should be a relatively straightforward task given the obvious analogies between second- and third-harmonic generation with one of the greatest challenges possibly being running out of letters to denote the indices present in the formulae.

REFERENCES

[1] S. Clemmen, A. Hermans, E. Solano, J. Dendooven, K. Koskinen, M. Kauranen, E. Brainis, C. Detavernier, and R. Baets, “Atomic layer deposited second-order nonlinear optical metamaterial for back-end integration with CMOS-compatible nanophotonic circuitry,” Opt. Lett. **40**, 5371–5374 (2015).

[2] K. Koskinen, R. Czaplicki, T. Kaplas, and M. Kauranen, “Recognition of multipolar second-order nonlinearities in thin-film samples,” Opt. Express **24**, 4972–4978 (2016).

[3] K. Koskinen, A. Slablab, S. Divya, R. Czaplicki, S. Chervinskii, M. Kailasnath, P. Radhakrishnan, and M. Kauranen, “Bulk second-harmonic generation from thermally evaporated indium selenide thin films,” Opt. Lett. **42**, 1076–1079 (2017).

[4] K. Koskinen, R. Czaplicki, A. Slablab, T. Ning, A. Hermans, B. Kuyken, V. Mittal, G. S. Murugan, T. Niemi, R. Baets, and M. Kauranen, “Enhancement of bulk second-harmonic generation from silicon nitride films by material composition,” Opt. Lett. **42**, 5030–5033 (2017).

[5] S. Chervinskii, K. Koskinen, S. Scherbak, M. Kauranen, and A. Lipovskii, “Nonresonant local fields enhance second-harmonic generation from metal nanoislands with dielectric cover,” Phys. Rev. Lett. **120**, 113902 (2018).

[6] R. W. Boyd, *Nonlinear Optics* (Academic Press, San Diego, 2008), 3rd ed.

[7] A. L. Schawlow and C. H. Townes, “Infrared and optical masers,” Physical Review **112**, 1940 (1958).

[8] P. A. Franken, A. E. Hill, C. W. Peters, and G. Weinreich, “Generation of optical harmonics,” Physical Review Letters **7**, 118–119 (1961).

[9] R. W. Terhune, P. D. Maker, and C. M. Savage, “Optical harmonic generation in calcite,” Physical Review Letters **8**, 404 (1962).

[10] B. Lax, J. G. Mavroides, and D. F. Edwards, “Nonlinear interband and plasma effects in solids,” Physical Review Letters **8**, 166 (1962).

[11] J. Ducuing and N. Bloembergen, "Observation of reflected light harmonics at the boundary of piezoelectric crystals," Physical Review Letters **10**, 474 (1963).

[12] F. Brown, R. E. Parks, and A. M. Sleeper, "Nonlinear optical reflection from a metallic boundary," Physical Review Letters **14**, 1029 (1965).

[13] N. Bloembergen, R. K. Chang, and C. Lee, "Second-harmonic generation of light in reflection from media with inversion symmetry," Physical Review Letters **16**, 986 (1966).

[14] C. C. Wang and A. N. Duminski, "Second-harmonic generation of light at the boundary of alkali halides and glasses," Physical Review Letters **20**, 668 (1968).

[15] N. I. Adams and P. B. Schoefer, "Continuous optical sum frequency generation," Proceedings of the IEEE **51**, 1366–1367 (1963).

[16] C. C. Wang and G. W. Racette, "Measurement of parametric gain accompanying optical difference frequency generation," Applied Physics Letters **6**, 169–171 (1965).

[17] J. A. Armstrong, N. Bloembergen, J. Ducuing, and P. S. Pershan, "Interactions between light waves in a nonlinear dielectric," Physical Review **127**, 1918–1939 (1962).

[18] Y. Shen, *The Principles of Nonlinear Optics*, ISBN: 978-0-471-43080-3 (Wiley-Interscience, 1984).

[19] G. B. Arfken, H. J. Weber, and F. E. Harris, *Mathematical Methods For Physicists International Student Edition* (Academic Press, 2005).

[20] G. D. Boyd, R. C. Miller, K. Nassau, W. L. Bond, and A. Savage, "LiNbO3: an efficient phase matchable nonlinear optical material," Applied Physics Letters **5**, 234–236 (1964).

[21] R. L. Byer, H. Kildal, and R. S. Feigelson, "CdGeAs2 – a new nonlinear crystal phasematchable at 10.6 μm," Applied Physics Letters **19**, 237–240 (1971).

[22] R. C. Miller, "Optical second harmonic generation in piezoelectric crystals," Applied Physics Letters **5**, 17–19 (1964).

[23] J. L. Oudar and R. Hierle, "An efficient organic crystal for nonlinear optics: methyl-(2, 4-dinitrophenyl)-aminopropanoate," Journal of Applied Physics **48**, 2699–2704 (1977).

[24] B. F. Levine, C. G. Bethea, C. D. Thurmond, R. T. Lynch, and J. L. Bernstein, "An organic crystal with an exceptionally large optical second-harmonic coefficient: 2-methyl-4-nitroaniline," Journal of Applied Physics **50**, 2523–2527 (1979).

[25] J. Zyss, D. S. Chemla, and J. F. Nicoud, "Demonstration of efficient nonlinear optical crystals with vanishing molecular dipole moment: Second-harmonic generation in 3-methyl-4-nitropyridine-1-oxide," The Journal of Chemical Physics **74**, 4800–4811 (1981).

[26] M. Kauranen, T. Verbiest, J. Maki, and A. Persoons, "Second-harmonic generation from chiral surfaces," The Journal of Chemical Physics **101**, 8193–8199 (1994).

[27] Y. R. Shen, "Surface properties probed by second-harmonic and sum-frequency generation," Nature **337**, 519–525 (1989).

[28] R. M. Corn and D. A. Higgins, "Optical second harmonic generation as a probe of surface chemistry," Chemical Reviews **94**, 107–125 (1994).

[29] K. L. Sly, S.-W. Mok, and J. C. Conboy, "Second harmonic correlation spectroscopy: a method for determining surface binding kinetics and thermodynamics," Analytical Chemistry **85**, 8429–8435 (2013).

[30] K. D. Singer, J. E. Sohn, and S. J. Lalama, "Second harmonic generation in poled polymer films," Applied Physics Letters **49**, 248–250 (1986).

[31] W. Margulis and U. Österberg, "Second-harmonic generation in optical glass fibers," Journal of the Optical Society of America B **5**, 312–316 (1988).

[32] R. A. Myers, N. Mukherjee, and S. R. J. Brueck, "Large second-order nonlinearity in poled fused silica," Optics Letters **16**, 1732–1734 (1991).

[33] C. Fiorini, F. Charra, J.-M. Nunzi, and P. Raimond, "Quasi-permanent all-optical encoding of noncentrosymmetry in azo-dye polymers," Journal of the Optical Society of America B **14**, 1984–2003 (1997).

[34] F. Timpu, A. Sergeyev, N. R. Hendricks, and R. Grange, “Second-harmonic enhancement with mie resonances in perovskite nanoparticles,” ACS Photonics **4**, 76–84 (2017).

[35] S. Liu, M. B. Sinclair, S. Saravi, G. A. Keeler, Y. Yang, J. Reno, G. M. Peake, F. Setzpfandt, I. Staude, T. Pertsch *et al.*, “Resonantly enhanced second-harmonic generation using iii–v semiconductor all-dielectric metasurfaces,” Nano letters **16**, 5426–5432 (2016).

[36] R. S. Jacobsen, K. N. Andersen, P. I. Borel, J. Fage-Pedersen, L. H. Frandsen, O. Hansen, M. Kristensen, A. V. Lavrinenko, G. Moulin, H. Ou, C. Peucheret, B. Zsigri, and A. Bjarklev, “Strained silicon as a new electro-optic material,” Nature **441**, 199 EP – (2006).

[37] B. Chmielak, M. Waldow, C. Matheisen, C. Ripperda, J. Bolten, T. Wahlbrink, M. Nagel, F. Merget, and H. Kurz, “Pockels effect based fully integrated, strained silicon electro-optic modulator,” Optics Express **19**, 17212–17219 (2011).

[38] M. Cazzanelli, F. Bianco, E. Borga, G. Pucker, M. Ghulinyan, E. Degoli, E. Luppi, V. Veniard, S. Ossicini, D. Modotto, S. Wabnitz, R. Pierobon, and L. Pavesi, “Second-harmonic generation in silicon waveguides strained by silicon nitride,” Nature Materials **11**, 148–154 (2012).

[39] I. R. Girling, S. R. Jethwa, R. T. Stewart, J. D. Earls, G. H. Cross, N. A. Cade, P. V. Kolinsky, R. J. Jones, and I. R. Peterson, “Second-order non-linear optical effects in Langmuir-Blodgett films,” Thin Solid Films **160**, 355–362 (1988).

[40] L. Alloatti, C. Kieninger, A. Froelich, M. Lauermann, T. Frenzel, K. Köhnle, W. Freude, J. Leuthold, M. Wegener, and C. Koos, “Second-order nonlinear optical metamaterials: ABC-type nanolaminates,” Applied Physics Letters **107**, 121903 (2015).

[41] M. Zdanowicz, J. Harra, J. M. Makela, E. Heinonen, T. Ning, M. Kauranen, and G. Genty, “Second-harmonic response of multilayer nanocomposites of silver-decorated nanoparticles and silica,” Scientific Reports **4**, 5745 (2014).

[42] I. Russier-Antoine, E. Benichou, G. Bachelier, C. Jonin, and P. Brevet, “Multipolar contributions of the second harmonic generation from silver and gold nanoparticles,” The Journal of Physical Chemistry C **111**, 9044–9048 (2007).

[43] A. E.-J. Lim, J. Song, Q. Fang, C. Li, X. Tu, N. Duan, K. K. Chen, R. P.-C. Tern, and T.-Y. Liow, "Review of silicon photonics foundry efforts," IEEE Journal of Selected Topics in Quantum Electronics **20**, 405–416 (2014).

[44] M. S. Rill, C. Plet, M. Thiel, I. Staude, G. Von Freymann, S. Linden, and M. Wegener, "Photonic metamaterials by direct laser writing and silver chemical vapour deposition," Nature Materials **7**, 543 (2008).

[45] I. Staude and J. Schilling, "Metamaterial-inspired silicon nanophotonics," Nature Photonics **11**, 274 (2017).

[46] A. Alduino and M. Paniccia, "Interconnects: Wiring electronics with light," Nature Photonics **1**, 153 (2007).

[47] D. A. Miller, "Optical interconnects to silicon," IEEE Journal of Selected Topics in Quantum Electronics **6**, 1312–1317 (2000).

[48] B. G. Lee, X. Chen, A. Biberman, X. Liu, I.-W. Hsieh, C.-Y. Chou, J. I. Dadap, F. Xia, W. M. Green, L. Sekaric *et al.*, "Ultrahigh-bandwidth silicon photonic nanowire waveguides for on-chip networks," IEEE Photonics Technology Letters **20**, 398–400 (2008).

[49] G. Lifante, *Integrated photonics: fundamentals* (John Wiley & Sons, 2003).

[50] C. R. Pollock and M. Lipson, *Integrated photonics*, vol. 20 (Springer, 2003).

[51] R. L. Espinola, J. I. Dadap, R. M. Osgood, S. J. McNab, and Y. A. Vlasov, "Raman amplification in ultrasmall silicon-on-insulator wire waveguides," Optics Express **12**, 3713–3718 (2004).

[52] R. M. Osgood, N. C. Panoiu, J. I. Dadap, X. Liu, X. Chen, I.-W. Hsieh, E. Dulkeith, W. M. J. Green, and Y. A. Vlasov, "Engineering nonlinearities in nanoscale optical systems: physics and applications in dispersion-engineered silicon nanophotonic wires," Advances in Optics and Photonics **1**, 162–235 (2009).

[53] J. S. Levy, A. Gondarenko, M. A. Foster, A. C. Turner-Foster, A. L. Gaeta, and M. Lipson, "CMOS-compatible multiple-wavelength oscillator for on-chip optical interconnects," Nature Photonics **4**, 37–40 (2010).

[54] J. Leuthold, C. Koos, and W. Freude, "Nonlinear silicon photonics," Nature Photonics **4**, 535 (2010).

[55] P. Kultavewuti, “Nonlinear photonics in chip-based structures,” Frontiers in Modern Optics **190**, 171 (2016).

[56] L. Chang, Y. Li, N. Volet, L. Wang, J. Peters, and J. E. Bowers, “Thin film wavelength converters for photonic integrated circuits,” Optica **3**, 531–535 (2016).

[57] P. D. Maker, R. W. Terhune, M. Nisenoff, and C. M. Savage, “Effects of dispersion and focusing on the production of optical harmonics,” Physical Review Letters **8**, 21–22 (1962).

[58] J. Jerphagnon and S. K. Kurtz, “Maker fringes: A detailed comparison of theory and experiment for isotropic and uniaxial crystals,” Journal of Applied Physics **41**, 1667–1681 (1970).

[59] J. Sipe, V. Mizrahi, and G. Stegeman, “Fundamental difficulty in the use of second-harmonic generation as a strictly surface probe,” Physical Review B **35**, 9091–9094 (1987).

[60] W. N. Herman and L. M. Hayden, “Maker fringes revisited: second-harmonic generation from birefringent or absorbing materials,” Journal of the Optical Society of America B **12**, 416–427 (1995).

[61] P. Pershan, “Nonlinear optical properties of solids: Energy considerations,” Physical Review **130**, 919–929 (1963).

[62] E. Adler, “Nonlinear optical frequency polarization in a dielectric,” Physical Review **134**, A728 (1964).

[63] P. Guyot-Sionnest and Y. Shen, “Bulk contribution in surface second-harmonic generation,” Physical Review B **38**, 7985–7989 (1988).

[64] S. Cattaneo and M. Kauranen, “Polarization-based identification of bulk contributions in surface nonlinear optics,” Physical Review B **72**, 033412 (2005).

[65] S. Cattaneo and M. Kauranen, “Bulk versus surface contributions in nonlinear optics of isotropic centrosymmetric media,” Physica Status Solidi (b) **242**, 3007–3011 (2005).

[66] F. Rodriguez, F. Wang, B. Canfield, S. Cattaneo, and M. Kauranen, “Multipolar tensor analysis of second-order nonlinear optical response of surface and bulk of glass,” Optics Express **15**, 8695–8701 (2007).

[67] F. Rodríguez, F. Wang, and M. Kauranen, "Calibration of the second-order nonlinear optical susceptibility of surface and bulk of glass," Optics Express **16**, 8704–8710 (2008).

[68] J. Sipe, "New Green-function formalism for surface optics," The Journal of the Optical Society of America B **4**, 481–498 (1987).

[69] P. Guyot-Sionnest, W. Chen, and Y. Shen, "General considerations on optical second-harmonic generation from surfaces and interfaces," Physical Review B **33**, 8254–8263 (1986).

[70] N. Bloembergen, R. Chang, S. Jha, and C. Lee, "Optical second-harmonic generation in reflection from media with inversion symmetry," Physical Review **174**, 813–822 (1968).

[71] T. Ning, H. Pietarinen, O. Hyvärinen, J. Simonen, G. Genty, and M. Kauranen, "Strong second-harmonic generation in silicon nitride films," Applied Physics Letters **100**, 161902 (2012).

[72] A. Segura, J. Bouvier, M. Andrés, F. Manjón, and V. Munoz, "Strong optical nonlinearities in gallium and indium selenides related to inter-valence-band transitions induced by light pulses," Physical Review B **56**, 4075 (1997).

[73] L. Debbichi, O. Eriksson, and S. Lebègue, "Two-dimensional indium selenides compounds: An ab initio study," The Journal of Physical Chemistry Letters **6**, 3098–3103 (2015).

[74] M. Kauranen and A. V. Zayats, "Nonlinear plasmonics," Nature Photonics **6**, 737 (2012).

[75] J. Maxwell, *A treatise on electricity and magnetism* (Macmillan and Company, London, 1873).

[76] J. D. Jackson, *Classical Electrodynamics*, ISBN: 978-0-471-30932-1 (Wiley, New York, 1975), 2nd ed.

[77] E. Hecht, *Optics* (Addison Wesley, 2002), 4th ed.

[78] A. Perot and C. Fabry, "On the application of interference phenomena to the solution of various problems of spectroscopy and metrology," The Astrophysical Journal **9**, 87 (1899).

[79] D. A. Kleinman, “Nonlinear dielectric polarization in optical media,” Physical Review **126**, 1977 (1962).

[80] R. D. Cowan, *The Theory of Atomic Structure and Spectra* (University of California press, Berkeley, 1981).

[81] P. Guyot-Sionnest and Y. Shen, “Local and nonlocal surface nonlinearities for surface optical second-harmonic generation,” Physical Review B **35**, 4420–4426 (1987).

[82] M. Kauranen, T. Verbiest, and A. Persoons, “Second-order nonlinear optical signatures of surface chirality,” Journal of Modern Optics **45**, 403–424 (1998).

[83] P. Figliozzi, L. Sun, Y. Jiang, N. Matlis, B. Mattern, M. Downer, S. Withrow, C. White, W. Mochan, and B. Mendoza, “Single-beam and enhanced two-beam second-harmonic generation from silicon nanocrystals by use of spatially inhomogeneous femtosecond pulses,” Physical Review Letters **94**, 047401 (2005).

[84] F. J. Rodríguez, F. X. Wang, B. K. Canfield, S. Cattaneo, and M. Kauranen, “Multipolar tensor analysis of second-order nonlinear optical response of surface and bulk of glass,” Optics Express **15**, 8695–8701 (2007).

[85] F. Wang, F. Rodríguez, W. Albers, R. Ahorinta, J. Sipe, and M. Kauranen, “Surface and bulk contributions to the second-order nonlinear optical response of a gold film,” Physical Review B **80**, 233402 (2009).

[86] F. Wang, F. Rodríguez, W. Albers, and M. Kauranen, “Enhancement of bulk-type multipolar second-harmonic generation arising from surface morphology of metals,” New Journal of Physics **12**, 063009 (2010).

[87] S. V. Andersen and K. Pedersen, “Second-harmonic generation from electron beam deposited SiO films,” Optics Express **20**, 13857–13869 (2012).

[88] R. Jing, Y. Guang, Z. Huidan, C. Guorong, K. Tanaka, K. Fujita, S. Murai, and Y. Tsujiie, “Second-harmonic generation in thermally poled chalcohalide glass,” Optics Letters **31**, 3492–3494 (2006).

[89] M. Larciprete, A. Belardini, C. Sibilia, M.-b. Saab, G. Varo, and C. Gergely, “Optical chirality of bacteriorhodopsin films via second harmonic maker’s fringes measurements,” Applied Physics Letters **96**, 221108 (2010).

[90] X. Zhang, J. Yao, W. Yin, Y. Zhu, Y. Wu, and C. Chen, “Determination of the nonlinear optical coefficients of the BaGa4Se7 crystal,” Optics Express **23**, 552–558 (2015).

[91] J. Maki, M. Kauranen, T. Verbiest, and A. Persoons, “Uniqueness of wave-plate measurements in determining the tensor components of second-order surface nonlinearities,” Physical Review B **55**, 5021–5026 (1997).

[92] F. Wang, M. Siltanen, and M. Kauranen, “Uniqueness of determination of second-order nonlinear optical expansion coefficients of thin films,” Physical Review B **76**, 085428 (2007).

[93] J. Maki, M. Kauranen, and A. Persoons, “Surface second-harmonic generation from chiral materials,” Physical Review B **51**, 1425–1434 (1995).

[94] M. Zdanowicz, J. Harra, J. M. Mäkelä, E. Heinonen, T. Ning, M. Kauranen, and G. Genty, “Ordered multilayer silica-metal nanocomposites for second-order nonlinear optics,” Applied Physics Letters **103**, 251907 (2013).

[95] W. Shimizu, S. Nakamura, T. Sato, and Y. Murakami, “Creation of high-refractive-index amorphous titanium oxide thin films from low-fractal-dimension polymeric precursors synthesized by a Sol-Gel technique with a hydrazine monohydrochloride catalyst,” Langmuir **28**, 12245–12255 (2012).

[96] S. K. Kim, S. W. Lee, C. S. Hwang, Y. S. Min, J. Y. Won, and J. Jeong, “Low temperature ($<$ 100 °C) deposition of aluminum oxide thin films by ald with o3 as oxidant,” Journal of The Electrochemical Society **153**, F69 (2006).

[97] D. Beena, K. Lethy, R. Vinodkumar, A. Detty, V. M. Pillai, and V. Ganesan, “Photoluminescence in laser ablated nanostructured indium oxide thin films,” Journal of Alloys and Compounds **489**, 215 – 223 (2010).

[98] A. Khanna, A. Z. Subramanian, M. Häyrinen, S. Selvaraja, P. Verheyen, D. V. Thourhout, S. Honkanen, H. Lipsanen, and R. Baets, “Impact of ald grown passivation layers on silicon nitride based integrated optic devices for very-near-infrared wavelengths,” Optics Express **22**, 5684–5692 (2014).

[99] A. Kitao, K. Imakita, I. Kawamura, and M. Fujii, “An investigation into second harmonic generation by Si–rich SiN x thin films deposited by rf sputtering over a wide range of si concentrations,” Journal of Physics D: Applied Physics **47**, 215101 (2014).

[100] E. F. Pecora, A. Capretti, G. Miano, and L. Dal Negro, “Generation of second harmonic radiation from sub-stoichiometric silicon nitride thin films,” Applied Physics Letters **102**, 141114 (2013).

[101] C. Di Valentin, G. Palma, and G. Pacchioni, “Ab initio study of transition levels for intrinsic defects in silicon nitride,” The Journal of Physical Chemistry C **115**, 561–569 (2011).

[102] M. Ippolito and S. Meloni, “Atomistic structure of amorphous silicon nitride from classical molecular dynamics simulations,” Physical Review B **83**, 165209 (2011).

[103] S. Lettieri, S. Di Finizio, P. Maddalena, V. Ballarini, and F. Giorgis, “Second-harmonic generation in amorphous silicon nitride microcavities,” Applied Physics Letters **81**, 4706–4708 (2002).

[104] S. Minissale, S. Yerci, and L. Dal Negro, “Nonlinear optical properties of low temperature annealed silicon-rich oxide and silicon-rich nitride materials for silicon photonics,” Applied Physics Letters **100**, 021109 (2012).

[105] M. H. Nayfeh, N. Rigakis, and Z. Yamani, “Photoexcitation of si-si surface states in nanocrystallites,” Physical Review B **56**, 2079–2084 (1997).

[106] M. W. Puckett, R. Sharma, H.-H. Lin, M. han Yang, F. Vallini, and Y. Fainman, “Observation of second-harmonic generation in silicon nitride waveguides through bulk nonlinearities,” Optics Express **24**, 16923–16933 (2016).

[107] T. Ning, H. Pietarinen, O. Hyvärinen, R. Kumar, T. Kaplas, M. Kauranen, and G. Genty, “Efficient second-harmonic generation in silicon nitride resonant waveguide gratings,” Optics Letters **37**, 4269–4271 (2012).

[108] I. Sebastian, S. Mathew, V. Nampoori, P. Radhakrishnan, and S. Thomas, “Concentration tuned bandgap and corresponding nonlinear refractive index dispersion in Ga-Ge-Se nanocolloids,” Journal of Applied Physics **114**, 053102 (2013).

[109] T. I. Kosa, R. Rangel-Rojo, E. Hajto, P. J. S. Ewen, A. E. Owen, A. K. Kar, and B. S. Wherrett, “Nonlinear optical properties of silver-doped As2S3,” Journal of Non-Crystalline Solids **164**, 1219–1222 (1993).

[110] J. M. Harbold, F. Ilday, F. W. Wise, J. S. Sanghera, V. Q. Nguyen, L. B. Shaw, and I. D. Aggarwal, "Highly nonlinear As–S–Se glasses for all-optical switching," Optics Letters **27**, 119–121 (2002).

[111] C. Quémard, F. Smektala, V. Couderc, A. Barthelemy, and J. Lucas, "Chalcogenide glasses with high non linear optical properties for telecommunications," Journal of Physics and Chemistry of Solids **62**, 1435–1440 (2001).

[112] K. Shimakawa, A. Kolobov, and S. Elliott, "Photoinduced effects and metastability in amorphous semiconductors and insulators," Advances in Physics **44**, 475–588 (1995).

[113] S. Schwarz, S. Dufferwiel, P. M. Walker, F. Withers, A. A. P. Trichet, M. Sich, F. Li, E. A. Chekhovich, D. N. Borisenko, N. N. Kolesnikov, K. S. Novoselov, M. S. Skolnick, S. J. M, K. D. N, and T. A. I, "Two-dimensional metal–chalcogenide films in tunable optical microcavities," Nano letters **14**, 7003–7008 (2014).

[114] S. R. Tamalampudi, Y.-Y. Lu, R. Kumar U., R. Sankar, C.-D. Liao, K. Moorthy B., C.-H. Cheng, F. C. Chou, and Y.-T. Chen, "High performance and bendable few-layered InSe photodetectors with broad spectral response," Nano Letters **14**, 2800–2806 (2014).

[115] W. Feng, X. Zhou, W. Q. Tian, W. Zheng, and P. Hu, "Performance improvement of multilayer InSe transistors with optimized metal contacts," Physical Chemistry Chemical Physics **17**, 3653–3658 (2015).

[116] J.-Y. Kim, J. Yang, J. H. Yu, W. Baek, C.-H. Lee, H. J. Son, T. Hyeon, and M. J. Ko, "Highly efficient copper–indium–selenide quantum dot solar cells: suppression of carrier recombination by controlled zns overlayers," ACS Nano **9**, 11286–11295 (2015).

[117] R. Tintu, V. P. N. Nampoori, P. Radhakrishnan, and S. Thomas, "Photoinduced changes in optical properties of Ga–Sb–Ge–Se glasses," Optics Communications **284**, 222–225 (2011).

[118] N. Liu, H. Liu, S. Zhu, and H. Giessen, "Stereometamaterials," Nature Photonics **3**, 157 (2009).

[119] V. M. Shalaev, "Optical negative-index metamaterials," Nature Photonics **1**, 41–48 (2007).

[120] H. Husu, J. Mäkitalo, J. Laukkanen, M. Kuittinen, and M. Kauranen, "Particle plasmon resonances in L-shaped gold nanoparticles," Optics Express **18**, 16601–16606 (2010).

[121] M. A. Green and S. Pillai, "Harnessing plasmonics for solar cells," Nature Photonics **6**, 130 (2012).

[122] J. N. Anker, W. P. Hall, O. Lyandres, N. C. Shah, J. Zhao, and R. P. Van Duyne, "Biosensing with plasmonic nanosensors," in "Nanoscience And Technology: A Collection of Reviews from Nature Journals," (World Scientific, 2010), pp. 308–319.

[123] X. Ni, N. K. Emani, A. V. Kildishev, A. Boltasseva, and V. M. Shalaev, "Broadband light bending with plasmonic nanoantennas," Science **335**, 427–427 (2012).

[124] H. Husu, R. Siikanen, J. Mï¿½kitalo, J. Lehtolahti, J. Laukkanen, M. Kuittinen, and M. Kauranen, "Metamaterials with tailored nonlinear optical response," Nano Letters **12**, 673–677 (2012).

[125] R. Czaplicki, H. Husu, R. Siikanen, J. Mäkitalo, M. Kauranen, J. Laukkanen, J. Lehtolahti, and M. Kuittinen, "Enhancement of second-harmonic generation from metal nanoparticles by passive elements," Physical Review Letters **110**, 093902 (2013).

[126] M. Klein, C. Enkrich, M. Wegener, and S. Linden, "Second-harmonic generation from magnetic metamaterials," Science **313**, 502–504 (2006).

[127] S. Cattaneo and M. Kauranen, "Polarization-based identification of bulk contributions in surface nonlinear optics," Physical Review B **72**, 033412 (2005).

[128] T. Kohoutek, S. Mizuno, T. Suzuki, Y. Ohishi, M. Matsumoto, and T. Misumi, "Third-harmonic generation measurement of nonlinear optical susceptibility $\chi(3)$ of Ge-Ga-Sb-S chalcogenide glasses proposed for highly nonlinear photonic fibers," Journal of the Optical Society of America B **28**, 298–305 (2011).

[129] R. W. Boyd, *Nonlinear Optics* (Academic Press, San Diego, 2003), 2nd ed.

[130] S. Scherbak, N. Kapralov, I. Reduto, S. Chervinskii, O. Svirko, and A. Lipovskii, "Tuning plasmonic properties of truncated gold nanospheres by coating," Plasmonics **12**, 1903–1910 (2017).

[131] M. Wind, J. Vlieger, and D. Bedeaux, "The polarizability of a truncated sphere on a substrate I," Physica A: Statistical Mechanics and its Applications **141**, 33 – 57 (1987).

[132] S. A. Scherbak and A. A. Lipovskii, "Understanding the second harmonic generation enhancement and behavior in metal core–dielectric shell nanoparticles," The Journal of Physical Chemistry C (2018).

[133] T. V. Shahbazyan and M. I. Stockman, *Plasmonics: theory and applications* (Springer, 2013).

Publications

Publication I

Atomic layer deposited second-order nonlinear optical metamaterial for back-end integration with CMOS-compatible nanophotonic circuitry

Stéphane Clemmen, Artur Hermans, Eduardo Solano, Jolien Dendooven, Kalle Koskinen, Martti Kauranen, Edouard Brainis, Christophe Detavernier and Roel Baets

Optics Letters **40**, 5371-5374 (2015)
© 2015 Optical Society of America.
Reprinted with permission.

Atomic layer deposited second-order nonlinear optical metamaterial for back-end integration with CMOS-compatible nanophotonic circuitry

Stéphane Clemmen[1,2,†], Artur Hermans[1,2,†], Eduardo Solano[3], Jolien Dendooven[3], Kalle Koskinen[4], Martti Kauranen[4], Edouard Brainis[2,5], Christophe Detavernier[3], Roel Baets[1,2]

1. Photonics Research Group, Department of Information Technology, Ghent University-imec,
Sint-Pietersnieuwstraat 41, 9000 Ghent, Belgium
2. Center for Nano- and Biophotonics (NB-Photonics), Ghent University, Sint-Pietersnieuwstraat 41, 9000 Ghent, Belgium
3. Department of Solid State Sciences, Faculty of Sciences, Ghent University, Krijgslaan 281/S1, 9000 Ghent, Belgium
4. Optics Laboratory, Tampere University of Technology, PO Box 692, FI-33101 Tampere, Finland
5. Physics and Chemistry of Nanostructures Group, Ghent University, Krijgslaan 281/S3, 9000 Ghent, Belgium
† Author e-mail address: sclemmen@intec.ugent.be; these authors contributed equally to the work

Received 21 August 2015; revised 2 October 2015; accepted 3 October 2015; posted 5 October 2015 (Doc. ID 248367); published 11 November 2015

We report the fabrication of artificial unidimensional crystals exhibiting an effective bulk second-order nonlinearity. The crystals are created by cycling atomic layer deposition of three dielectric materials such that the resulting metamaterial is non-centrosymmetric in the direction of the deposition. Characterization of the structures by second-harmonic generation Maker-fringe measurements shows that the main component of their nonlinear susceptibility tensor is about 5 pm/V which is comparable to well-established materials and more than an order of magnitude greater than reported for a similar crystal [L. Alloatti *et al.*, Appl. Phys. Lett. 107, 121903 (2015)]. Our demonstration opens new possibilities for second-order nonlinear effects on CMOS-compatible nanophotonic platforms.

OCIS codes: *(190.4400) Nonlinear optics, materials, (190.4720), Optical nonlinearities of condensed matter, (190.4350) Nonlinear optics at surfaces*

http://dx.doi org

Second-order nonlinear optical response of materials gives rise to useful effects, including nonlinear wave mixing and the Pockels effect, with applications such as light generation in optical parametric oscillators and electro-optic modulation. Some of these applications have been miniaturized using various technologies. More recently, a goal has been to integrate optical functionalities on nanophotonic chips that are compatible with CMOS fabrication, which is the standard in micro/nanoelectronics. As a result, optical parametric oscillators [1,2] and fast modulators [3] have been reported. Since silicon and silicon nitride, which are the two main CMOS-compatible photonics platforms, lack a second-order nonlinearity, those realizations were based on the third-order nonlinearity or carrier effects. This resulted in a modest improvement in terms of energy consumption and efficiency over simpler second-order nonlinear devices widely used in free space nonlinear optics. Therefore, it would be highly desirable to be able to induce a second-order nonlinear response in a material otherwise lacking that property.

To date, common methods to artificially create a second-order nonlinearity include poling in silica glass [4] or polymers [5], strain [6], plasmonic surface enhancement [7], and alternate stacking of organic films [8]. In addition, even materials expected to lack a second-order response may in some cases exhibit a significant response, but the origin remains unknown [9,10]. In any case, the inversion symmetry of the material structure must somehow be broken to induce a second-order nonlinear response.

In this letter, we utilize the symmetry breaking mechanism which was also implemented by Alloatti *et al.* in 2015 [11] to induce a substantial second-order nonlinear response, as described by the second-order susceptibility $\chi^{(2)}$. We deposit very thin layers of three distinct transparent amorphous materials A, B, and C and repeat that structure many times to form a thick layer of a composite ABC material. In such a system, each interface between any two materials breaks the symmetry resulting in an effective bulk $\chi^{(2)}$ for the overall structure. Whereas [11] reported a relatively low second-order response, we demonstrate that such an ABC approach can result in a large $\chi^{(2)}$, comparable to that of well-known second-order materials. Our characterization is based on second-harmonic generation (SHG) Maker-fringe measurements that allow the nonlinearity of the ABC layer to be separated unambiguously from that of the substrate. We verified that the SHG contributions of each of the 3 interfaces A-B, B-C, and C-A do not sum up to 0 as would be expected for an AB system.

It is important to understand that our approach is well suited for integration with existing CMOS-compatible nanophotonics platforms. Indeed, the deposition method, ALD, is conformal, requires low temperature, and has been proven to integrate perfectly with existing nanophotonic circuitry [12]. Moreover, as the symmetry of the ABC structure is broken along its normal, the nonlinearity requires electric field components along the normal direction, which occurs for p-polarized light at non-normal incidence (see figure 1a). This implies that, for the case of widely used planar or rib waveguides, the nonlinearity would be the greatest for a TM-mode such as illustrated in figure 1b.

In the present proof of principle, the three materials were chosen to be (A) TiO_2, (B) Al_2O_3, and (C) In_2O_3. While detailed theories exist to predict second-order nonlinearities of superlattices of crystalline materials [13], we are not aware of such theories existing for stacks of amorphous materials. In choosing our particular materials, we therefore used

Material	Precursor	Growth (nm/cycle)	Bandgap (eV)	Refractive index	# cycles for 0.7 nm layer
TiO_2	TDMAT – Tetrakis (dimethylamido)titanium	0.06	3.4 [15]	2.1 [16]	12
Al_2O_3	TMA - Trimethylaluminium	0.1	8.8 [17]	1.5 – 1.7 [18]	7
In_2O_3	$In(TMHD)_3$– Tris(2,2,6,6-tetramethyl-3,5-heptanedionato) indium(III)	0.01	3.7 [19]	2.2 [19]	70

Table 1: Summary of ALD parameters and optical properties. For the TDMAT and $In(TMHD)_3$ precursors, Ar was used as a carrier gas.

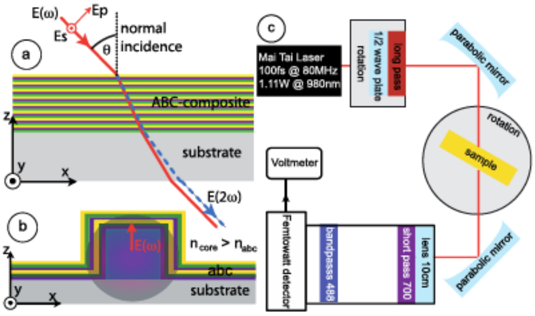

Figure 1: (a) Geometry of the ABC composite and the incidence of either p- or s-polarized light resulting in collinear second-harmonic generation. (b) Possible use of the nonlinearity via the TM-mode of a waveguiding structure (c) Maker-fringe experimental setup for characterization of $\chi^{(2)}$ nonlinearity via second-harmonic generation.

Table 2: Parameters used for the fitting (see body of the text for more details) Left: Refractive indices of the ABC composite measured by ellipsometry at the fundamental and second-harmonic wavelengths for ordinary and extraordinary polarization. Right: refractive index and nonlinearity of the borosilicate glass substrate.

ABC composite	
n_z (980 nm) ordinary	2.02
n_z (490nm) ordinary	2.13
n_x (980 nm) extraordinary	1.92
n_x (490nm) extraordinary	2.06

Borosilicate glass	
n (980 nm)	1.4633
N (490 nm)	1.4766
χ_{xxz}^{glass} (m^2/V)	$11.6 \pm 0.8 \times 10^{-22}$ [27]
χ_{zzz}^{glass} (m^2/V)	$93 \pm 14 \times 10^{-22}$ [27]

the old guideline that the nonlinearity depends on the dielectric contrast between the materials [14] (see table 1). In consequence, the nonlinearities of the A-B and B-A interfaces are equal in magnitude but opposite in sign. By combining the three materials appropriately, however, we expect to obtain a structure where the nonlinearities of the A-B, B-C, and C-A interface have a non-cancelling contribution. Each individual layer is 0.7 nm thick such that the ABC cycle is repeated many times to form thick ABC composite layers on top of 500 µm hick borosilicate glass substrates (Schott BOROFLOAT®33). The thickness of individual layers is an arbitrary compromise between the greatest density of interfaces and the certainty to have a well-defined layer. Several ABC composite crystals were made that differ only by their total thickness of 2.1, 25 and 50 nm which is limited solely by the duration of the deposition process. The deposition process started with the cleaning of the glass with O_2 plasma. The ALD was enhanced by using an oxygen plasma with an RF power of 200 W, a frequency of 13.56 MHz and a pulse duration of 10 s. The deposition was done by alternating pulses of the corresponding metalorganic precursor at a pressure of 6.0×10^{-5} bar, followed by the O_2 plasma pulse at 1.2×10^{-5} bar and a temperature of 120°C, constant throughout the full deposition process. In between each gas pulse the chamber is pumped down to high vacuum. Table 1 shows the precursors and growth-per-cycle for each of the three materials deposited [20-23].

Since the individual layers are much thinner than optical wavelengths, we can consider the multilayer as one homogeneous uniaxial material [24]. The refractive indices of the ABC composite were measured via ellipsometry (see table 2).

The nonlinear characterization was done using the Maker-fringe technique [25] with the setup depicted in figure 1c. The source for fundamental light was a commercial Ti sapphire laser (Mai Tai HP from Spectra-Physics) emitting 100 fs pulses at the fundamental wavelength of 980 nm and a peak power reaching 140 kW. The linear polarization of the laser beam was aligned to p-polarization with a half-wave plate and its spectrum was cleaned to suppress any spurious light at wavelengths below 800 nm. Then, the light is slightly focused on the sample using a parabolic mirror of 5 cm focal length such that the beam size ($1/e^2$) is brought from 1.2 mm to 52 ± 4 microns. The corresponding Rayleigh range is 9 mm thus leaving a relatively large tolerance for the alignment of the sample in the focal plane. After interaction with the sample, the light was collimated and the fundamental wavelength filtered out from the generated second-harmonic light. A lens was placed before the femtowatt detector (Thorlabs PDF10A) so that it can accommodate beam displacements induced by the rotation of the sample. To confirm that the detected signal is SHG and not any fluorescence, we tuned the laser wavelength so that its corresponding second-harmonic wavelength falls out of the bandpass filter and verified that the signal collected vanishes.

The results of our experiment consist of Maker fringes for our samples consisting of a blank substrate, and substrates coated on one side by 2.1, 25, and 50 nm of our ABC composite material. The results are summarized in figures 2 and 3. The curve corresponding to the bare borosilicate glass shows the expected Maker fringes with a visibility limited in part by temporal walk-off occurring between the fundamental beam and the second-harmonic signal generated at the first interface and for the rest due to experimental imperfection leading to slightly unequal intensities at the front and back surfaces. The curve corresponding to 2.1 nm sample shows essentially the same response as the blank substrate thus providing a first indication that the air-ABC interface is not responsible for the increased SHG. The curves corresponding to thicker ABC samples show SHG increasing with thickness and fringes with reduced visibility. The reduced visibility is due to imbalance between the increased responses of the ABC layers and the unchanged response of the uncoated back surface.

To extract a value for the second-order susceptibility from these measurements, we model and fit the experimental curves assuming that SHG occurs at the ABC layer at the front interface and at the glass-air back interface. The SHG depends on the respective components of the second-order nonlinear susceptibility tensor χ_{xxz}^{abc}, χ_{zxx}^{abc}, χ_{zzz}^{abc} of the ABC composite and χ_{xxz}^{glass}, χ_{zxx}^{glass}, χ_{zzz}^{glass} of the glass substrate. The SHG signals can be described by the following equation [26]:

$$E_{total} = E_{front} + E_{back}$$
$$\propto \left[\frac{t_{air,abc}^2 T_{abc,glass} T_{glass,air}}{N_{abc}\cos(\Theta_{abc})} exp\left(i\frac{2L\omega N_{glass}\cos\Theta_{glass}}{c}\right)\chi^{abc} + \frac{t_{air,abc}^2 t_{abc,glass}^2 T_{glass,air}}{N_{glass}\cos(\Theta_{glass})} exp\left(i\frac{2L\omega n_{glass}\cos\theta_{glass}}{c}\right)\chi^{glass}\right]$$

with

$$\begin{aligned}\chi^{abc} = \chi^{abc}_{xxz}\, sin(2\theta_{abc})\, cos(\Theta_{abc}) \\ + \chi^{abc}_{zxx}\, sin(\Theta_{abc})\ cos^2(\theta_{abc}) \\ + \chi^{abc}_{zzz}\, sin^2(\theta_{abc})\, sin(\Theta_{abc})\end{aligned}$$

and

$$\begin{aligned}\chi^{glass} = \chi^{glass}_{xxz}\, sin(2\theta_{glass})\, cos(\Theta_{glass}) \\ + \chi^{glass}_{zxx}\, sin(\Theta_{glass})\, cos^2(\theta_{glass}) \\ + \chi^{glass}_{zzz}\, sin^2(\theta_{glass})\, sin(\Theta_{glass})\end{aligned}$$

The generated fields depend on parameters defined at the fundamental frequency ω (lower case letters) and second-harmonic frequency 2ω (capital letters), such as the Fresnel transmission coefficients t_{ij} and T_{ij} at each interface, the propagation angles θ and Θ of the beams in the ABC layer and in the glass, as well as the refractive indices of the glass substrate n_{glass} and N_{glass}. As our model does not account for the birefringence of the material, we also neglected it in the Fresnel transmission coefficients and set the indices as the average of the ordinary and extraordinary indices (n=1.97, N=2.1). The thickness *L* and dispersion of the glass substrate are responsible for the period of the Maker fringes as the intensity is given by $I = c_1|E_{front} + E_{back}|^2$ where c_1 is a proportionality constant. The fitting procedure contains three real-valued free parameters: c_1, χ^{abc}_{zzz} and $(2\chi^{abc}_{xxz} + \chi^{abc}_{zxx})$. Other parameters used for the fitting are summarized in table 2. Assuming that the SHG originates from an effective bulk nonlinearity of the ABC layer, the respective bulk second-order susceptibility is obtained by dividing the measured surface-type signals by the thickness D of the ABC layer so that $\chi_{zzz} \equiv \frac{\chi^{abc}_{zzz}}{D}$ and $A_{zx} \equiv \frac{(2\chi^{abc}_{xxz} + \chi^{abc}_{zxx})}{D}$. The small discrepancy between experimental and fitting curve at small angles of incidence may be due to multiple reflections between the front and back surfaces, which our model does not account for. Our characterization also suffers from imperfections that manifest themselves in the non-diagonal components $(2\chi^{abc}_{xxz} + \chi^{abc}_{zxx})$., whose values for different samples vary by a factor of two. Note, however, that these components are particularly sensitive to the quality of the fit for small angles of incidence, whereas the diagonal component is relatively more important for large angles of incidence, where the fit is very good.

From this fitting procedure, we deduce the nonlinearity to be $\chi_{zzz} = 6.1 \pm 0.4$ pm/V ($\chi_{zzz} = 6.0 \pm 0.8$ pm/V) and $A_{zx} = 0.78 \pm 0.07$ pm/V ($A_{zx} = 1.44 \pm 0.16$ pm/V) for the 50 nm (25 nm) thick samples. Note that we find similar values for the bulk nonlinearities of the 50 nm and 25 nm thick samples. This shows that the SHG indeed originates from the bulk of the ABC layer rather than the ABC-air interface. Moreover it indicates that our measurements were not influenced by impurities adsorbed on the samples' surfaces which could alter the surface nonlinearities. Clearly, the main diagonal tensor component χ_{zzz} is significantly larger than the value of 0.26 pm/V reported before for a similar nanocomposite [11]. Assuming that Kleinman symmetry is satisfied, we can impose $\chi_{xxz} = \chi_{zxx}$ and then deduce also an order of magnitude value for $\chi_{zxx} \approx 0.35 \pm 0.15$ pm/V.

To gain further insight on the relative strengths between the diagonal and non-diagonal components, we also measured SHG from our 50 nm thick sample as a function of the polarization of the fundamental beam at a fixed incidence angle. Figure 3 shows that the SHG signal vanishes almost perfectly for s-polarized incident light, which confirms that the non-diagonal components of the nonlinear tensor are indeed much weaker than the diagonal one. Further studies are needed to obtain more precise values for the non-diagonal tensor components of our ABC composite.

To further demonstrate that the origin of the effective bulk nonlinearity is the broken centrosymmetry resulting from the ABC structure, we have acquired additional Maker fringes (see figure 4) from a structure where two ABC samples were brought together. The reference curve (crosses) corresponds to SHG from two blank glass substrates thus showing a weak response. The level of SHG is almost identical to the reference curve presented in figure 2 but presents fringes with a shorter period and reduced visibility as a consequence of the doubled thickness of the substrate. In particular, the temporal walk-off becomes more significant because of the thicker sample. The second curve (squares) is obtained using two identical ABC samples, coated on one side of the substrate. The two samples face each other on their uncoated sides so that the interfaces producing SHG are the two ABC layers while the glass-glass interface

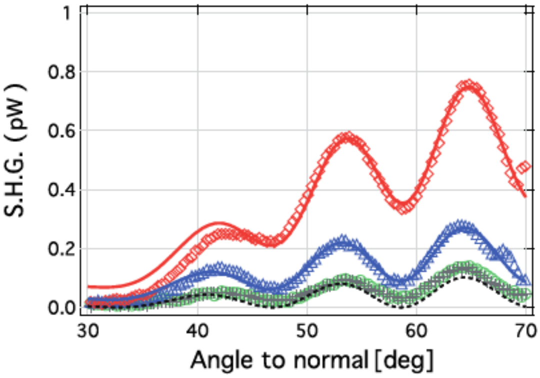

Figure 2: Experimental data (markers) and fitting curves (bold lines) of the second harmonic generation (average power) as a function of the incidence angle for 50 nm (diamonds), 25 nm (triangles), 2.1 nm (circles) and 0 nm (crosses) thick ABC composite coating deposited on the front surface of a Borofloat wafer.

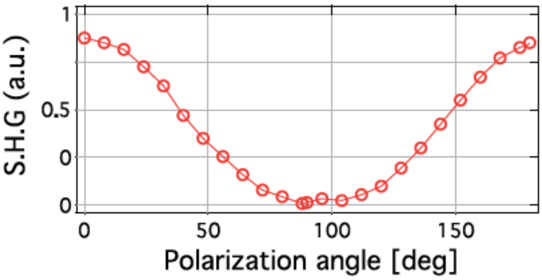

Figure 3: Variation of the SHG with the incident polarization angle.

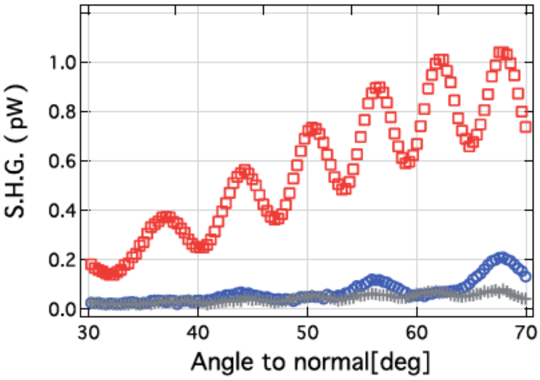

Figure 4: Comparison of SHG (average power) originating from 2 part-samples: ABC-glass+glass-CBA (red squares), glass-CBA+ABC-glass (blue circles), glass+glass (grey crosses).

does not produce SHG. This results in strong SHG with fringes exhibiting similar visibility as the blank sample. However, the visibility is still reduced for the reasons mentioned above. Finally, the last curve (circles) corresponds to those two same ABC-coated substrates but facing each other on their coated side. The nonlinear material has thus a restored symmetry as its cycling structure is now ABC…ABC-CBA…CBA and it is expected to result in negligible SHG. Indeed, while the SHG contributions from the air-glass interfaces of course remain, the curves indicate that the contributions from the ABC layers vanish to a large extent.

We should note that the samples of the present study were far from being optimized. In addition, our experimental setup was not yet optimized for the most precise measurements. While this affects mainly the weaker non-diagonal tensor components, both the diagonal and non-diagonal components are partly coupled through our fitting procedure. In order to take this remaining uncertainty into account, we believe that it is safe to state that the value of the dominant component is χ_{zzz} is 5 ± 2 pm/V.

Nevertheless this value for the main tensor component is greater by more than an order of magnitude than the 0.26 pm/V reported by Alloatti *et al.* [11] for a similar system. We note that only one material is different in the ABC composite in [11]: HfO_2 is used where we have In_2O_3. Since $\chi^{(2)}$ is expected to be proportional to the density of interfaces, we also assess this quantity in both cases. Each ABC period is 2.7 nm in [11] as compared to 2.1 nm in our study, so we find it can only explain for a difference of a factor 1.3 for the second-order susceptibility. This seems to indicate that the materials chosen, and likely also the deposition parameters, have a considerable influence on the effective bulk second-order susceptibility. Finally we want to mention that in [11] the surface nonlinearity of the glass substrate, and thus the interference between SHG from the front and back surfaces, is not accounted for; despite the fact that the Rayleigh range is much thicker than the sample. This can result in an underestimation of the nonlinearity when operating in a Maker-fringe minimum. However, it cannot accommodate for an order of magnitude difference. We think an important future study would be to investigate the possible correlation between the linear and/or nonlinear susceptibilities of many combinations of ABC materials and the resulting effective second-order susceptibility.

In conclusion, we have demonstrated an artificial nonlinear material relying on the principle of surface induced symmetry breaking. We believe that this new class of nonlinear material is promising as our proof of principle indicates a second-order nonlinearity reaching 5 ± 2 pm/V for its main tensor component. We believe that such a second-order nonlinearity could be used in combination with nanophotonic waveguides based on CMOS-compatible materials that lack significant second-order nonlinearity. We envisage sub-micron SiN waveguides with guided modes overlapping over 50% with the ABC composite coated on top of the waveguide. Furthermore, the possibilities to increase the nonlinearity of the ABC composite are numerous ranging from thinner individual layers to optimization of the contrast between the materials involved [14].

Funding. S.C., R.B., A.H., and J.D. would like to thank the ERC-InSpectra advanced grant and FWO-Vlaanderen for funding support. K.K. and M.K. acknowledge Tampere University of Technology for Optics and Photonics Strategic Funding. K.K. acknowledges the Vaisala Foundation for a Fellowship.

Acknowledgment. We thank Koen Alexander for his support in the automatization of the experimental setup.

References

1. J. S. Levy, A. Gondarenko, M. A. Foster, A. C. Turner-Foster, A. L. Gaeta, and M. Lipson, Nat. Photonics **4**, 37 (2010) .
2. L. Razzari, D. Duchesne, M. Ferrera, R. Morandotti, S. Chu, B. E. Little, and D. J. Moss, Nat. Photonics **4**, 41 (2010).
3. A. Liu, R. Jones, L. Liao, D. Samara-Rubio, D. Rubin, O. Cohen, R. Nicolaescu, and M. Paniccia, Nature **427**, 615 (2004).
4. R. A. Myers, N. Mukherjee, and S. R. J. Brueck, Opt. Lett. **16**, 1732 (1991).
5. T. Kim, J. Luo, J. Ka, S. Hau, Y. Tian, Z. Shi, N. M. Tucker, S. Jang, J. Kang, and A. K. Y. Jen, Adv. Mater. **18**, 3038 (2006).
6. M. Cazzanelli, F. Bianco, E. Borga, G. Pucker, M. Ghulinyan, E. Degoli, and L. Pavesi, Nat. Mater. **11**, 148 (2012).
7. M. Zdanowicz, J. Harra, J. M. Mäkelä, E. Heinonen, T. Ning, M. Kauranen, and G. Genty, Scientific Reports **4**, 5745 (2014).
8. I. R. Girling, P. V. Kolinsky, N. A. Cade, J. D. Earls, and I. R. Peterson, Opt. Commun. **55**, 289 (1985).
9. T. Ning, H. Pietarinen, O. Hyvärinen, J. Simonen, G. Genty, and M. Kauranen, Appl. Phys. Lett. **100**, 161902 (2012).
10. A. Kitao, K. Imakita, I. Kawamura, and M. Fujii, J. Phys. D Appl. Phys. **47**, 215101 (2014).
11. L. Alloatti, C. Kieninger, A. Froelich, M. Lauermann, T. Frenzel, K. Köhnle, W. Freude, J. Leuthold, M. Wegener, and C. Koos, Appl. Phys. Lett. **107**, 121903 (2015).
12. A. Khanna, A. Z. Subramanian, M. Häyrinen, S. Selvaraja, P. Verheyen, D. Van Thourhout, S. Honkanen, H. Lipsanen, and R. Baets, Opt. Express **22**, 5684 (2014).
13. E. Ghahramani, D. J. Moss, and J. E. Sipe, Phys. Rev. B **43**, 8990 (1991).
14. N. Bloembergen, R. K. Chang, S. S. Jha, and C. H. Lee, Phys. Rev. Lett. **174**, 813 (1968).
15. G. X. Liu, F. K. Shan, W. J. Lee, and B. C. Shin, J. Korean Phys Soc. **50**, 1827 (2007).
16. W. Shimizu, S. Nakamura, T. Sato, and Y. Murakami, Langmuir **28**, 12245 (2012).
17. J. Koo, S. Kim, S. Jeon, H. Jeon, Y. Kim, and Y. Won, J. Korean Phys. Soc. **48**, 131 (2006).
18. S. K. Kim, S. W. Lee, C. S. Hwang, Y. S. Min, J. Y. Won, and J. Jeong, J. Electrochem. Soc. **153**, F69 (2006).
19. D .Beena, K. J. Lethy, R. Vinodkumar, A. P. Detty, V. P. Mahadevan Pillai, and V. Ganesan, J. Alloy. Comp. **489**, 215 (2011).
20. Q. Xie, Y. L. Jiang, C. Detavernier, D. Deduytsche, R. L. Van Meirhaeghe, G. P. Ru, B. Z. Li, and X. P. Qu, J. Appl. Phys. **102**, 083521 (2007).
21. Q. Xie, J. Musschoot, D. Deduytsche, R. L. Van Meirhaeghe, C. Detavernier, S. Van den Berghe, Y. L. Jiang, G. P. Ru, B. Z. Li, and X. P. Qu, J. Electrochem. Soc. **155**, H688 (2008).
22. R. K. Ramachandran, J. Dendooven, H. Poelman, and C. Detavernier, J. Phys. Chem. C **119**, 11786 (2015).
23. R. L. Puurunen, J. Appl. Phys. **97**, 121301 (2005).
24. P. Lalanne, and M. Hutley, Encyclopedia of optical engineering, **62** (2003).
25. P. D. Maker, R. W. Terhune, M. Nisenhoff, and C. M. Savage, Phys. Rev. Lett. **8**, 21 (1962).
26. J. J. Maki, M. Kauranen, and A. Persoons, Phys. Rev. B **51**, 1425 (1995).
27. F. J. Rodriguez, F. X. Wang, and M. Kauranen, Opt. Express **6**, 8704 (2008).

Publication II

Recognition of multipolar second-order nonlinearities in thin-film samples

Kalle Koskinen, Robert Czaplicki, Tommi Kaplas and Martti Kauranen

Optics Express **24**, 4972-4978 (2016)

© 2016 Optical Society of America.
Reprinted with permission.

Recognition of multipolar second-order nonlinearities in thin-film samples

Kalle Koskinen,[1,*] Robert Czaplicki,[1] Tommi Kaplas,[2] and Martti Kauranen[1]

[1] *Department of Physics, Tampere University of Technology, P.O. Box 692, FI-33101 Tampere, Finland*
[2] *Institute of Photonics, University of Eastern Finland, P.O. Box 111, FI-80101 Joensuu, Finland*
**kalle.o.koskinen@tut.fi*

Abstract: We use two-beam second-harmonic generation to address thin films of silicon nitride (SiN). This technique is able to distinguish between the dipolar and higher-multipolar (magnetic and quadrupolar) contributions to the nonlinearity, as earlier shown for bulk samples. Our results for the SiN films exhibit strong multipolar signatures. Nevertheless, the results can be fully explained by the strong dipolar response of SiN once multiple reflections of the fundamental and second-harmonic fields within the film are properly taken into account. The results show that the recognition of multipolar nonlinearities requires extreme care for samples typically used for the characterization of new materials.

©2016 Optical Society of America

OCIS codes: (190 0190) Nonlinear optics; (310 6860) Thin films, optical properties

---

References and links

1 K L Sly, S -W Mok, and J C Conboy, “Second harmonic correlation spectroscopy: a method for determining surface binding kinetics and thermodynamics,” Anal Chem **85**(17), 8429–8435 (2013)
2 D E Wilcox, M E Sykes, A Niedringhaus, M Shtein, and J P Ogilvie, “Heterodyne-detected and ultrafast time-resolved second-harmonic generation for sensitive measurements of charge transfer,” Opt Lett **39**(14), 4274–4277 (2014)
3 Y R Shen, “Surface nonlinear optics: a historical perspective,” IEEE J Sel Top Quantum Electron **6**(6), 1375–1379 (2000)
4 L Alloatti, C Kieninger, A Froelich, M Lauermann, T Frenzel, K Köhnle, W Freude, J Leuthold, M Wegener, and C Koos, “Second-order nonlinear optical metamaterials: ABC-type nanolaminates,” Appl Phys Lett **107**(12), 121903 (2015)
5 S Clemmen, A Hermans, E Solano, J Dendooven, K Koskinen, M Kauranen, E Brainis, C Detavernier, and R Baets, “Atomic layer deposited second-order nonlinear optical metamaterial for back-end integration with CMOS-compatible nanophotonic circuitry,” Opt Lett **40**(22), 5371–5374 (2015)
6 P Guyot-Sionnest, W Chen, and Y R Shen, “General considerations on optical second-harmonic generation from surfaces and interfaces,” Phys Rev B Condens Matter **33**(12), 8254–8263 (1986)
7 P Guyot-Sionnest and Y R Shen, “Local and nonlocal surface nonlinearities for surface optical second-harmonic generation,” Phys Rev B Condens Matter **35**(9), 4420–4426 (1987)
8 J E Sipe, V Mizrahi, and G I Stegeman, “Fundamental difficulty in the use of second-harmonic generation as a strictly surface probe,” Phys Rev B Condens Matter **35**(17), 9091–9094 (1987)
9 N Bloembergen, R Chang, S Jha, and C Lee, “Optical second-harmonic generation in reflection from media with inversion symmetry,” Phys Rev **174**(3), 813–822 (1968)
10 F Wang, F Rodríguez, W Albers, and M Kauranen, “Enhancement of bulk-type multipolar second-harmonic generation arising from surface morphology of metals,” New J Phys **12**(6), 063009 (2010)
11 S Kruk, M Weismann, A Y Bykov, E A Mamonov, I A Kolmychek, T Murzina, N C Panoiu, D N Neshev, and Y S Kivshar, “Enhanced magnetic second-harmonic generation from resonant metasurfaces,” ACS Photonics **2**(8), 1007–1012 (2015)
12 I M Hancu, A G Curto, M Castro-López, M Kuttge, and N F van Hulst, “Multipolar interference for directed light emission,” Nano Lett **14**(1), 166–171 (2014)
13 J Butet, I Russier-Antoine, C Jonin, N Lascoux, E Benichou, and P -F Brevet, “Sensing with multipolar second harmonic generation from spherical metallic nanoparticles,” Nano Lett **12**(3), 1697–1701 (2012)
14 M R Shcherbakov, D N Neshev, B Hopkins, A S Shorokhov, I Staude, E V Melik-Gaykazyan, M Decker, A A Ezhov, A E Miroshnichenko, I Brener, A A Fedyanin, and Y S Kivshar, “Enhanced third-harmonic generation in silicon nanoparticles driven by magnetic response,” Nano Lett **14**(11), 6488–6492 (2014)
15 P Figliozzi, L Sun, Y Jiang, N Matlis, B Mattern, M C Downer, S P Withrow, C W White, W L Mochán, and B S Mendoza, “Single-beam and enhanced two-beam second-harmonic generation from silicon nanocrystals by use of spatially inhomogeneous femtosecond pulses,” Phys Rev Lett **94**(4), 047401 (2005)

Received 28 Dec 2015; revised 3 Feb 2016; accepted 3 Feb 2016; published 26 Feb 2016

16 S Cattaneo and M Kauranen, “Polarization-based identification of bulk contributions in surface nonlinear optics,” Phys Rev B **72**(3), 033412 (2005)
17 F J Rodríguez, F X Wang, B K Canfield, S Cattaneo, and M Kauranen, “Multipolar tensor analysis of second-order nonlinear optical response of surface and bulk of glass,” Opt Express **15**(14), 8695–8701 (2007)
18 F J Rodriguez, F X Wang, and M Kauranen, “Calibration of the second-order nonlinear optical susceptibility of surface and bulk of glass,” Opt Express **16**(12), 8704–8710 (2008)
19 F X Wang, F J Rodríguez, W M Albers, R Ahorinta, J Sipe, and M Kauranen, “Surface and bulk contributions to the second-order nonlinear optical response of a gold film,” Phys Rev B **80**(23), 233402 (2009)
20 Y Hase, K Kumata, S S Kano, M Ohashi, T Kondo, R Ito, and Y Shiraki, “New method for determining the nonlinear optical coefficients of thin films,” Appl Phys Lett **61**(2), 145 (1992)
21 T Ning, H Pietarinen, O Hyvärinen, J Simonen, G Genty, and M Kauranen, “Strong second-harmonic generation in silicon nitride films,” Appl Phys Lett **100**(16), 161902 (2012)
22 J Sipe, “New Green-function formalism for surface optics,” J Opt Soc Am B **4**(4), 481–498 (1987)

1. Introduction

Second-order nonlinear optical processes provide the basis for frequency conversion and electro-optic modulation of light. A prime example here is second-harmonic generation (SHG), i.e., conversion of light at a fundamental frequency ω to light at the doubled frequency 2ω. Within the electric-dipole approximation of the light-matter interaction, second-order processes can occur only in non-centrosymmetric materials. This is a crucial limitation in the search for new second-order materials. On the other hand, the centrosymmetry of any material is broken at its surface, giving rise to an electric-dipole-allowed surface nonlinearity. This has found several applications in surface spectroscopy [1–3]. More recently, it has been shown that by elaborate stacking of several surface layers, one can even build up artificial metamaterials with appreciable second-order response [4,5].

The symmetry properties of magnetic-dipole and electric-quadrupole interactions are different from those of electric-dipole interactions. In consequence, such higher-multipolar interactions can allow second-order effects even in the centrosymmetric bulk [6–9]. In principle, higher-multipolar responses could lead to completely new types of second-order materials, but their design guidelines are poorly understood. Nanostructured materials, where the higher multipoles should be interpreted in terms of effective (Mie-type) response, could provide an avenue forward [10,11]. Multipole interactions have also other important uses, e.g., in directional optical antennas [12], sensing [13], and third-order nonlinear optics [14].

In spite of these opportunities, the separation between the dipolar surface and multipolar bulk nonlinearity has been a long standing problem [3,6,7]. A breakthrough was achieved by SHG using two non-collinear beams at the fundamental frequency. This technique provides relatively simple, yet distinct signatures for the dipolar surface and multipolar bulk responses [15,16] and was subsequently used to quantify the dipolar and multipolar responses of bulk glasses and gold films [10,17–19]. In all these works, the sample was such that the reflections between its front and back surfaces could be excluded from the analysis. New materials, however, are often convenient to characterize as thin films, and need to be analyzed using models that account for the multiple reflections between the various interfaces [20]. Although conceptually straight-forward, such models are tedious to implement.

In this paper, we show that thin films provide additional challenges in the recognition of higher-multipolar nonlinearities. More specifically, SHG from a thin film of silicon nitride (SiN), which has strong dipolar second-order nonlinearity, gives rise to signatures of apparent multipolar origin when analyzed using the model justified for bulk samples. We further show that these signatures arise from multiple reflections within the thin film and can be fully explained by considering only the dipolar nonlinearity. These results emphasize the importance of using the most complete models to describe nonlinear processes, which further complicate the recognition of potential materials with strong higher-multipolar responses.

2. Two-beam second-harmonic generation

The dipolar surface and multipolar bulk contributions to SHG from isotropic materials can be separated by two-beam SHG [15,16]. In this arrangement, two non-collinear beams at the fundamental frequency and in the same plane of incidence are applied on the sample and the SHG signal generated jointly by the two beams is detected [Fig. 1]. For symmetry reasons, the multipolar response can only be accessed by using the two non-collinear beams. In addition, the dipolar and multipolar SHG signals behave very differently when their dependence on the polarizations of the fundamental beams is considered. For sufficiently thick bulk samples, the two fundamental beams can be made to cross at the front interface in such a way that they are separated at the back surface and the back reflections miss the interaction volume [Fig. 1].

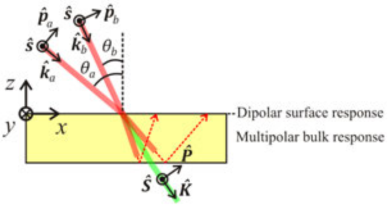

Fig 1 Schematic of two-beam SHG measurement and the used notation

We choose z-axis perpendicular to the sample surface and x-axis (y-axis) parallel (perpendicular) to the plane of incidence. Lower (upper) -case letters denote quantities at ω (2ω). The electric fields are $\mathbf{a}$ and $\mathbf{b}$ for the fundamental beam with larger (θ_a) and smaller (θ_b) angle of incidence, respectively. Such geometry is best analyzed in the $(\hat{\mathbf{p}},\hat{\mathbf{s}})$ basis, where p (s) polarization is in (perpendicular to) the plane of incidence.

The surface of an isotropic material has $C_{\infty v}$ symmetry, and thus the dipolar surface susceptibility tensor has three independent nonvanishing components χ_{zzz}, $\chi_{zxx} = \chi_{zyy}$, and $\chi_{xxz} = \chi_{xzx} = \chi_{yyz} = \chi_{yzy}$ [18]. The SHG source polarization for s-polarized SHG signal can then be shown to be of the form [17]

$$P_s^d = 2\chi_{xxz}\left(a_s b_p \sin\theta_b + a_p b_s \sin\theta_a\right), \tag{1}$$

where the fields are evaluated inside the nonlinear medium. The superscript d refers to dipolar origin of the source polarization and the subscripts s and p describe the beam polarizations.

The higher-multipole contributions are usually analyzed in terms of effective polarization. By accounting for the symmetry of the magnetic and quadrupole tensors, one finds that the effective polarization for isotropic media is of the form [8,9,16]

$$\mathbf{P}^{\mathrm{MP}} = \beta\mathbf{e}(\nabla\cdot\mathbf{e}) + \gamma\nabla(\mathbf{e}\cdot\mathbf{e}) + \delta'(\mathbf{e}\cdot\nabla)\mathbf{e}, \tag{2}$$

where β, γ and δ' are nonlinear material parameters, $\mathbf{e}$ denotes the total fundamental field and MP refers to higher multipoles. The first term in Eq. (2) makes no contribution and the second contributes to the effective surface response [6–9]. The distinguishable bulk contribution (δ') gives rise to the following s-polarized source [17]

$$P_s^{\delta'} = ik\delta'\sin\left(\theta_a - \theta_b\right)\left(a_s b_p - a_p b_s\right), \tag{3}$$

where k is the wavenumber of the fundamental field. Note that in Eq. (1) the terms $a_s b_p$ and $a_p b_s$ are in-phase when the incident angles have the same sign contrary to Eq. (3), where these terms are out-of-phase. This difference is crucial for the separation of the dipolar and multipolar contributions as the polarizations of the fundamental beams are modulated.

#256193 Received 28 Dec 2015; revised 3 Feb 2016; accepted 3 Feb 2016; published 26 Feb 2016
© 2016 OSA

In order to extend this formalism for thin films, we assume that the dipolar nonlinearity is still associated with $C_{\infty v}$ symmetry (with the tensor components given above), but could extend through the whole film, i.e., is not limited to surface only. This is compatible with the known structure of the SiN films, where such dipolar nonlinearity has “bulk” origin [21]. However, we assume that the possible higher-multipolar contributions can still be described by Eq. (3), based on isotropy in three dimensions. Such assumption is sufficient because any deviation of the measurements from the dipolar model would provide evidence of higher-multipole contributions.

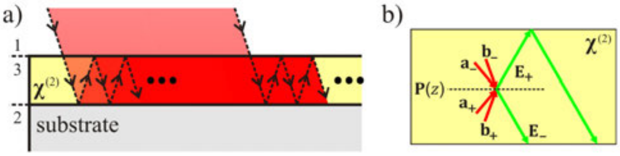

Fig 2 Schematic of the two main consequences of reflections in thin samples a) Multiple reflections contributing to the total field strength b) SHG generated into two directions in the nonlinear medium

The additional complications for thin-film samples arise from the fact that the width of the beams is generally much larger than the film thickness. As a result, parts of the beams reflected at both interfaces of the medium cannot be separated from another. Thus, the total field must be treated as an infinite series of upward and downward propagating partial waves [Fig. 2(a)]. In addition, a SHG source sheet at any given location emits waves both in the downward ($-$) and upward ($+$) directions, which again both undergo multiple reflections at the top and bottom interfaces [Fig. 2(b)]. The total SHG signal is then obtained by integrating the source sheets through the thickness of the nonlinear film (D).

In order to account for all the reflections, each fundamental incident field (**a** or **b**) gives rise to upward ($\mathbf{a}_+$ and $\mathbf{b}_+$) and downward ($\mathbf{a}_-$ and $\mathbf{b}_-$) propagating fields inside the film. These fields are $\mathbf{e}_\pm = \mathbf{e}_0 C_\pm \mathrm{e}^{iw_\pm z}$, where

$$C_+ = \frac{t_{13} r_{32} \mathrm{e}^{2i|w|D}}{1 - r_{31} r_{32} \mathrm{e}^{2i|w|D}}, \text{and } C_- = \frac{t_{13}}{1 - r_{31} r_{32} \mathrm{e}^{2i|w|D}}. \tag{4}$$

Here w is the z-component of the wave vector ($w = \omega n \cos\theta / c$, where n is the refractive index at the fundamental wavelength and c is the speed of light), t (r) is transmission (reflection) Fresnel coefficient and indices 1 (air), 3 (film) and 2 (glass substrate) denote respective media. The SHG field exhibits similar behavior, but only gives rise to an overall scaling factor since we limit ourselves to only s-polarized signal. Note that all quantities need to be evaluated separately for beams **a** and **b**.

The local nonlinear polarization acts as a source for upward and downward propagating SHG fields. Phase-matching considerations are most conveniently accounted for by Green’s function formalism for nonlinear optics [22]. The total SHG field amplitude in the medium can then be written as

$$E_s \propto \sum_{\alpha,\beta \in \{+,-\}} \left[P_s^d \left(a_\alpha, b_\beta \right) + P_s^{\delta'} \left(a_\alpha, b_\beta \right) \right] \left(G_{\alpha,\beta} + R_{31}^s G'_{\alpha,\beta} \right), \tag{5}$$

where

$$G_{\alpha,\beta} = \frac{1 - \exp\left(-i \left(w_{a,\alpha} + w_{b,\beta} + W \right) D \right)}{i \left(w_{a,\alpha} + w_{b,\beta} + W \right)}, \text{ and } G'_{\alpha,\beta} = \frac{1 - \exp\left(-i \left(w_{a,\alpha} + w_{b,\beta} - W \right) D \right)}{i \left(w_{a,\alpha} + w_{b,\beta} - W \right)} \tag{6}$$

and subscripts $\alpha,\beta\in\{+,-\}$ denote the direction of propagation of the partial beams related to a and b, respectively, $W=2\omega N\cos(\Theta)/c$ (N and Θ are the refractive index and the angle of incidence at the second-harmonic wavelength, respectively). Finally, by combining Eqs. (2), 4–6), the s-polarized SHG field can be written as

$$E_s \propto h_s a_p b_s + k_s a_s b_p, \tag{7}$$

where h_s and k_s are linear combinations of χ_{xxz} [Eq. (1)] and $k\delta'$ [Eq. (3)], and can be written as

$$\begin{bmatrix} h_s \\ k_s \end{bmatrix} = \begin{bmatrix} m_{11} & m_{12} \\ m_{21} & m_{22} \end{bmatrix} \begin{bmatrix} \chi_{xxz} \\ k\delta' \end{bmatrix}, \text{where} \tag{8a}$$

$$\begin{aligned} m_{11} &= 2\sin(\theta_a)\sum_{\alpha,\beta\in\{+,-\}} C_\alpha^{a,p} C_\beta^{b,s}\left(G_{\alpha,\beta}+R_{31}^s G'_{\alpha,\beta}\right) \\ m_{12} &= i\sum_{\alpha,\beta\in\{+,-\}} C_\alpha^{a,p} C_\beta^{b,s}\left(G_{\alpha,\beta}+R_{31}^s G'_{\alpha,\beta}\right)1_\beta \sin\left(\theta_a - 1_\alpha 1_\beta \theta_b\right), \\ m_{21} &= 2\sin(\theta_b)\sum_{\alpha,\beta\in\{+,-\}} C_\alpha^{a,s} C_\beta^{b,p}\left(G_{\alpha,\beta}+R_{31}^s G'_{\alpha,\beta}\right) \\ m_{22} &= -i\sum_{\alpha,\beta\in\{+,-\}} C_\alpha^{a,s} C_\beta^{b,p}\left(G_{\alpha,\beta}+R_{31}^s G'_{\alpha,\beta}\right)1_\beta \sin\left(\theta_a - 1_\alpha 1_\beta \theta_b\right) \end{aligned} \tag{8b}$$

and $1_\pm = \pm 1$. The relationship between auxiliary coefficients (h_s, k_s) and material parameters $(\chi_{xxz}, k\delta')$ depends only on the geometry of the experiment, and the matrix $\left[m_{ij}\right]$ describing it can be fully determined beforehand.

In the limit where all reflections are neglected, h_s and k_s are

$$\begin{aligned} h_s &= \left[2\chi_{xxz}\sin(\theta_a) - ik\delta'\sin\left(\theta_a-\theta_b\right)\right] t_{13}^{a,p} t_{13}^{b,s}, \\ k_s &= \left[2\chi_{xxz}\sin(\theta_b) + ik\delta'\sin\left(\theta_a-\theta_b\right)\right] t_{13}^{a,s} t_{13}^{b,p} \end{aligned} \tag{9}$$

which can also be obtained directly from Eqs. (1) and (3). Thus, h_s and k_s are perfectly in-phase when the multipolar parameter $k\delta'$ is zero. However, the complete expression of Eq. (8) can give rise to a phase difference between h_s and k_s even when $k\delta'$ vanishes.

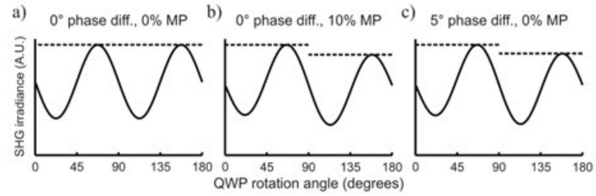

Fig 3 Three simulations of a measurement: a) reflections neglected, no multipole contribution; b) reflections neglected, 10% multipole contribution; c) 5° phase difference between h_s and k_s, no multipole contribution

The separation of the dipolar and multipolar responses relies on simultaneous control of the relative phase and amplitude between factors $a_p b_s$ and $a_s b_p$. This can be accomplished when one fundamental beam is linearly polarized along direction $\hat{\mathbf{a}} = (\hat{\mathbf{p}} - \hat{\mathbf{s}})/\sqrt{2}$ and the other is initially linearly polarized $\hat{\mathbf{b}} = \hat{\mathbf{p}}$, and then varied by a rotating quarter-wave plate [16]. If reflections are neglected, any phase difference between h_s and k_s would: 1) be seen as a difference between peak heights in the measured graph and 2) indicate a nonvanishing multipole response [Figs. 3(a) and 3(b)]. However, if reflections are taken into account, similar phase difference can arise strictly from the multiple reflections in the film [Fig. 3(c)]. Thus, neglecting reflections for thin films can lead to incorrect values for nonlinear parameters or even false positives for the multipole response.

3. Experimental results

To verify our findings experimentally, we studied an 800 nm thick film of SiN previously verified to have $C_{\infty v}$ symmetry and dipolar bulk nonlinearity [21]. The film was fabricated by plasma enhanced chemical vapour deposition on a fused silica substrate. The SHG experiments were performed with a setup described by Rodriguez *et al.* in [17], which uses a pulsed Nd:YAG laser (wavelength 1064 nm, pulse length 60 ps, pulse energy 0.15 mJ and pulse repetition rate 1000 Hz). The initial powers and polarizations of the control (**a**) and probe (**b**) beams were set using linear polarizers and half-wave plates. The polarizations of the beams were initially set to $\hat{\mathbf{a}} = (\hat{\mathbf{p}} - \hat{\mathbf{s}})/\sqrt{2}$ and $\hat{\mathbf{b}} = \hat{\mathbf{p}}$, and the angles of incidence were $\theta_a = 58.3^\circ$ and $\theta_b = 32.0^\circ$, i.e., same sign but different magnitude. During the measurement, the probe polarization was varied using a motorized quarter-wave plate while measuring the *s*-polarized SHG in transmission using an analyzer and a photomultiplier tube.

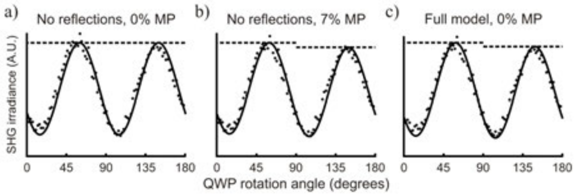

Fig 4 Experimental data fitted in three different ways: a) traditional model without multipole contribution; b) traditional model with multipole contribution and c) detailed model without multipole contribution

The experimental data was fitted using both models: the simplified one described by Eq. (9) [Figs. 4(a) and 4(b)] and the detailed one described by Eq. (8) without multipolar contribution [Fig. 4(c)]. The traditional (simplified) model predicts a multipolar response due to difference between the peak heights and yields a multipolar contribution of approximately 7% with respect to χ_{xxz}, with a mean squared error (MSE) of 3.6 in arbitrary units. However, the detailed model based on the dipolar response, multiple reflections, and propagation effects, produces a better fit (MSE 2.9) even though there are less free parameters.

4. Conclusions

We have presented a careful theoretical and experimental analysis of two-beam second-harmonic generation in addressing magnetic and quadrupole contributions to the second-order nonlinearity of films with sub-wavelength thickness. Our results show that a simplified analysis of the results may lead to apparent multipolar responses of significant magnitude. However, the results can be fully explained by the dipolar response when multiple reflections and propagation effects within the nonlinear film are properly taken into account. The results underline the importance of using detailed theoretical models in analyzing the nonlinear responses of thin films. Reliable recognition of multipolar responses is likely to require a more extensive set of experiments to be performed and fully analyzed.

Acknowledgments

The authors would like to thank Outi Hyvärinen from the Optoelectronics Research Centre at Tampere University of Technology, for the sample preparation. We also acknowledge the Academy of Finland (265682, 287886 and 287651) for funding. K.K. acknowledges the Väisälä foundation for funding a personal fellowship.

#256193 Received 28 Dec 2015; revised 3 Feb 2016; accepted 3 Feb 2016; published 26 Feb 2016

© 2016 OSA

Publication III

Bulk second-harmonic generation from thermally evaporated indium selenide thin films

Kalle Koskinen, Abdallah Slablab, Sasi Divya, Robert Czaplicki, Semen Chervinskii, Madanan Kailasnath, Padmanabhan Radhakrishnan and Martti Kauranen

Optics Letters **42**, 1076-1079 (2017)
© 2017 Optical Society of America.
Reprinted with permission.

Bulk second-harmonic generation from thermally-evaporated indium selenide thin films

KALLE KOSKINEN,[1,#] ABDALLAH SLABLAB,[1,*,#] SASI DIVYA,[2] ROBERT CZAPLICKI,[1] SEMEN CHERVINSKII,[3,4] MADANAN KAILASNATH,[2] PADMANABHAN RADHAKRISHNAN,[2] AND MARTTI KAURANEN[1]

[1] *Laboratory of Photonics, Tampere University of Technology, FI-33101 Tampere, Finland*
[2] *International School of Photonics, Cochin University of Science and Technology, Cochin 682022, India*
[3] *Institute of Photonics, University of Eastern Finland, FI-80101 Joensuu, Finland*
[4] *Institute of Physics, Nanotechnology and Telecommunications, St.Petersburg Polytechnic University, 195251 St.Petersburg, Russia*
[#] *These authors contributed equally to this work.*
**Corresponding author: abdallah.slablab@tut.fi*

Received 3 January 2017; revised 10 February, 2017; accepted 12 February 2017; posted 13 February 2017 (Doc. ID 283997); published 6 March 2017

We investigate bulk second-order nonlinear optical properties of amorphous indium selenide thin films fabricated by thermal evaporation. Such films are shown to exhibit strong and photostable second-harmonic generation (SHG). We report strong thickness-dependence of the second-harmonic signals as characterized by the Maker-fringe method. The absolute value of the nonlinear susceptibility tensor of the film is addressed by analyzing the interference of SHG signals from the film and the glass substrate. The value of the joint non-diagonal component of the susceptibility is found to be 4 pm/V, which is comparable to that of widely used second-order nonlinear materials. © 2017 Optical Society of America

OCIS codes: *(190.0190) Nonlinear optics; (190.4400) Nonlinear optics, materials; (310.6860) Thin films, optical properties.*

http://dx.doi org/10.1364/OL.99 099999

There is continuing interest in the development of thin film materials with strong nonlinear optical response, motivated by the possibility of fabricating compact and flexible nanometer scale nonlinear optical devices, such as tunable light sources [1], optical parametric oscillators [2] and electro-optical modulators [3]. The development of second-order nonlinear materials is particularly difficult due to their non-centrosymmetry requirement [4]. Traditionally, such materials are based on appropriate crystals or poled polymer films. Recently, however, it has been found that relatively simple thin film growth techniques, such as plasma enhanced chemical vapor deposition (PECVD) [5], pulsed laser deposition [6] or thermal evaporation [7], can lead spontaneously to a strong second-order response. Indeed, silicon nitride (SiN) films fabricated using PECVD were reported to possess a strong second-order response, with the dominant nonlinear susceptibility for second-harmonic generation (SHG) of χ_{zzz} ~2.5 pm/V [5], which is comparable to that of traditional second-order crystals [4]. Even higher values have been reported for SiN [8] and it has already been used in nonlinear waveguides [9].

Chalcogenide glasses (ChGs) are an interesting family of materials, which show promise for various optical and photonic applications [10]. Diverse physical properties of ChGs, such as the index of refraction or energy band gap, can be easily tailored by varying the elemental composition of the glass. ChGs are also known for high third-order nonlinearity and exceptional transmission in the infrared region [11,12].

Among the large variety of ChGs, indium selenide (InSe), a group III-VI semiconductor, has gained attention due to its anisotropic optical, electronic and mechanical properties enabling possible applications in energy conversion [13] and in nano- and opto-electronics [14]. The optical properties of InSe are particularly interesting because it can exist in several different phases and crystal structures for a given stoichiometric ratio of the atomic constituents [15]. The nonlinear optical response of thin films of crystalline InSe reveals different possible contributions of the surface and bulk effects to the SHG response. Depending on how the film is fabricated, the origin and the strength of SHG may be due to surface roughness, broken inversion symmetry of the layered structure, stacking of separate monolayers with different domain orientations or even the presence of small nanocrystals with different crystalline domains [16,17]. Recently, the strength of the SHG was explored by controlling the thickness of the film, showing interplay between surface and bulk contributions to SHG [18]. While the second-order response of InSe is tied to the fabrication method, manufacturing crystalline InSe at large scale remains a tedious and costly process. Thus, addressing the second-order response of InSe films fabricated using simpler and more cost-effective techniques is an important issue.

In this letter, we use simple and inexpensive thermal evaporation to fabricate amorphous InSe thin films and study their second-order properties by SHG. We show that the films have a significant and photostable nonlinear response. The response depends on film thickness, suggesting bulk origin of the response. The magnitude of the second-harmonic (SH) susceptibility of the samples is addressed by analyzing the interference of the SHG signals from the InSe film and the glass substrate, and is found to be comparable to that of amorphous SiN [5].

The samples were fabricated by thermal evaporation [19]. Glass substrates (plain microscope slides) were placed in a vacuum chamber (pressure 10^{-5} Torr) and located above a bulk InSe source prepared by the well-known melt quenching method [20]. The source constituents were weighted beforehand according to their atomic percentages (Se: 62%, In: 38%, Sigma Aldrich, 5N purity) and were melted at 1000°C, thereby forming a bulk InSe source. The source was then heated up to the temperature of ~300°C. The vaporized gas mixture coated the substrates with the speed of 1 Å/s and the film thickness was controlled by the deposition time. Samples with thicknesses from 40 nm to 190 nm were fabricated. The chemical composition of the samples was confirmed by energy-dispersive X-ray spectroscopy (EDS; not shown). The elemental analysis of the sample confirmed the purity of the deposited films by showing the presence of only In and Se.

The surface homogeneity and thickness of the samples were addressed by atomic force microscopy (AFM) for different sample areas. The results (not shown) confirm that the films are homogenous with an estimated thickness variance of ±4 nm. The optical transmission spectra of the films [Fig. 1(a)] were determined using a spectrophotometer. As expected, the transmission decreases with increasing thickness for wavelengths below about 700 nm, which is the range including SHG in our experiments. The slightly reduced transmission for longer wavelengths arises from interference within the sub-wavelength thick film. The linear optical properties were subsequently measured by ellipsometry. This confirmed that absorption is negligible for wavelengths above 1 µm, a known feature of chalcogenide materials. Thus, we neglect absorption at the fundamental wavelength of our laser source (1064 nm) but take it into account at the SH wavelength (532 nm). We further neglect birefringence and use an isotropic model for the ellipsometry. This approach was found to perform adequately, yielding the refractive indices of 3.02+i0.28 at 532 nm and 2.63 at 1064 nm, respectively, for the 190 nm film. Due to the homogeneity of the surface properties and elemental composition between the samples, we assume that there is little variation in the refractive index for different samples. Hence, we use the above values in the forthcoming numerical fitting of the experimental results.

To measure the SHG response, we used an experimental setup identical to the one in [5], with the following parameters: laser wavelength 1064 nm, pulse length 70 ps, repetition rate 1 kHz and spot size of the weakly focused beam at the sample ~400 μm. In order to perform the SHG Maker-fringe characterization [21], the sample was placed on a high precision motorized rotation stage, which allows the angle of incidence to be varied.

First, we verified the SHG origin of the signal by studying *p* polarized SHG generated by *p* polarized incident beam from the sample at 60° angle of incidence [for notation, see Fig. 1(b)]. The quadratic power dependence confirms the SHG origin of the signal, as indicated in Fig. 1(c). It is also clear that the SHG signal increases significantly with the film thickness under identical experimental conditions. Such result suggests that the SHG has bulk origin. From our experience, thermal instability and laser damage are typical issues for thermally evaporated thin films. Thus, we studied the photostability of the signal by illuminating the sample with a focused beam at different positions under average incident power of 20 mW for up to 15 minutes. The measured signal remained constant with a high signal-to-background ratio and none of the typical instability or damage issues were observed.

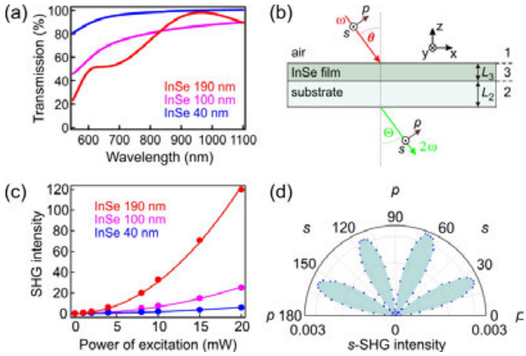

Fig. 1. (a) Transmission spectra of InSe films with different thicknesses: 40 nm (blue), 100 nm (magenta) and 190 nm (red). (b) Schematic of the cross-section of the sample with incident and SH beams. (c) Quadratic dependence of SHG intensity versus incident laser power for different samples. (d) *s*-polarized SHG intensity of 190 nm thick film as a function of polarization state of incident beam modulated by a HWP.

In order to analyze the SHG from the InSe films, the symmetry of the sample was determined by studying the *s*- and *p*-polarized SHG as a function of the linear polarization of the fundamental beam. We found that the *s*-polarized signal vanishes for both *s*- and *p*-polarized fundamental light [Fig. 1(d)], which suggests that the sample is at least in-plane isotropic (symmetry group $C_{\infty,v}$) [22]. Thus, the non-vanishing SHG susceptibility tensor components are limited to χ_{zzz}, $\chi_{xxz} = \chi_{xzx} = \chi_{yyz} = \chi_{yzy}$ and $\chi_{zxx} = \chi_{zyy}$, where *z*-axis is perpendicular to the surface of the sample and *x*- and *y*- axes are the two equivalent in-plane directions.

The qualitative polarization-dependent experiment is not sufficient to distinguish between in-plane isotropy (tensor components defined for the bulk of the material) and full three-dimensional isotropy (tensor components defined for surface-type response). Therefore, we characterized the sample by the Maker-fringe technique, where the interference between the SHG signals from the InSe film and the back surface of the substrate lead to fringes [Fig. 2(a)]. The Maker fringes are easily distinguishable for all samples and the signal is significantly stronger than the one from the substrate. In fact, even the lowest signal, from 40 nm thick film, is 4 times higher than that from the substrate, which suggests that the SHG is from the bulk of the film. In order to estimate the strength of SHG, the signal from the 100 nm thick sample was compared to the signal from a SiN film of the same thickness [5]. The SHG signals from InSe and SiN are comparable, with the signal from SiN being slightly higher than the one from InSe.

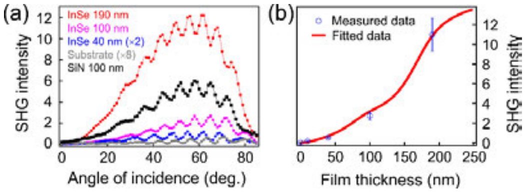

Fig. 2. (a) Maker-fringes of substrate (gray), 190 nm InSe (red), 100 nm InSe (magenta), 40 nm InSe (blue) and 100 nm SiN (black). (b) Experimental SHG (blue circles) and theoretical fit (solid red line) versus InSe thickness.

In order to confirm our findings, we studied the thickness dependence of the SHG signal while taking into account the infinite number of reflections of both beams within the film [23]. This can be done by utilizing the Green's function formalism for nonlinear optics with complex index of refraction [24,25]. In principle, both the upward and downward (positive and negative z-component of the wave-vector, respectively) propagating fundamental beams act as a source to SHG which also has an upward and downward propagating component. However, the contribution from upward propagating fundamental beams to downward propagating SHG is negligible due to poor phase-matching and low irradiance of the reflected fundamental beams. In addition, the upward propagating SHG is attenuated due to the longer propagation path in the absorptive medium and lower irradiance due to reflection at the film-air interface, and can also be neglected. Thus, the SHG irradiance outside the sample can be expressed as

$$I(L_3) \propto \left| \left(\frac{\left(\mathrm{e}^{i\Delta k L_3} - \mathrm{e}^{\alpha L_3} \right) (t_{13})^2 T_{32} T_{21}}{(i\Delta k + \alpha)\left(1 - R_{32} R_{31}\, \mathrm{e}^{(i2W_3 - \alpha)L_3}\right)} \right) \frac{1}{\left(1 - r_{32} r_{31}\, \mathrm{e}^{i2w_3 L_3}\right)^2} \right|^2 \tag{1}$$

where L_3 is the film thickness, α is the absorption coefficient for the SH field, w_3 (W_3) is the z-component of the wave-vector for fundamental (SH) wavelength, $\Delta k = W_3 - 2w_3$ is the phase-mismatch, and the factors t_{ij} (T_{ij}) and r_{ij} (R_{ij}) are the transmission and reflection Fresnel coefficients of the interface between media i and j for the fundamental (SH) wavelength, respectively. Note that Eq. (1) does not yet take into account surface SHG from the back substrate-air interface which interferes with SHG from the film and causes fringes with varying angles of incidence. For representative signal levels, we averaged the SHG responses between the extrema about a given nominal angle of incidence and included respective error bars to illustrate the maximum error due to interference.

The experimental SHG data for samples of different thicknesses fitted using Eq. (1) is shown in Fig. 2(b). Note that our fit uses only an overall scaling factor as free parameter. The blue dots illustrate the experimental data corresponding to the highest value of the SHG intensity for different film thicknesses given by Maker-fringe measurements. The model (red line) predicts a thickness dependence with a particular shape. The signal increases quadratically for small thicknesses until absorption effects and phase effects of reflected beams come into play, distorting the quadratic shape. A similar effect was also observed for van der Waals InSe crystalline films [18]. Due to the experimental values being explained well by the model, the assumption of bulk-type SHG response is well founded. The small film thickness variation and identical SHG response from different parts of the sample suggest that the bulk-type response could arise from atomic layers with preferred crystalline orientations formed during the growth of InSe clusters in the fabrication process.

To address the SHG tensor components quantitatively, the Maker-fringe results were analyzed using a method similar to reported previously [26,27]. However, we take into account multiple reflections [23] and absorption. Furthermore, the refractive indices of the film at both wavelengths are very high, and thus the coupling between the sample z-coordinate and the p-polarized beam components is extremely weak. As a result, any noise will break the statistical independence between χ_{zzz} and the non-diagonal components. Therefore, we neglect χ_{zzz} as it cannot be reliably addressed. We thus write the SH field as

$$\begin{aligned} E_{film} = {} & \frac{8i\pi\omega^2}{c^2 (W_3 + i\alpha)} (t_{13})^2 T_{32} T_{21} \\ & \times \left(\chi_{xxz} \sin(2\theta_3) \cos\Theta_3 + \chi_{zxx} \cos^2\theta_3 \sin\Theta_3 \right) \\ & \times \left(\frac{1}{1 - r_{32} r_{31} e^{i2w_3 L_3}} \right)^2 \left(\frac{1}{1 - R_{32} R_{31} e^{(i2W_3 - \alpha)L_3}} \right) \\ & \times \left(\frac{e^{i\Delta k L_3} - e^{-\alpha L_3}}{i\Delta k + \alpha} \right), \end{aligned} \tag{2}$$

where θ_3 (Θ_3) is the propagation angle inside the nonlinear medium for the fundamental (SH) wavelength, respectively, c is the speed of light and ω is the angular frequency of the fundamental beam. As discussed in [27], it is extremely difficult to separate χ_{xxz} from χ_{zxx} with a Maker-fringe experiment. Instead, we follow an approach similar to the one presented in [27]: We assume Kleinman symmetry in the numerical analysis and calculate the value of the joint non-diagonal tensor component $A_{xz} = 2\chi_{xxz} + \chi_{zxx}$. Note that this joint component is alternatively obtained from Eq. (2) by neglecting dispersion, i.e., by assuming that the propagation angles at the two frequencies are equal. By comparing these alternative approaches, we find that they result in at most 11% error for the value of the joint component.

Similarly, we have for the SHG from the substrate back surface:

$$\begin{aligned} E_{glass} = {} & \frac{-8i\pi\omega^2}{c^2 W_2} (t_{13})^2 (t_{32})^2 T_{21} \left[\chi_{xxz}^{glass} \sin(2\theta_2) \cos(\Theta_2) \right. \\ & + \chi_{zxx}^{glass} \cos^2(\theta_2) \sin(\Theta_2) \\ & \left. + \chi_{zzz}^{glass} \sin^2(\theta_2) \sin(\Theta_2) \right] \left(\frac{1}{1 - r_{32} r_{31} e^{i2w_3 L_3}} \right)^2, \end{aligned} \tag{3}$$

where χ^{glass} is the surface SHG susceptibility of a standard BK7 glass ($\chi_{xxz}^{glass} = 14.6$, $\chi_{zxx}^{glass} = 7$, $\chi_{zzz}^{glass} = 93$, all in 10^{-22} m^2/V, based on the susceptibility of quartz of $\chi_{xxx}^{quartz} = 0.80$ pm/V [28]). In the experiment, the SHG from InSe and glass interfere, and the total SHG irradiance detected outside the sample can be written as

$$I \propto \left| E_{film} e^{iW_2 L_2} + E_{glass} e^{i2w_2 L_2} \right|^2, \qquad \textbf{(4)}$$

where w_2 is the z-component of the wave-vector in the substrate for the fundamental wavelength, and L_2 is the thickness of the substrate. The absolute value of the SHG susceptibility of the film is then obtained from the modulation depth of the interference [27]. The experimental results fitted using Eq. (4) are shown in Fig. 3. The results (solid lines) are in excellent agreement with the measured data for all samples, reproducing the modulation depth and period of the fringes correctly. The obtained values of the joint non-diagonal tensor component A_{xz} are 4.1 ± 0.5 pm/V, 4.0 ± 0.5 pm/V and 2.9 ± 0.4 pm/V for 190 nm, 100 nm and 40 nm thick InSe films, respectively.

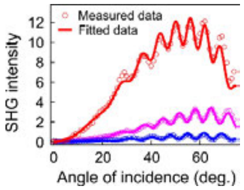

Fig. 3. Experimental SHG signal (circles) and fitting curves (lines) as a function of the angle of incidence for 40 nm (blue), 100 nm (magenta) and 190 nm (red) thick InSe films.

Remarkably, the values of the non-diagonal tensor components are of the same order of magnitude as for most well-known nonlinear crystals [4]. The acquired values are consistent for the two thickest samples with the 40 nm sample having about 25% smaller susceptibility. This may be due to the choice to neglect the upward propagating beams. Although such contributions would be small due to the poor phase-matching and SHG absorption within the film for the thicker samples, they may be non-negligible for the 40 nm sample. It is also possible that the slightly higher surface roughness of the 40 nm sample causes the error. Another interesting result is the shift in the angle corresponding to the maximum SHG signal level neglecting the interference for samples of different thicknesses (Fig. 3). Intuitively, this could be interpreted as change in the tensor structure, but the fitting is done only to a single tensor component as the measurement is insensitive to the diagonal component and the difference between the two non-diagonal components. Thus, the shift is fully explained by the reflection and absorption effects, highlighting the need for a sufficiently rigorous analysis when drawing conclusions from SHG experiments.

In summary, we have characterized amorphous InSe thin films fabricated using thermal evaporation. We report a strong, thickness dependent SHG from the samples. A detailed study on films of varying thicknesses yielded the value of the joint non-diagonal tensor component of the SHG susceptibility to be around 4 pm/V. Our results suggest that an amorphous InSe is a promising nonlinear optical material with potential applicability for photonic devices. In addition, our results provide general guidelines for the determination of the second-order susceptibility of amorphous and absorptive thin films.

Funding. Academy of Finland (256272, 274649). K.K. acknowledges the Väisälä Foundation for a personal fellowship.

Acknowledgment. The authors thank Tero Isotalo for AFM measurements.

References

1. S. Schwarz, S. Dufferwiel, P. M. Walker, F. Withers, A. A. P. Trichet, M. Sich, F. Li, E. A. Chekhovich, D. N. Borisenko, N. N. Kolesnikov, K. S. Novoselov, M. S. Skolnick, J. M. Smith, D. N. Krizhanovskii, and A. I. Tartakovskii, Nano Lett. **14**, 7003–7008 (2014).
2. J. S. Levy, A. Gondarenko, M. A. Foster, A. C. Turner-Foster, A. L. Gaeta, and M. Lipson, Nat. Photon. **4**, 37–40 (2010).
3. L. Chang, Y. Li, N. Volet, L. Wang, J. Peters, and J. E. Bowers, Optica **3**, 531–535 (2016).
4. R. W. Boyd, *Nonlinear Optics* (Academic Press, San Diego, 2008), 3rd ed.
5. T. Ning, H. Pietarinen, O. Hyvärinen, J. Simonen, G. Genty, and M. Kauranen, Appl. Phys. Lett. **100**, 161902 (2012).
6. M. Hrdlicka, J. Prikryl, M. Pavlista, L. Benes, M. Vlcek, and M. Frumar, J. Phys. Chem. Sol. **68**, 846–849 (2007).
7. M. El-Nahass, A.-B. A. Saleh, A. Darwish, and M. Bahlol, Opt. Commun. **285**, 1221-1224 (2012).
8. E. F. Pecora, A. Capretti, G. Miano, and L. Dal Negro, Appl. Phys. Lett. **102**, 141114 (2013).
9. M. W. Puckett, R. Sharma, H.-H. Lin, M. han Yang, F. Vallini, and Y. Fainman, Opt. Express **24**, 16923-16933 (2016).
10. D. Lezal, J. Pedlikova, and J. Zavadila, J. Opt. Adv. Mater. **6**, 133–137 (2004).
11. I. Chung and M. G. Kanatzidis, Chem. Mater. **26**, 849–869 (2014).
12. A. Zakery and S. Elliott, *Optical Nonlinearities in Chalcogenide Glasses and their Applications* (Springer Berlin Heidelberg, 2007).
13. S. R. Tamalampudi, Y.-Y. Lu, R. K. U., R. Sankar, C.-D. Liao, K. M. B., C.-H. Cheng, F. C. Chou, and Y.-T. Chen, Nano Lett. **14**, 2800–2806 (2014).
14. W. Feng, X. Zhou, W. Q. Tian, W. Zheng, and P. Hu, Phys. Chem. Chem. Phys. **17**, 3653–3658 (2015).
15. L. Debbichi, O. Eriksson, and S. Lebègue, J. Phys. Chem. Lett. **6**, 3098–3103 (2015).
16. E. Bringuier, A. Bourdon, N. Piccioli, and A. Chevy, Phys. Rev. B **49**, 16971–16982 (1994).
17. M. Parlak, C. Ercelebi, I. Günal, Z. Salaeva, and K. Allakhverdiev, Thin Solid Films **258**, 86 – 90 (1995).
18. S. Deckoff-Jones, J. Zhang, C. E. Petoukhoff, M. K. Man, S. Lei, R. Vajtai, P. M. Ajayan, D. Talbayev, J. Madéo, and K. M. Dani, Sci. Rep. **6**, 22620 (2016).
19. A. Slablab, K. Koskinen, R. Czaplicki, N. T. Karunakaran, I. Sebastian, C. P. Chandran, M. Kailasnath, P. Radhakrishnan, and M. Kauranen, Proc. SPIE **9126**, 912621 (2014).
20. R. Tintu, V. Nampoori, P. Radhakrishnan, and S. Thomas, Opt. Commun. **284**, 222 – 225 (2011).
21. P. D. Maker, R. W. Terhune, M. Nisenoff, and C. M. Savage, Phys. Rev. Lett. **8**, 21–22 (1962).
22. N. Bloembergen, R. K. Chang, S. S. Jha, and C. H. Lee, Phys. Rev. **174**, 813–822 (1968).
23. K. Koskinen, R. Czaplicki, T. Kaplas, and M. Kauranen, Opt. Express **24**, 4972–4978 (2016).
24. J. Maki, M. Kauranen, and A. Persoons, Phys. Rev. B **51**, 1425–1434 (1995).
25. J. Sipe, J. Opt. Soc. Am. B **4**, 481–498 (1987).
26. M. Zdanowicz, J. Harra, J. M. Makela, E. Heinonen, T. Ning, M. Kauranen, and G. Genty, Sci. Rep. **4**, 5745 (2014).
27. S. Clemmen, A. Hermans, E. Solano, J. Dendooven, K. Koskinen, M. Kauranen, E. Brainis, C. Detavernier, and R. Baets, Opt. Lett. **40**, 5371–5374 (2015).
28. F. Rodriguez, F. Wang, and M. Kauranen, Opt. Express **16**, 8704–8710 (2008).

Publication IV

Enhancement of bulk second-harmonic generation from silicon nitride films by material composition

Kalle Koskinen, Robert Czaplicki, Abdallah Slablab, Tingyin Ning, Artur Hermans, Bart Kuyken, Vinita Mittal, Ganapathy Senthil Murugan, Tapio Niemi, Roel Baets and Martti Kauranen

Optics Letters **42**, 5030-5033 (2017)
© 2017 Optical Society of America.
Reprinted with permission.

Enhancement of bulk second-harmonic generation from silicon nitride films by material composition

K. KOSKINEN,[1,*] R. CZAPLICKI,[1] A. SLABLAB,[1] T. NING,[2] A. HERMANS,[3,4] B. KUYKEN,[3,4] V. MITTAL,[5] G. S. MURUGAN,[5] T. NIEMI,[1] R. BAETS,[3,4] AND M. KAURANEN[1]

[1]*Laboratory of Photonics, Tampere University of Technology, 33101 Tampere, Finland*
[2]*School of Physics and Electronics, Shandong Normal University, Jinan, Shandong 250014, China*
[3]*Photonics Research Group, INTEC Department, Ghent University-imec, Ghent, Belgium*
[4]*Center for Nano- and Biophotonics, Ghent University, Technologiepark-Zwijnaarde 15, 9052 Ghent, Belgium*
[5]*Optoelectronics Research Center, University of Southampton, Southampton SO17 1BJ, United Kingdom*
**Corresponding author: kalle.o.koskinen@tut.fi*

Received 26 September 2017; revised 1 November 2017; accepted 5 November 2017; posted 7 November 2017 (Doc. ID 307991); published 1 December 2017

We present a comprehensive tensorial characterization of second-harmonic generation from silicon nitride films with varying composition. The samples were fabricated using plasma-enhanced chemical vapor deposition, and the material composition was varied by the reactive gas mixture in the process. We found a six-fold enhancement between the lowest and highest second-order susceptibility, with the highest value of approximately 5 pm/V from the most silicon-rich sample. Moreover, the optical losses were found to be sufficiently small (below 6 dB/cm) for applications. The tensorial results show that all samples retain in-plane isotropy independent of silicon content, highlighting the controllability of the fabrication process. © 2017 Optical Society of America

OCIS codes: *(190.0190) Nonlinear optics; (190.4400) Nonlinear optics, materials; (310.6860) Thin films, optical properties.*

http://dx.doi org/10.1364/OL.99 099999

High-performance complementary metal oxide semiconductor (CMOS) compatible materials are essential elements for advanced on-chip photonic devices to realize the future progress in all-optical processing. The ultra-fast speed and high bandwidth of integrated photonic networks continuously require new materials possessing excellent linear and nonlinear optical properties [1, 2]. Although silicon (Si) is still the most commonly used CMOS material, the intrinsic drawbacks of Si, such as its narrow bandgap and centro-symmetric structure highly limit its future applications especially in the visible and ultraviolet spectral regimes [2, 3]. Thus, exploring novel CMOS-compatible materials with wide bandgap and strong optical nonlinearities is very important for future integrated devices.

Many photonic applications rely on nonlinear optical effects. One of the limitations of many nonlinear materials for CMOS-compatible platforms is the lack of second-order nonlinearity due to centrosymmetry. The problem can be overcome by poling [4, 5], straining the material [3] or by using multilayer composites [6-8]. Unexpectedly, CMOS-compatible amorphous silicon nitride films (SiN) have been shown to possess a bulk second-order nonlinearity by measuring strong second-harmonic generation (SHG) from thin films [9-11]. Although the exact reason for this strong SHG response remains unclear, it is believed that the complicated composition, crystalline phase and defects in the film during the deposition may be responsible [10, 12-16].

In this Letter, we show that the strong second-harmonic signal from SiN films can be further enhanced by varying the composition of the films prepared with plasma-enhanced chemical vapor deposition (PECVD). Furthermore, we demonstrate that such composition tuning does not compromise the linear optical properties or optical losses of the material for applications. Our results are crucial for the comprehensive understanding of the linear and nonlinear optical properties in SiN films with different structures, opening the path for further optimization of SiN for on-chip devices.

We recognize that there have been previous studies yielding different values for the SHG susceptibility of SiN [9, 10, 11, 17, 18]. Samples prepared by sputtering can yield very high values of the susceptibility. Unfortunately, the susceptibility value depends extremely sensitively on material composition [9] or the samples possess varying symmetry [11]. These results suggest that the sputtering process can be poorly controlled. In contrast, our PECVD process is consistent, maintaining sample isotropy about the surface normal [10, 17, 19]. PECVD is also compatible with the thermal budget of finished CMOS-circuits. Sample composition is also an important parameter for electric-field-enhanced SHG [18], but this preliminary study reported only a scalar value for the susceptibility. Our tensorial results, obtained through a very advanced model, combined with loss measurements are thus crucial in addressing the suitability of SiN in various photonic applications.

SiN films of thicknesses of approximately 500 nm and of different compositions were grown on fused silica substrates using the PECVD technique. Four samples (S10, S20, S30 and S40) were fabricated in the Laboratory of Photonics (Tampere University of Technology) with the reactive gas mixture of 2% SiH_4/N_2 and NH_3, process pressure of 1000 mTorr, and deposition temperature of 300°C (Plasmalab 80 plus, Oxford Instruments). For these four samples, the plasma was generated using a RF field with frequency of 13.56 MHz and power of 20 W. The material composition of the samples was controlled by adjusting the flow rate of NH_3 (10, 20, 30 and 40 sccm for samples labeled S10, S20, S30 and S40, respectively) while simultaneously applying a constant flow rate of 2% SiH_4/N_2 of 1000 sccm. In order to further address the role of the fabrication procedure, we prepared one additional sample (S35, 35 sccm of NH_3) with PECVD (Advanced Vacuum Vision 310 PECVD) at Ghent University-imec using a gas mixture of SiH_4 (40 sccm), NH_3 (35 sccm) and N_2 (1960 sccm) under deposition temperature of 270°C and process pressure of 650 mTorr. For the S35 sample, the plasma was generated using an exciting field alternating between one second period of high frequency field (13.73 MHz, 30 W) and five second period of low frequency field (~100-300 kHz, 50 W). We also addressed a SiN thin film fabricated using low pressure chemical vapor deposition (LPCVD). However, the SHG response from the LPCVD sample was found to be extremely weak and it will not be discussed any further here.

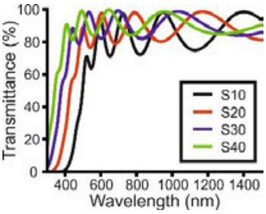

Fig. 1. Normalized transmittance spectra of samples with different compositions.

The fabricated samples were characterized by linear optical spectroscopy (UV-VIS-NIR spectrophotometer, Shimadzu UV-3600) for wavelengths from 300 nm to 1500 nm (Fig. 1). As the silicon content increases (with the lower flow rate of NH_3), the transmittance threshold shifts towards shorter wavelengths in good agreement with previous studies [9]. The oscillatory behavior of the transmittance at longer wavelengths can be ascribed to interference between beams reflected at the interfaces of the SiN film. The optical bandgap energies were estimated from a Tauc plot (not shown) to be between ~3 and ~2 eV from the least to the most silicon rich sample.

The wavelength dependent refractive index and thickness of the samples were determined by ellipsometric measurements. The real and imaginary parts of the refractive index are shown in Figs. 2(a) and 2(b), respectively. The refractive indices at the fundamental and second-harmonic wavelengths as well as film thicknesses are shown in Table 1 for all of the studied samples.

Table 1. Thicknesses and refractive indices at fundamental (n) and second-harmonic (N) wavelengths from ellipsometric measurements. The number in the sample name refers to NH_3 sccm, as described in the text.

sample	thickness [nm]	n @ 1064 nm	N @ 532 nm
S10	662	2.174+0.002i	2.354+0.022i
S20	604	2.005+0.000i	2.099+0.007i
S30	537	1.945+0.000i	1.989+0.002i
S35	500	1.969+0.000i	2.027+0.002i
S40	505	1.902+0.000i	1.951+0.001i

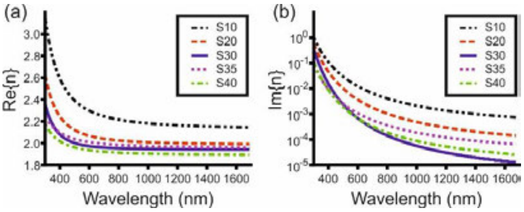

Fig. 2. Real (a) and imaginary (b) parts of refractive indices of the studied SiN thin films with different compositions.

To assess the potential of SiN for applications, we carried out optical loss measurements for all samples at the 633 nm and 1550 nm wavelengths. All samples were found to exhibit losses of less than 6 dB/cm, decreasing further below 3 dB/cm for samples S10 and S20, which is in line with the values previously reported for SiN [20].

The nonlinear measurements were conducted using the setup described in [10]. A mode-locked Nd:YAG laser with a wavelength of 1064 nm, pulse duration of 70 ps, and repetition rate of 1 kHz was used as the source of fundamental light. The spot diameter at the sample was estimated to be a few hundred micrometers. The polarization state of the fundamental beam was controlled with a high-quality polarizer and a motorized quarter-wave plate (QWP). The polarization of the detected SHG signal was selected using another polarizer in front of a photomultiplier tube.

In order to characterize the nonlinear susceptibility, we first illuminated the film at an oblique incidence and studied the polarization signatures of the SHG process for four different polarization controlled measurements. This method is known to uniquely address the relative values of the non-vanishing SHG susceptibility tensor components for samples of $C_{\infty v}$ symmetry [21-23], which is compatible with the known structure for SiN films fabricated using PECVD [10]. Subsequently, we carried out a fifth measurement for fixed polarization states of the incident beam and detected SHG while varying the angle of incidence, followed by a reference measurement from a quartz plate with a known SHG susceptibility to calibrate the value of a single tensor component in absolute units. By combining these two sets of experiments, the values of all nonvanishing SHG susceptibility tensor components can be determined.

For the polarization measurements, we write the SHG field outside the sample as [24]

$$\mathbf{E}_{\mathrm{SHG}} = \hat{\mathbf{P}} f^{p}\left(e^{p}\right)^{2} + \hat{\mathbf{P}} g^{p}\left(e^{s}\right)^{2} + \hat{\mathbf{S}} h^{s} e^{p} e^{s}, \tag{1}$$

where $\hat{\mathbf{P}}$ ($\hat{\mathbf{S}}$) is the unit vector of the polarization components of the SHG field parallel (perpendicular) to the plane of incidence, e^{p} (e^{s}) is the amplitude of the polarization component of the fundamental field parallel (perpendicular) to the plane of incidence evaluated prior to the sample, and f^{p}, g^{p}, and h^{s} are auxiliary expansion coefficients describing the polarization signatures of the SHG response.

The expansion coefficients f^{p}, g^{p}, and h^{s} have been previously shown to be linear combinations of the non-vanishing SHG susceptibility tensor components, which for samples of $C_{\infty v}$ symmetry are $\chi_{xxz} = \chi_{xzx} = \chi_{yyz} = \chi_{yzy}$, $\chi_{zxx} = \chi_{zyy}$, and χ_{zzz} [22], where *z* is the sample normal and *x*, *y* are the two orthogonal in-plane directions [23]. However, it was recently discovered that in order to properly characterize a film with thickness much smaller than the spot size of the fundamental beam, effects arising from multiple reflections within the films can significantly influence the final results [25]. Thus, we utilize a complete model based on the Green's function formalism for nonlinear optics, which includes all effects arising from reflections [26]. Even in this case, the expansion coefficients can be written as functions of the SHG tensor components as

$$\begin{bmatrix} f^{p} \\ g^{p} \\ h^{s} \end{bmatrix} = M \begin{bmatrix} \chi_{xxz} \\ \chi_{zxx} \\ \chi_{zzz} \end{bmatrix}, \tag{2}$$

where the matrix M depends only on the experimental geometry and the linear material parameters of the nonlinear film and the substrate. The evaluation of M is a straightforward process but requires arduous calculus, and its full description is omitted due to the extreme length of the mathematical expressions.

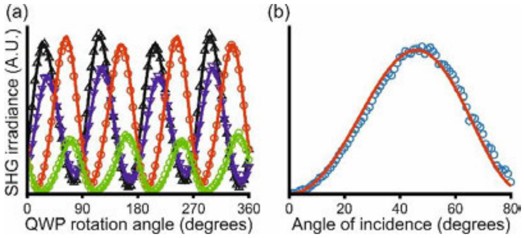

Fig. 3. (a) Experimental data (markers) from polarization controlled SHG (black: *p*+*s* in, *p* out; blue: *p*+*s* in, *p*+*s* out; red: *p*-*s* in, *p* out; green: *p*-*s* in, *p*+*s* out) for sample S30 and analytical fits (lines) to the tensor components. (b) Experimental data of *p*-polarized SHG signal arising from sample S30 with *s*-polarized input versus angle of incidence from the calibration experiment (blue circles) and analytical fit (red line). Similar results were obtained for samples S10, S20, S35 and S40.

To probe the polarization signatures of the SHG process, we chose the four different combinations of polarizations for the detected SHG beam and the initial fundamental beam incident to the QWP to be the same as in [10] and an angle of incidence of 60°. The results from all four measurements were simultaneously fitted for relative values of χ_{xxz}, χ_{zxx} and χ_{zzz} and are shown in Fig. 3(a) for the S30 sample. The absolute values of the SHG susceptibility were determined by comparing an angle of incidence controlled calibration measurement of *p*-polarized SHG generated from *s*-polarized input to a measurement from ~1 mm thick Y-cut quartz crystal wedge plate with a known SHG susceptibility of $\chi_{xxx}^{\mathrm{Q}} = 0.80\ \mathrm{pm/V}$ [(Fig. 3(b)] [27]. Note also the lack of interference fringes in the angle of incidence controlled measurements [Fig. 3(b)], confirming that the SHG is indeed of bulk origin. If that were not the case, the surface SHG signal from SiN would have to be multiple orders of magnitude higher than that of the substrate back-surface, which is implausible. Similar behavior was observed for all samples.

The determined values of the SHG susceptibility tensor components of the SiN films of varying composition are shown in Table 2. Our results show that the second-order response can be greatly enhanced by adjusting the flow rate of NH_3 during the PECVD fabrication process, showcasing the tunable nature of SiN as a material. Furthermore, the highest bulk-susceptibility of the studied SiN compositions (sample S10) was found to be about 5 pm/V, which is a reasonable value for potential applications. Another interesting result was the discrepancy between the determined susceptibility for S30 sample (for example, $\chi_{zzz} = 1.10\ \mathrm{pm/V}$) and the value previously reported for a SiN film prepared under identical conditions ($\chi_{zzz} = 2.47\ \mathrm{pm/V}$) [10]. We believe that the difference is due to our present analysis being based on a more advanced model taking reflection effects into account for all experiments, whereas the analysis reported in [10] was based on a simpler approach. This result further highlights the crucial role of a sufficiently detailed model in the nonlinear characterization of thin films.

Note also that the results for the silicon poor samples (S40 and S35) essentially fulfill the Kleinman symmetry $\chi_{xxz} = \chi_{zxx}$, as expected for non-resonant nonlinearity, whereas the silicon-richer samples (S30, S20, and S10) start deviating from this symmetry as the resonance for the second-harmonic wavelength is approached (see Fig. 1).

The results also show that the nonlinear response depends sensitively on the fabrication conditions as the sample S35, fabricated at Ghent University, deviates from the general trend of the remaining samples, fabricated at Tampere University of Technology.

Table 2. The calibrated values of second-order susceptibility tensor components of the studied SiN thin films with different compositions.

sample	χ_{zzz} [pm/V]	χ_{xxz} [pm/V]	χ_{zxx} [pm/V]
S10	5.10	1.60	1.40
S20	1.70	0.87	0.72
S30	1.10	0.40	0.34
S35	0.66	0.20	0.21
S40	0.80	0.23	0.22

In conclusion, we have conducted a comprehensive analysis using a detailed analytical model of the SHG response from SiN thin films fabricated using the PECVD method in order to study the dependence of the response on material composition and to determine the optimal composition for nonlinear photonic applications. We have done so by studying five different samples fabricated in two different laboratories with varying fabrication parameters resulting in varying material composition.

Our results show that silicon nitride can be optimized for efficient bulk-type second-harmonic generation response through the material composition at least by a factor of 6 in terms of susceptibility. The value of the highest susceptibility component was found to be approximately 5 pm/V corresponding to the most silicon-rich sample, a number that is comparable to that of traditional nonlinear crystals. Furthermore, the optical losses were found to be sufficiently low for viable applications. We believe that our results, combined with favorable linear properties as well as CMOS–compatibility of SiN, further open the path towards using SiN in a variety of new nonlinear optical applications.

Funding. Academy of Finland (265682). K.K. acknowledges the Vilho, Yrjö and Kalle Väisälä Foundation for a personal fellowship. A.H. acknowledges the Research Foundation – Flanders (FWO) for personal fellowship.

References

1. J. Leuthold, C. Koos, and W. Freude, Nat. Photon. **4**, 535 (2010).
2. J. S. Levy, A. Gondarenko, M. A. Foster, A. C. Turner-Foster, A. L. Gaeta, and M. Lipson, Nat. Photon. **4**, 37 (2010).
3. M. Cazzanelli, F. Bianco, E. Borga, G. Pucker, M. Ghulinyan, E. Degoli, E. Luppi, V. Véniard, S. Ossicini, D. Modotto, S. Wabnitz, R. Pierobon, and L. Pavesi, Nat. Mater. **11**, 148 (2012).
4. R. A. Myers, N. Mukherjee, and S. R. J. Brueck, Opt. Lett. **16**, 1732 (1991).
5. T.-D. Kim, J. Luo, J.-W. Ka, S. Hau, Y. Tian, Z. Shi, N. Tucker, S.-H. Jang, J.-W. Kang, and A.-Y. Jen, Adv. Mater. **18**, 3038 (2006).
6. L. Alloatti, C. Kieninger, A. Froelich, M. Lauermann, T. Frenzel, K. Köhnle, W. Freude, J. Leuthold, M. Wegener, and C. Koos, Appl. Phys. Lett. **107**, 121903 (2015).
7. S. Clemmen, A. Hermans, E. Solano, J. Dendooven, K. Koskinen, M. Kauranen, E. Brainis, C. Detavernier, and R. Baets, Opt. Lett. **40**, 5371 (2015).
8. M. Zdanowicz, J. Harra, J. M. Makela, E. Heinonen, T. Ning, M. Kauranen, and G. Genty, Sci. Rep. **4**, 5745 (2014).
9. A. Kitao, K. Imakita, I. Kawamura, and M. Fujii, J. Phys. D: Appl. Phys. **47**, 215101 (2014).
10. T. Ning, H. Pietarinen, O. Hyvärinen, J. Simonen, G. Genty, and M. Kauranen, Appl. Phys. Lett. **100**, 161902 (2012).
11. E. F. Pecora, A. Capretti, G. Miano, and L. Dal Negro, Appl. Phys. Lett. **102**, 141114 (2013).
12. C. Di Valentin, G. Palma, and G. Pacchioni, J. Phys. Chem. C **115**, 561 (2011).
13. M. Ippolito and S. Meloni, Phys. Rev. B **83**, 165209 (2011).
14. S. Lettieri, S. Di Finizio, P. Maddalena, V. Ballarini, and F. Giorgis, Appl. Phys. Lett. **81**, 4706 (2002).
15. S. Minissale, S. Yerci, and L. Dal Negro, Appl. Phys. Lett. **100**, 021109 (2012).
16. M. H. Nayfeh, N. Rigakis, and Z. Yamani, Phys. Rev. B **56**, 2079 (1997).
17. M. W. Puckett, R. Sharma, H.-H. Lin, M. han Yang, F. Vallini, and Y. Fainman, Opt. Express **24**, 16923 (2016).
18. H.-H. Lin, R. Sharma, M.-H. Yang, M. W. Puckett, C. D. Wurm, F. Vallini, and Y. Fainman, in *Conference on Lasers and Electro-Optics* (Optical Society of America, 2017), p. SM1M.6.
19. T. Ning, H. Pietarinen, O. Hyvärinen, R. Kumar, T. Kaplas, M. Kauranen, and G. Genty, Opt. Lett. **37**, 4269 (2012).
20. A. Z. Subramanian, P. Neutens, A. Dhakal, R. Jansen, T. Claes, X. Rottenberg, F. Peyskens, S. Selvaraja, P. Helin, B. D. Bois, K. Leyssens, S. Severi, P. Deshpande, R. Baets, and P. V. Dorpe, IEEE Photon. J. **5**, 2202809 (2013).
21. J. Maki, M. Kauranen, T. Verbiest, and A. Persoons, Phys. Rev. B **55**, 5021 (1997).
22. F. J. Rodriguez, F. X. Wang, and M. Kauranen, Opt. Express **16**, 8704 (2008).
23. F. Wang, M. Siltanen, and M. Kauranen, Phys. Rev. B **76**, 085428 (2007).
24. M. Kauranen, T. Verbiest, J. Maki, and A. Persoons, J. Chem. Phys. **101**, 8193 (1994).
25. K. Koskinen, R. Czaplicki, T. Kaplas, and M. Kauranen, Opt. Express **24**, 4972 (2016).
26. J. Sipe, J. Opt. Soc. Am. B **4**, 481–498 (1987).
27. R. W. Boyd, *Nonlinear Optics* (Academic Press, 2003)

Publication V

Nonresonant local fields enhance second-harmonic generation from metal nanoislands with dielectric cover

Semyon Chervinskii, Kalle Koskinen, Sergey Scherbak, Martti Kauranen and Andrey Lipovskii

Physical Review Letters **120**, 113902 (2018)
© 2018 American Physical Society.
Reprinted with permission.

PHYSICAL REVIEW LETTERS **120,** 113902 (2018)

Editors' Suggestion

Nonresonant Local Fields Enhance Second-Harmonic Generation from Metal Nanoislands with Dielectric Cover

Semyon Chervinskii,[1,2,*] Kalle Koskinen,[3] Sergey Scherbak,[1,4] Martti Kauranen,[3] and Andrey Lipovskii[1,4]
[1]*Institute of Physics, Nanotechnology and Telecommunication, Peter the Great St. Petersburg Polytechnic University,*
Polytechnicheskaya 29, St. Petersburg, 195251 Russia
[2]*Institute of Photonics, University of Eastern Finland, P.O. Box 111, FI-80101 Joensuu, Finland*
[3]*Laboratory of Photonics, Tampere University of Technology, P.O. Box 692, FI-33101 Tampere, Finland*
[4]*Department of Physics and Technology of Nanostructures, St. Petersburg Academic University,*
Khlopina 8/3, St. Petersburg, 194021 Russia

(Received 13 October 2017; published 15 March 2018)

We study second harmonic generation from gold nanoislands covered with amorphous titanium oxide (TiO_2) films. As the TiO_2 thickness increases, the plasmon resonance of the nanoislands shifts away from the second harmonic wavelength of 532 nm, diminishing the resonant enhancement of the process at this wavelength. Nevertheless, the second harmonic signal is enhanced by up to a factor of 45 with increasing TiO_2 thickness. This unexpected effect arises from the scaling of local fields at the fundamental wavelength of 1064 nm which is at the far tail of the resonance due to a change in the dielectric environment of the nanoislands.

DOI: 10.1103/PhysRevLett.120.113902

The optical properties of metal nanoparticles arise from their localized surface plasmon resonances (LSPRs). Such resonances give rise to strongly enhanced local fields (LFs) near the metal dielectric interfaces, advantageous, e.g., for catalytic activity [1], optical absorption and emission [2,3], or Raman scattering [4]. The enhancement is particularly interesting for nonlinear optical processes, which scale with a high power of the optical field [5]. For the particular case of second harmonic generation (SHG), several studies have addressed plasmon resonances at the fundamental [6,7] and second harmonic [8 11] wavelengths as well as their interplay with symmetry rules and local field distributions [8,12 17].

The spectral positions of LSPRs depend on the dielectric environment of the metal particles, which forms the basis for plasmonic sensors [18]. When the particles are covered with a dielectric film of increasing thickness, the spectrum shifts gradually and saturates only when the evanescent tails of the LFs are fully embedded in the dielectric. This can be qualitatively understood by treating thin dielectric films as bulk media with reduced effective permittivity, which grows with the film thickness until the bulk value is reached. The associated spectral shift occurs in parallel with growing particle polarizability and, respectively, the LF at the resonant frequency. Far less known is that the modified LFs are not limited to plasmon resonances. In fact, the dielectric loading increases the particle polarizability, thereby scaling the LFs even when the wavelength is far from the plasmon resonance, providing unexplored opportunities for nanophotonics.

In this Letter, we demonstrate the usefulness of such nonresonant LFs in nonlinear optics. More specifically, we use SHG with the fundamental wavelength of 1064 nm to investigate gold nanoisland films with plasmon resonance at about 520 nm. This is close to the second harmonic (SH) wavelength of 532 nm, and the process is, therefore, resonantly enhanced at the SH but not at the fundamental wavelength. We then use atomic layer deposition (ALD) to cover the nanoislands with amorphous titanium dioxide (TiO_2) films of increasing thickness. This shifts the plasmon resonance away from the SH wavelength, thereby decreasing the resonance enhancement. Nevertheless, the SH signal from coated nanoislands increases by a factor of 45 with the TiO_2 thickness, while TiO_2 films on silica without nanoislands do not exhibit any remarkable nonlinearity. The increase is well explained by the scaling of the LFs at the fundamental wavelength associated with the increased dielectric loading due to the TiO_2 film.

Our gold nanoisland films were prepared by air annealing of gold films deposited onto fused silica substrates by evaporation. The resulting films were comprised of separate nanoislands of 10 20 nm in size (Fig. 1 inset) [19]. The details related to the preparation of the samples and measurements are presented in the Supplemental Material [20]. The nanoisland films were coated with TiO_2 films of varying thickness (about 3 100 nm) by ALD. Ellipsometric analysis of similar TiO_2 films on substrates without nanoislands showed that their refractive indices varied by about 10% depending on film thickness, probably due to densification of the thickest film in the long

© 2018 American Physical Society

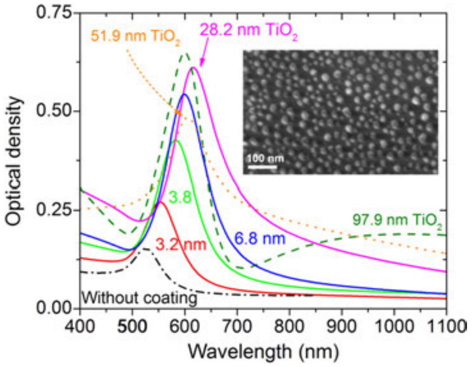

FIG. 1. Absorption spectra of the samples with gold nanoisland film coated with TiO$_2$ layers of different thicknesses (indicated near the curves). The spectra of the 51.9 and 97.9 nm samples, which demonstrate irregularities, are dotted and dashed, respectively. Inset: SEM image of the nanoisland film.

ALD process. These differences have no influence on the main results of our work.

The optical spectra of the nanoisland films covered with TiO$_2$ layers of different thicknesses (Fig. 1) show that the LSPR peak shifts toward longer wavelengths, as known for covered nanoparticles [24–26]. Additionally, the peak becomes more intense with increasing TiO$_2$ thickness. Both trends saturate after the thickness of about 30 nm when the electric field of the plasmon is completely inside the covering layer [19]. The peak growth is similar to that of metal nanoparticles when they are embedded in more polarizable media [23,27], and this behavior is theoretically well understood [28]. For the two samples with TiO$_2$ thickness exceeding 30 nm (51.9 and 97.9 nm), the spectra exhibit some irregularities compared to the monotonic trend for thinner TiO$_2$ films. We relate these irregularities to the very long ALD times of the thickest covers, which could influence the size of the gold nanoislands, and interference effects within the thickest TiO$_2$ films. Nevertheless, even in these cases, saturation of both the spectral shift and the absorption peak is evident.

The SHG responses of bare TiO$_2$ films and TiO$_2$ covered gold nanoisland samples with different TiO$_2$ thicknesses were characterized using the Maker fringe technique [29]. A laser with 70 ps pulses at 1064 nm was used as the source of fundamental light [20,30]. Both the fundamental and SH beams were *p* polarized, which typically gives rise to the strongest SH signals. The experiments result in interference fringes between the SH signals from the sample and the back surface of the substrate as the incident angle is varied, as detailed in the Supplemental Material [20]. Representative Maker fringes from our samples are shown in the Fig. 2 inset, where the SH response increases by a factor of 45 with increasing TiO$_2$ thickness. We emphasize that the SH signals from bare TiO$_2$ films of any thickness were about the same and comparable to the signal from the silica substrate, approximately 80 times weaker than the signal from gold nanoislands with no TiO$_2$ coating. This proves that the TiO$_2$ films are amorphous as expected from ALD [31].

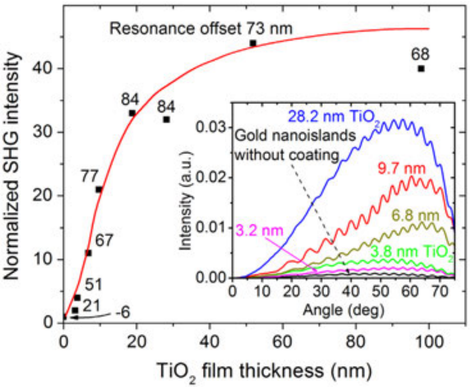

FIG. 2. SH response from gold nanoisland films coated with TiO$_2$ layers as a function of the TiO$_2$ layer thickness. The resonance offsets $\Delta\lambda$ (nm) between the LSPR and SH wavelength are indicated near the corresponding data markers. The SH intensity is normalized by the SH signal from the nanoisland film without the TiO$_2$ cover. The line is a guide for the eye only. Inset: SHG Maker fringe patterns from representative samples.

The dependence of SHG from gold nanoisland films on TiO$_2$ thickness is shown in Fig. 2. The signal is normalized to that from the nanoisland film without cover. The SH signal saturates at about 30 nm film thickness, near the range where the LSPR spectral shift saturates [19]. Importantly, the SH response grows with the TiO$_2$ thickness despite the detuning $\Delta\lambda = \lambda_{\mathrm{LSPR}} - 532$ nm of the LSPR wavelength from the SH wavelength (532 nm); see the magnitudes of the resonance offset indicated near the data markers in Fig. 2. A small decrease in the SH signal for the thickest TiO$_2$ cover is probably related to the effect of the temperature on the gold nanoparticles in the long ALD process.

Physical insight into the observed effects can be obtained by considering the polarizability of a spherical particle of radius R [32],

$$\alpha = R^3 \frac{\varepsilon_{\mathrm{me}} - \varepsilon_{\mathrm{out}}}{\varepsilon_{\mathrm{me}} + 2\varepsilon_{\mathrm{out}}} = R^3 \frac{(\varepsilon_{\mathrm{me}} + 2\varepsilon_{\mathrm{out}}) - 3\varepsilon_{\mathrm{out}}}{\varepsilon_{\mathrm{me}} + 2\varepsilon_{\mathrm{out}}}, \qquad (1)$$

where $\varepsilon_{\mathrm{me}}$ is the permittivity for the metal and $\varepsilon_{\mathrm{out}}$ that for the embedding medium. By assuming that $\varepsilon_{\mathrm{out}}$ is real and by separating $\varepsilon_{\mathrm{me}}$ into its real and imaginary parts $\varepsilon_{\mathrm{me}} = \varepsilon'_{\mathrm{me}} + i\varepsilon''_{\mathrm{me}}$, it is evident that the polarizability exhibits a resonance when $\varepsilon'_{\mathrm{me}} = -2\varepsilon_{\mathrm{out}}$. The absorption cross section of the particles, which is of interest here, depends on the imaginary part of the polarizability

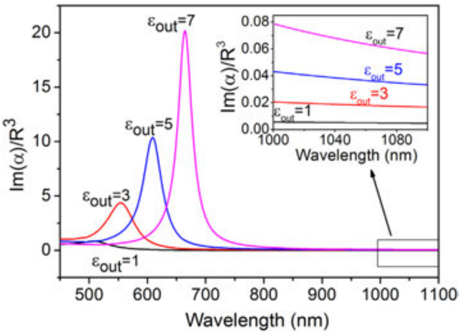

FIG. 3. Influence of outer medium permittivity ($\varepsilon_{\mathrm{out}}$) on the dispersion of the imaginary part of the polarizability of a spherical gold nanoparticle of radius R.

[$\sigma^{\mathrm{abs}} \propto \mathrm{Im}(\alpha)$] [33]. The imaginary part of the resonant polarizability is, thus,

$$\mathrm{Im}(\alpha_{\mathrm{res}}) \quad 3R^3 \frac{\varepsilon_{\mathrm{out}}}{\varepsilon''_{\mathrm{me}}}; \tag{2}$$

i.e., it is proportional to the permittivity of the outer medium. The real part $\varepsilon'_{\mathrm{me}}$ for metals becomes more negative with increasing wavelength. By then treating the layer of the embedding medium by effective permittivity, which increases with film thickness, it becomes clear that the resonance shifts to longer wavelengths and becomes more intense as the layer thickness increases. Note that the imaginary part $\varepsilon''_{\mathrm{me}}$ for metals is assumed to be small, which allowed neglecting the real part of the resonant polarizability.

It is less evident, however, that this thickness dependent scaling is not limited to the line center of LSPR. Equation (1) typically leads to a Lorentzian line shape. If its linewidth does not change much with the thickness of the outer medium, the tails of the LSPR must increase in the same proportion as at the line center. We applied this simple model for small gold spheres using the Johnson Christy data [34] for the permittivity of gold. The results are illustrated in Fig. 3 for the imaginary part of the polarizability. When the effective permittivity is increased, the resonance shifts and becomes more intense, as observed experimentally (Fig. 1). Furthermore, the increase also affects the tails of the LSPR, reaching the fundamental wavelength of the laser. Finally, similar effects occur also for the real part of the polarizability. The changes in the LFs arise from both the real and imaginary parts of the polarizability and are, therefore, fully carried through to the tails of the resonance.

For a more detailed treatment of the observed effects, we need both the linear polarizability of the gold nanoparticles and the local field factors (LFFs) near the particles. For this, we use an approach [19,35] where the polarizability and corresponding electric potential of a truncated nanosphere on a substrate [see Fig. 4(a)] are calculated in quasistatic approximation. In the following, we present the results for the case where the field is polarized along the glass surface. The normal polarization components are known to exhibit similar behavior albeit scaled by a factor that depends on the truncation angle [36].

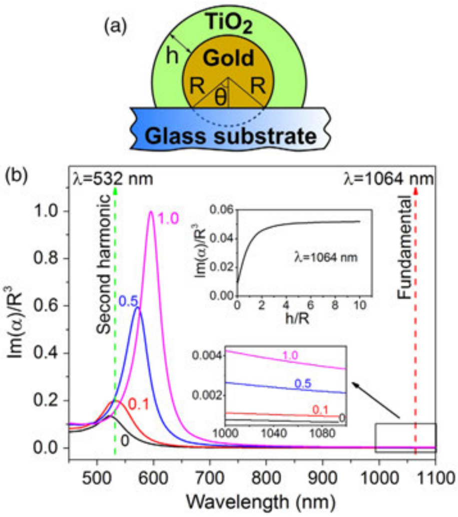

FIG. 4. (a) Schematic of a truncated gold nanosphere on a glass substrate and covered with a TiO$_2$ layer, θ truncation angle. (b) Influence of the TiO$_2$ ($\varepsilon_{\mathrm{coat}}$ 5.5) cover of different thickness (h) on the imaginary part of the polarizability of a truncated gold sphere (truncation angle ~50°) of radius R placed on a substrate with $\varepsilon_{\mathrm{sub}}$ 2.25; the h/R ratio is labeled near the curves. Inset: Polarizability at the fundamental wavelength 1064 nm vs the h/R ratio. Dispersions of the substrate and the cover are neglected.

We applied this model to small gold nanoparticles with radius R by using the Johnson Christy data for the permittivity of gold [34]. The truncation angle was taken to be θ 50° [Fig. 4(a)]. The permittivity of TiO$_2$ was taken to be $\varepsilon_{\mathrm{coat}}$ 5.5 and its thickness h was varied. The permittivity of the glass substrate was taken to be $\varepsilon_{\mathrm{sub}}$ 2.25. The absorption spectrum [Fig. 4(b)] is seen to depend on the ratio h/R.

The general behavior again follows that of the absorption presented in Fig. 1. The LSPR is seen to shift toward longer wavelengths and become more intense with increasing cover thickness. The shift has been discussed elsewhere [19,37], while not much attention has been paid to the growth in polarizability [38]. A key difference between the experiments and simulations is that the latter exhibit higher LSPR quality factors. This is because the simulations did not account for deviations in the size and shape of the particles in the real samples or for the mutual interaction between the particles. The trend in the polarizability is similar to the one for spherical particles in a medium with effective polarizability (Fig. 3). The polarizability at our fundamental wavelength, i.e., the far tail of the LSPR, grows rapidly with the TiO_2 cover thickness and starts saturating at the ratio h/R of about 3 [inset of Fig. 4(b)]. For our nanoisland samples with average radius of ~9 nm, this corresponds to ~30 nm thick TiO_2 cover, in very good agreement with the experiment (Fig. 1 inset).

We next apply this model to interpret our experimental results for SHG. For this, we need the LFFs at the fundamental and SH wavelengths. For nanoparticles, the LFFs are space dependent, describing the redistribution of optical energy to "hot spots," and tensorial, because the LFs can contain polarization components not present in the incident field. Keeping these limitations in mind, the source polarization for SHG can be written as [39]

$$P_{2\omega} = \chi^{(2)}_{\mathrm{eff}} L_{2\omega} L^2_{\omega} E^2_{0\omega}, \tag{3}$$

where $\chi^{(2)}_{\mathrm{eff}}$ is the effective second order susceptibility, L_ω and $L_{2\omega}$ are the LFFs at the fundamental and SH frequencies, respectively, and $E_{0\omega}$ is the incident field at the fundamental frequency. Thus, the SHG intensity depends on the LFFs as

$$I_{\mathrm{SHG}} \propto L^2_{2\omega} L^4_{\omega}. \tag{4}$$

It is crucial that the dependence at the fundamental frequency is to the fourth power and at the SH frequency, it is to the second power.

The application of Eqs. (3) and (4) depends greatly on how the effective susceptibility $\chi^{(2)}_{\mathrm{eff}}$ is chosen. We assume that the SH response arises from the surface nonlinearity of the gold particles and that the dominant tensor component of the surface susceptibility is $\chi^{(2)}_{S,\perp\perp\perp}$, where $\perp$ refers to the normal component, as justified in a number of works [40–42]. This local response, thus, needs to be integrated over the shape of the nanoparticle. Therefore, the LFF for frequency Ω is defined as

$$L^{\perp}_{\Omega} = \frac{\langle |E^{\perp}_{\Omega}(r = R)| \rangle_{\theta,\phi}}{|E^0_{\Omega}|}, \tag{5}$$

where E^0_Ω is the incident electric field, $E^{\perp}_{\Omega}(r = R)$ the local normal component of the field on the particle surface, and $\langle \cdots \rangle_{\theta,\phi}$ denotes angular averaging, with θ and ϕ being spherical coordinates for the truncated nanosphere.

The SH intensity calculated according to Eq. (4) as a function of dielectric coating thickness h for truncated gold nanoparticles of radius R is shown in Fig. 5, while the powers of calculated LFFs L_ω and $L_{2\omega}$ [Eq. (3)] are presented in the inset.

The expected resonant behavior of the LFF at the SHG frequency $L_{2\omega}$ is evident in the inset in Fig. 5. The LSPR passes through the SH wavelength ($\lambda = 532$ nm) for very thin coatings, but this resonance is quickly lost as the coating thickness increases. The fundamental wavelength ($\lambda = 1064$ nm), on the other hand, is at the far tail of the LSPR, and the LFF L_ω monotonically grows with the coating thickness. Obviously, these differences are accentuated for the higher powers of the LFFs. The average particle radius in our case is about 9 nm [19], so the h/R ratio for the maximum cover thickness of 100 nm is about 11. All the LFFs for SHG [Eq. (4)] are combined in Fig. 5. The contribution of the monotonic growth of L_ω is seen to override any resonant features of $L_{2\omega}$. This, of course, arises because the scaling with L_ω is to the fourth power, whereas with $L_{2\omega}$, it is only to the second power.

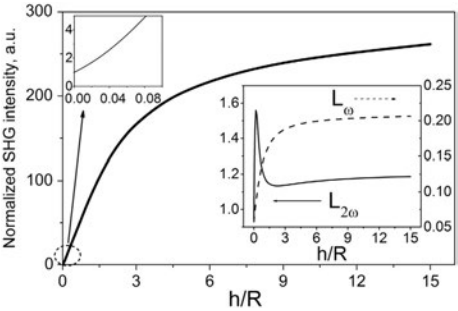

FIG. 5. Calculated SH intensity for truncated spherical gold nanoparticles (50° truncation angle) on a glass surface ($\varepsilon_{\mathrm{sub}} = 2.25$) as a function of the TiO_2 ($\varepsilon_{\mathrm{coat}} = 5.5$) coating thickness. The intensity is normalized by the SH signal from bare gold nanoparticles ($h = 0$). Inset: Calculated LFFs at the fundamental and SH frequencies. Dispersions of the substrate and the cover are neglected.

The qualitative agreement for the SH signal strength between the experimental results (Fig. 2) and theory (Fig. 5) is seen to be very good. The main difference is that the experimental enhancement is about a factor of 45, whereas the theory predicts a factor of 240 for $h/R = 11$. The factor of 5 discrepancy in SH intensity, however, corresponds to only a factor of 1.5 difference in field amplitude. This difference can be, for example, due to the size distribution of the nanoparticles and due to Fresnel reflections at the air–TiO_2 interfaces, which could be remedied by antireflection coatings on the interfaces.

Our results have links to nonlinear composite materials [43,44]. The focus in that area has been on bulk type composite materials with different dielectric properties. In addition, the role of a host material with high permittivity on enhancing nonlinear properties has been emphasized [45]. On the other hand, for metal–dielectric composites, only the role of plasmon resonances is usually considered [46–49]. The present work goes beyond these earlier results by highlighting how systematic variations in the dielectric environment affect the nonlinear responses and how the local field effects at nonresonant wavelengths can completely overrule the role of any resonant effects.

It is evident that the theoretical analysis of the present results can be significantly improved. In particular, we describe the local nonlinearity of the metal dielectric interface by a single component of the susceptibility tensor. By more extensive modeling, additional components could be included, as has been done for nonlinear scattering [42,50] and numerical description of nonlinear metamaterials [41]. A more important future question, however, is to consider how the local field effects influence the overall response of our samples. It is likely that due to the anisotropy of our thin film structure, the local field effects are different for different polarization components of the fundamental and SH beams. Such effect would then influence different tensor components of the sample in different ways, whereas the present results were discussed only in terms of an effective scalar SH susceptibility. However, such additional factors have no influence on the main results of the present Letter.

In conclusion, we showed that covering metal nanoparticles with a dielectric coating allows the efficiency of second harmonic generation to be enhanced, independent of the spectral position of the localized surface plasmon resonance of the particles. The enhancement was observed for gold nanoislands covered with a dielectric layer of amorphous titanium dioxide of varying thickness. We modeled and explained this phenomenon by the growth of the local field factors at the fundamental wavelength. This growth dominates the decrease in the local field factors at the second harmonic wavelength caused by the shift of the plasmon resonance away from the second harmonic wavelength. The importance of the LFFs at the fundamental wavelength over those at the second harmonic wavelength arises because the second harmonic signal is proportional to the second power of the local field factors at the second harmonic wavelength and to the fourth power of those at the fundamental wavelength. We believe that this phenomenon is of great importance and can be observed in a variety of contexts, independent of the particular shape or even size of the nanoparticles. In addition, the effect is not limited to second harmonic generation but should open new opportunities in all cases where the tailoring of the local fields can be used to advantage in photonic applications.

The authors are grateful to Igor Reduto for SEM measurements. S. Ch. is thankful to Niko Penttinen and Pertti Pääkkönen for the introduction to ellipsometry. The study has been supported by Academy of Finland (Grants No. 287651 and No. 309473) and the Russian Ministry for Education and Science Project No. 3.2869.2017. K. K. acknowledges the Vilho, Yrjö, and Kalle Väisälä Foundation for a personal fellowship.

S. Ch., K. K., and S. Sch. contributed equally to this work.

[*] Corresponding author.
semen.chervinskii@uef.fi

[1] E. C. Le Ru and P. G. Etchegoin, *Principles of Surface-Enhanced Raman Spectroscopy* (Elsevier Science, New York, 2009).

[2] V. A. Podolskiy, P. Ginzburg, B. Wells, and A. V. Zayats, Faraday Discuss. **178**, 61 (2015)

[3] M. A. Green and S. Pillai, Nat. Photonics **6**, 130 (2012).

[4] J. N. Anker, W. P. Hall, O. Lyandres, N. C. Shah, J. Zhao, and R. P. Van Duyne, Nat. Mater. **7**, 442 (2008).

[5] M. Kauranen and A. V. Zayats, Nat. Photonics **6**, 737 (2012).

[6] R. Czaplicki, M. Zdanowicz, K. Koskinen, J. Laukkanen, M. Kuittinen, and M. Kauranen, Opt. Express **19**, 26866 (2011).

[7] F. B. P. Niesler, N. Feth, S. Linden, and M. Wegener, Opt. Lett. **36**, 1533 (2011).

[8] K. Thyagarajan, S. Rivier, A. Lovera, and O. J. F. Martin, Opt. Express **20**, 12860 (2012).

[9] M. Celebrano, X. Wu, M. Baselli, S. Großmann, P. Biagioni, A. Locatelli, C. de Angelis, G. Cerullo, R. Osellame, B. Hecht, L. Duò, F. Ciccacci, and M. Finazzi, Nat. Nanotechnol. **10**, 412 (2015).

[10] B. Metzger, L. Gui, J. Fuchs, D. Floess, M. Hentschel, and H. Giessen, Nano Lett. **15**, 3917 (2015).

[11] H. Linnenbank and S. Linden, Optica **2**, 698 (2015).

[12] B. K. Canfield, H. Husu, J. Laukkanen, B. F. Bai, M. Kuittinen, J. Turunen, and M. Kauranen, Nano Lett. **7**, 1251 (2007).

[13] J. Berthelot, G. Bachelier, M. Song, P. Rai, G. Colas des Francs, A. Dereux, and A. Bouhelier, Opt. Express **20**, 10498 (2012).

[14] R. Czaplicki, J. Mäkitalo, R. Siikanen, H. Husu, J. Lehtolahti, M. Kuittinen, and M. Kauranen, Nano Lett. **15**, 530 (2015).

[15] S. D. Gennaro, M. Rahmani, V. Giannini, H. Aouani, T. P. H. Sidiropoulos, M. Navarro Cía, S. A. Maier, and R. F. Oulton, Nano Lett. **16**, 5278 (2016).

[16] S. Viarbitskaya, O. Demichel, B. Cluzel, G. Colas des Francs, and A. Bouhelier, Phys. Rev. Lett. **115**, 197401 (2015).

[17] F. Wang, A. B. F. Martinson, and H. Harutyunyan, ACS Photonics **4**, 1188 (2017).

[18] M. Li, S. K. Cushing, and N. Q. Wu, Analyst **140**, 386 (2015).

[19] S. Scherbak, N. Kapralov, I. Reduto, S. Chervinskii, O. Svirko, and A. A. Lipovskii, Plasmonics **12**, 1903 (2017).

[20] See Supplemental Material at http://link.aps.org/supplemental/10.1103/PhysRevLett.120.113902 which includes Refs. [21 23] for details of the samples preparation and measurements.

[21] B. von Blanckenhagen, D. Tonova, and J. Ullmann, Appl. Opt. **41**, 3137 (2002).

[22] G. E. Jellison and F. A. Modine, Appl. Phys. Lett. **69**, 371 (1996).

[23] H. X. Xu and M. Kall, Sens. Actuators B **87**, 244 (2002).

[24] P. Royer, J. P. Goudonnet, R. J. Warmack, and T. L. Ferrell, Phys. Rev. B **35**, 3753 (1987).

[25] W. Ji Fei, L. Hong Jian, Z. Zi You, L. Xue Yong, L. Ju, and Y. Hai Yan, Chin. Phys. B **19**, 117310 (2010).

[26] J. A. Dieringer, A. D. McFarland, N. C. Shah, D. A. Stuart, A. V. Whitney, C. R. Yonzon, M. A. Young, X. Zhang, and R. P. Van Duyne, Faraday Discuss. **132**, 9 (2006).

[27] T. Okamoto, I. Yamaguchi, and T. Kobayashi, Opt. Lett. **25**, 372 (2000).

[28] V. Klimov, *Nanoplasmonics* (CRC Press, Boca Raton, 2013).

[29] P. D. Maker, R. W. Terhune, M. Nisenhoff, and C. M. Savage, Phys. Rev. Lett. **8**, 21 (1962).

[30] T. Ning, H. Pietarinen, O. Hyvärinen, J. Simonen, G. Genty, and M. Kauranen, Appl. Phys. Lett. **100**, 161902 (2012).

[31] M. R. Saleem, S. Honkanen, and J. Turunen, Appl. Opt. **52**, 422 (2013).

[32] J. D. Jackson, *Classical Electrodynamics*, 3rd ed. (John Wiley & Sons Inc., New York, 1999).

[33] C. F. Bohren and D. R. Huffman, *Absorption and Scattering of Light by Small Particles* (John Wiley & Sons Inc., New York, 1983).

[34] P. Johnson and R. Christy, Phys. Rev. B **6**, 4370 (1972).

[35] M. M. Wind, J. Vlieger, and D. Bedeaux, Physica (Amsterdam) **141A**, 33 (1987).

[36] M. M. Wind, J. Vlieger, and D. Bedeaux, Physica (Amsterdam) **143A**, 164 (1987).

[37] S. Chervinskii, A. Matikainen, A. Dergachev, A. Lipovskii, and S. Honkanen, Nanoscale Res. Lett. **9**, 398 (2014).

[38] V. I. Chegel, V. K. Lytvyn, A. M. Lopatynskyi, P. E. Shepeliavyi, O. S. Lytvyn, and Yu. V. Goltvyanskyi, Semi. Phys. Quant. Electron. Optoelectron. **18**, 272 (2015).

[39] *Plasmonics: Theory, and Applications*, edited by T. V. Shahbazyan and M. I. Stockman (Springer Dordrecht, 2013).

[40] J. Martorell, R. Vilaseca, and R. Corbalan, Phys. Rev. A **55**, 4520 (1997).

[41] J. Mäkitalo, S. Suuriniemi, and M. Kauranen, Opt. Express **19**, 23386 (2011); **21**, 10205 (2013).

[42] J. Dadap, J. Shan, and T. Heinz, J. Opt. Soc. Am. B **21**, 1328 (2004).

[43] J. E. Sipe and R. W. Boyd, Phys. Rev. A **46**, 1614 (1992).

[44] R. J. Gehr, G. L. Fischer, R. W. Boyd, and J. E. Sipe, Phys. Rev. A **53**, 2792 (1996).

[45] K. Dolgaleva and R. W. Boyd, Adv. Opt. Photonics **4**, 1 (2012).

[46] D. D. Smith, G. Fischer, R. W. Boyd, and D. A. Gregory, J. Opt. Soc. Am. B **14**, 1625 (1997).

[47] G. Piredda, D. D. Smith, B. Wendling, and R. W. Boyd, J. Opt. Soc. Am. B **25**, 945 (2008).

[48] L. A. Gomez, C. B. de Araujo, A. M. Brito Silva, and A. Galembeck, Appl. Phys. B **92**, 61 (2008).

[49] R. F. Souza, M. A. R. C. Alencar, E. C. da Silva, M. R. Meneghetti, and J. M. Hickmann, Appl. Phys. Lett. **92**, 201902 (2008).

[50] H. B. de Aguiar, P. Gasecka, and S. Brasselet, Opt. Express **23**, 8960 (2015).

Tampereen teknillinen yliopisto
PL 527
33101 Tampere

Tampere University of Technology
P.O.B. 527
FI-33101 Tampere, Finland

ISBN 978-952-15-4209-1
ISSN 1459-2045